



## Thermal radiation management by natural photonic structures: *Morimus asper funereus* case

Darko Vasiljević<sup>a</sup>, Danica Pavlović<sup>a,\*</sup>, Vladimir Lazović<sup>a</sup>, Branko Kolarić<sup>a,c</sup>, Branislav Salatić<sup>a</sup>, Wang Zhang<sup>b</sup>, Di Zhang<sup>b</sup>, Dejan Pantelić<sup>a</sup>

<sup>a</sup> Institute of Physics, University of Belgrade, Pregrevica 118, 11080, Belgrade, Zemun, Serbia

<sup>b</sup> State Key Lab of Metal Matrix Composite, Shanghai Jiao Tong University, 800 Dongchuan Road, Shanghai, 200240, China

<sup>c</sup> Micro- and Nanophotonic Materials Group, University of Mons, Place du Parc 20, 7000, Mons, Belgium

### ARTICLE INFO

#### Keywords:

Photonic structures  
Infrared radiation  
Hyperuniformity  
Radiative energy exchange  
Longicorn beetle

### ABSTRACT

Convective, conductive and radiative mechanisms of thermal management are extremely important for life. Photonic structures, used to detect infrared radiation (IR) and enhance radiative energy exchange, were observed in a number of organisms. Here we report on sophisticated radiative mechanisms used by *Morimus asper funereus*, a longicorn beetle whose elytra possess a suitably aligned array of lenslets and blackbodies. Additionally, a dense array of microtrichia hyperuniformly covers blackbodies and operates as a stochastic, full-bandgap, IR-photonic structure. All these features, whose characteristic dimensions cover a range from several hundred down to a few micrometres, operate synergistically to improve the absorption, emission and, possibly, detection of IR radiation. We present a morphological characterization of the elytron, thermal imaging measurements and a theoretical IR model of insect elytron, uncovering a synergistic operation of all structures.

### 1. Introduction

Colouration in the living world serves multiple purposes, such as: camouflage, mimicry, warning or attraction (Doucet and Meadows, 2009; Kemp, 2007; Sweeney et al., 2003; Verstraete et al., 2019), and it sometimes affects the very existence of animals. Radiative heat exchange with the environment can also be influenced by colours, through absorption or reflection of the visible light. There is a delicate balance between colouration and other mechanisms of thermal regulation: convection, conduction, radiation emission and absorption, evaporation, perspiration, internal heat generation, behaviour (Bosi et al., 2008; Cossins, 2012).

Such mechanisms have also been observed in insects. Their exoskeleton (cuticle) serves many functions, such as: locomotion, providing a defence barrier (against mechanical stress, cold, hot or wet environment), a reservoir for the storage of metabolic waste products, mechano- and chemoreception, balancing radiant energy absorption in the visible and dissipation in the infrared (IR) part of the spectrum (Capinera, 2008; Gillott, 2005; Gullan and Cranston, 2004; Shi et al., 2015). The cuticle is usually patterned on micro- and nano-scale and produces striking optical effects. Such photonic structures (Vukusic and

Sambles, 2003) create structural colouration (Vukusic et al., 2001) in the visible, but can have an important role in the infrared part of the spectrum, participating in thermoregulation (Scoble, 1992; Shi et al., 2015).

Most insects are primarily ectothermic and rely on external heat sources, such as solar radiation (Nijhout, 1991). It is proven that butterflies use physiological mechanisms to regulate the heat gain by orientation and posture relative to the sun (Kingsolver, 1985). On the other hand, structures are developed during evolution to efficiently reflect the visible light, simultaneously dissipating infrared radiation directly into the atmospheric window at mid-infrared, as in the Saharan silver ant, *Cataglyphis bombycina* (Roger, 1859) (Shi et al., 2015). This clever mechanism enables an insect to efficiently regulate its body temperature in a hostile desert environment.

In addition, the insect cuticle can be a place where so-called extra-ocular photoreception occurs. Also known as “dermal light sense” and defined as a “widespread photic sense that is not mediated by eyes or eyespots and in which light does not act directly on an effector” (Millott, 1968), it has been reported in several orders of insects. Some butterflies have such photoreceptors located at the end of their abdomens to control copulation in males and oviposition in females (Arikawa and Takagi,

\* Corresponding author. Institute of Physics, University of Belgrade, Serbia Pregrevica 118, 11080, Belgrade, Zemun, Serbia.

E-mail address: [danica.pavlovic@ipb.ac.rs](mailto:danica.pavlovic@ipb.ac.rs) (D. Pavlović).

<https://doi.org/10.1016/j.jtherbio.2021.102932>

Received 19 November 2020; Received in revised form 5 March 2021; Accepted 29 March 2021

Available online 3 April 2021

0306-4565/© 2021 Elsevier Ltd. All rights reserved.

2001). In some cases, dermal light sensitivity has been confirmed from behavioural responses, mediated by light intensity and wavelength (Desmond Ramirez et al., 2011). For example the larvae of *Tenebrio molitor* avoid light even after decapitation (Tucolesco, 1933). Light sensitivity of the *Aphis fabae* antennae is responsible for the insect's photokinetic activity (Booth, 1963).

Here we highlight the specific architecture of *Morimus asper funereus* (Mulsant, 1863) (Insecta: Coleoptera: Cerambycidae) elytra, which implicates dermal detection of IR radiation, a feature not previously observed in any other species. We also study the radiative properties of the elytra. Electron and optical microscopy were used to reveal the external and internal morphology of elytra, and thermal imaging to establish its radiative properties in the thermal IR (7.5–13  $\mu\text{m}$ ) part of the spectrum. Theoretical analysis and 3D modelling were used to reveal the role of microstructures.

## 2. Materials and methods

### 2.1. Insect

*Morimus asper funereus* (Fig. 1) (family Cerambycidae, subfamily Lamiinae) is a large longicorn beetle inhabiting central and southern Europe. The species is characterized by grey elytra with four black patches and a body length of 15–40 mm (Parisi and Busetto, 1992). The colouration and velvety appearance of the elytra comes from the dense tomentum of the setae, grey hairs and black scales, embedded in the elytral surface, which is black and shiny. The hind wings (alae) of *M. asper funereus* are reduced and the species is flightless (Solano et al., 2013).

*M. asper funereus* is a saproxylic species (Carpaneto et al., 2015; Hardersen et al., 2017) and depends on decaying wood during larval development. This process takes place in tree trunks and stumps and lasts approximately three or four years (Stanić et al., 1985). We noticed that the insects evade direct sunlight. We never found them on trunks that were directly exposed to solar radiation: when we subjected an insect to sunlight, it hid in the shadow. This was confirmed by other research, which found that this species is active during the evening and at night (Polak and Maja, 2012; Romero-Samper and Bahülo, 1993). Hardersen et al. (2017) determined that the highest activity of the species was between 20:00 and 24:00. However, the authors stated that *M. asper funereus* individuals were seen during the day, but that the number was only 30% of the maximum recorded in the evening and at night.

The species is strictly protected in Europe (and Serbia) by Annex II of the Habitat Directive 92/43/CEE. In the IUCN Red List of Threatened Species, it is designated as vulnerable (A1c) (IUCN Red List of Threatened Species, 2018). We had ten, conserved and pinned, specimens at our disposal, collected during the summer of 2018 on Mt. Avala, near the city of Belgrade, with the permission of the Serbian Ministry of



Fig. 1. *Morimus asper funereus*: a longicorn beetle whose most prominent features are black body and greyish elytra with four prominent black patches.

Environmental Protection (N°:353-01 –1310/2018-04).

### 2.2. Microanalysis

A stereomicroscope (STEBA600, Colo Lab Experts, Slovenia) with maximum magnification up to 180X, eyepiece 20X, auxiliary objective 2X, working distance 100 mm, reflection and transmission mode, and equipped with a digital camera (Canon EOS 50D, Tokyo, Japan) was used to examine the anatomy of the whole insect.

The optical characteristics of the elytra and setae were analysed on a trinocular microscope (MET104, Colo Lab Experts, Slovenia) (maximum magnification 400X, polarization set, objectives Plan Achromatic POL Polarizing 10X/20X/40X).

Micro-computed tomography (micro-CT) was employed to view the overall anatomy of the beetle and measure the thickness of the elytra. We had at our disposal the Skyscan 1172 system (Bruker, USA). To ensure the optimum signal/noise ratio during micro-CT imaging, the specimens were scanned without filter, with scanning parameters set as follows: 40 kV, 244  $\mu\text{A}$ , 530 ms, rotation step 0.2° (pixel size 13.5  $\mu\text{m}$ ). For the purpose of this experiment, CT scanning was performed without any special preparation of a specimen.

A field emission gun scanning electron microscope (FEGSEM) (MiraSystem, TESCAN, Czech Republic) was used for ultrastructural analysis. Prior to analysis, insect elytra were removed and placed on an aluminium mount and coated with a thin layer (5–10 nm) of gold palladium (AuPd), using a SC7620 Mini Sputter Coater (Quorum Technologies Ltd., UK).

### 2.3. Thermal infrared (IR) analysis

Assessment of the thermal properties of insects is normally done by some kind of thermometry (Heinrich, 2013). With the advent of IR cameras, thermal imaging (TI) becomes a method of choice. It is a non-invasive and non-contact technique with applications in numerous fields (Vollmer and Möllmann, 2010). Recently, TI become an important sensing technology in biological investigations (Kastberger and Stachl, 2003). TI cameras are a relatively new tool in studying nocturnal flying animals: birds, bats and insects (Horton et al., 2015). So far, most TI studies of insects have focused on the thermoregulation of Hymenoptera species (Stabentheiner and Schmaranzer, 1987; Stabentheiner et al., 2012).

In this research, the emission of thermal radiation was analysed by an IR thermal camera corresponding to an atmospheric window at 7.5–13  $\mu\text{m}$  (FLIR A65, USA, 640 x 512 pixels, thermal resolution/NETD 50 mK). Thermal measurements were corrected for surface emissivity, and reflected temperature, while images were acquired without binning. Due to the smallness of the insect, we positioned the camera as close as possible (at a distance between 10 and 20 cm), and sometimes used an additional lens to further magnify the thermal image. Under these conditions, the Narcissus effect (radiation emitted by the camera itself) was pronounced. For this reason, we positioned the elytra outside the thermal beam emanating from the camera objective. The rest of the camera body was shielded by aluminium foil.

We manufactured an aluminium cavity and coated it with an absorbing, velvety material whose absorbance was measured at 0.996, in agreement with the calculated value (Prokhorov, 2012). It was used as a reference to measure elytra emissivities, as shown in Fig. 2.

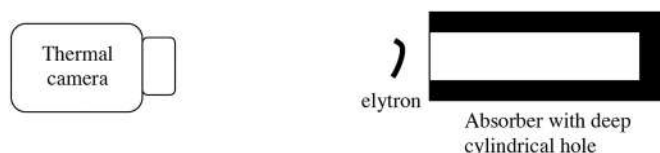


Fig. 2. A simple experimental setup for thermal measurements.

### 3. Results

#### 3.1. Morphological and optical characterization of photonic structures of *M. asper funereus*

The macroscopic anatomy of a dried specimen, visualized using micro-CT (Fig. 3), showed that the elytra of *M. asper funereus* are ellipsoidal, sclerotized and thick (between 200 and 350  $\mu\text{m}$ ). The hind wings of *M. asper funereus* are highly reduced and there is a large, air-filled space between the elytra and the insect body.

The elytra of *M. asper funereus* (Fig. 1) possess a hierarchical structure with a number of features ranging from macroscopic to micron and submicron levels.

The inner surface (facing the insect body) looks spongy (Fig. 4(a)), with an array of oval zones (approx. 0.2–0.4 mm in size – see Fig. 4(b)), surrounded by yellowish walls. If observed in transmission, it can be seen that the walls are actually a complex, connected network of channels that transport hemolymph (Fig. 4(c)) (Unruh and Chauvin, 1993; van de Kamp and Greven, 2010). Within each zone, there is a spherical-looking object with a circular opening at its centre that looks like a standard blackbody (BB) model found in textbooks. In transmission (Fig. 4(c)), BBs are deep red, doughnut-shaped features in the middle of each oval zone. It should be noted that the red colour is due to melanin, characterized by strong absorption in the blue-green part of the spectrum and good transmission in the red. By bleaching elytra using hydrogen peroxide ( $\text{H}_2\text{O}_2$ ) we were able to reveal a network of smaller channels, connecting the BB to the main microfluidic channels. (Fig. 4 (d)).

All the structures described above are protected by an optically transparent layer. This layer is electron-dense (Fig. 5) and hides all the structures observed optically. Microtrichia (thorn-like structures, approx. 5  $\mu\text{m}$  in height – inset in Fig. 5) are a dominant feature of the internal surface. As can be seen, the microtrichia are arranged in an ordered but not completely regular pattern (average mutual distance is 11  $\mu\text{m}$ ). In many other insects, such structures are used to lock the hind wings to the elytra, as in the Asian ladybeetle (Sun et al., 2018).

Outer surface of elytra is black and covered with two different types of microtrichiae (Fig. 6(a) and (b)). One type is transparent and covers most of the body, which looks greyish (grey zone) due to the scattered

radiation. The other type is pigmented and densely covers four distinct areas producing characteristic black patches. However, in thermal infrared, the whole body looks quite uniform.

On grey elytral zone there is also an array of shiny black, quite smooth, microlens-like protrusions, surrounded with hairs (compare optical and SEM images in Fig. 6(c), respectively). The microlenses and BBs have a well-defined mutual orientation, which was observed by simultaneously illuminating the elytron in transmission and reflection (Fig. 7). As observed before (Fig. 4), the BB occupies the centre of an oval zone, while the microlens is at its rim, directly facing a hemolymph-filled channel.

The elytron directly beneath the surface (procuticle 200- $\mu\text{m}$  thick) is well organized, as in all coleopteran (van de Kamp and Greven, 2010; van de Kamp et al., 2016). It is layered and possesses a number of laminae that envelope the BBs and microchannels (Fig. 8(a)). It is interesting to note a number of tiny hairs covering the internal surface of the blackbody (Fig. 8(b)). At the moment, we can only speculate about their biological function, because this can be revealed only by physiological investigation of live specimens, which we didn't have at our disposal. However, from purely physical point of view, we note that hairs increase the absorbance of the black body wall due to enhanced scattering and trapping of radiation.

#### 3.2. Radiative properties of *M. asper funereus*

We used thermal imaging to evaluate radiative properties of elytra. An elytron was placed in front of the reference cavity (with absorbance higher than 99% (Prokhorov, 2012)) and observed with a thermal camera (operating within the 8–14  $\mu\text{m}$  wavelength range). In thermal equilibrium (room temperature), the elytron completely disappears from thermal image (Fig. 9(a)) and becomes visible only when heated by the laser beam (Fig. 9(b)). The same is true for both the outer and inner sides, along the entire, highly curved, elytral surface. Thus, we may conclude that the high directional emissivity (higher than 99%) is constant along the surface and has the characteristics of a Lambertian source.

It is interesting to note that the emissivity of both black and grey areas of elytra is the same. This is because the wavelength of thermal radiation is close to characteristic dimensions of hairs covering the

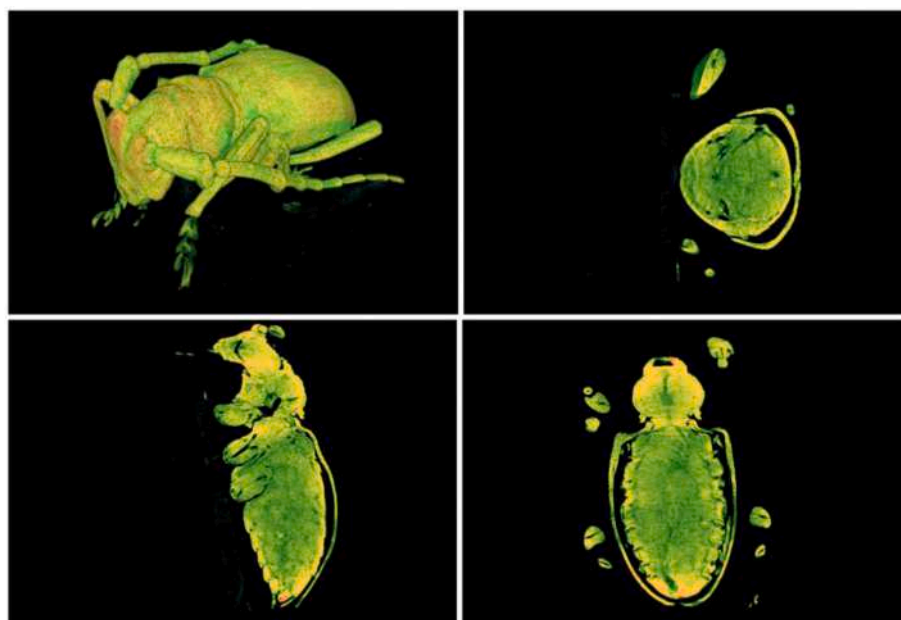
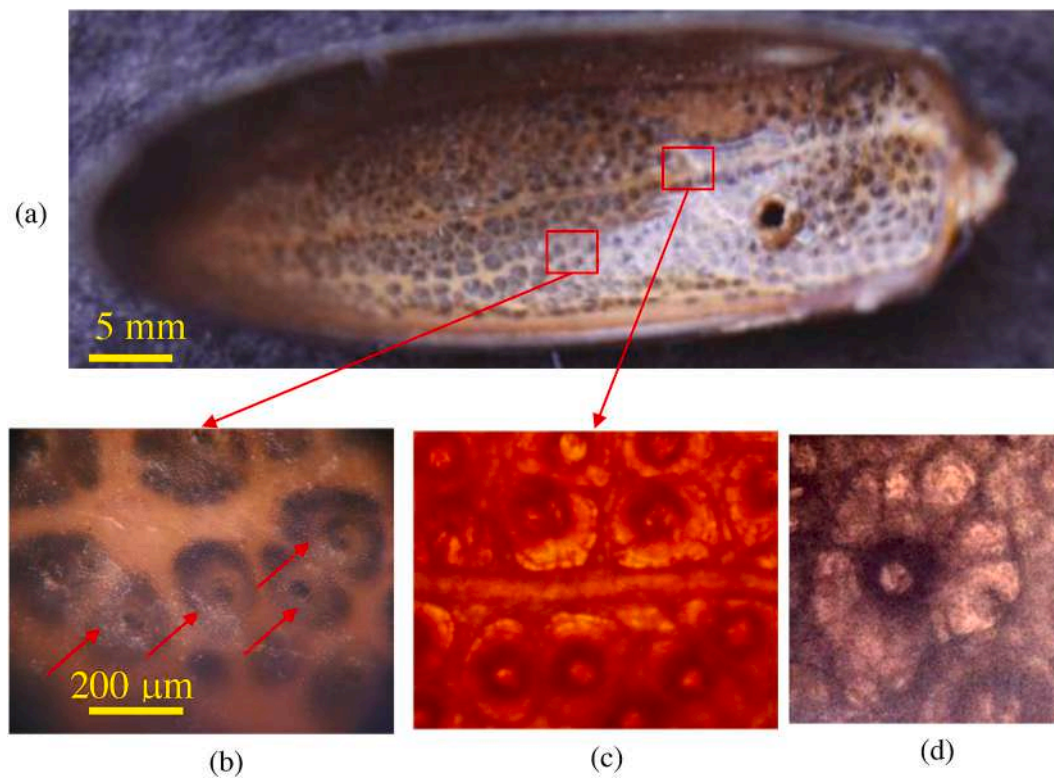
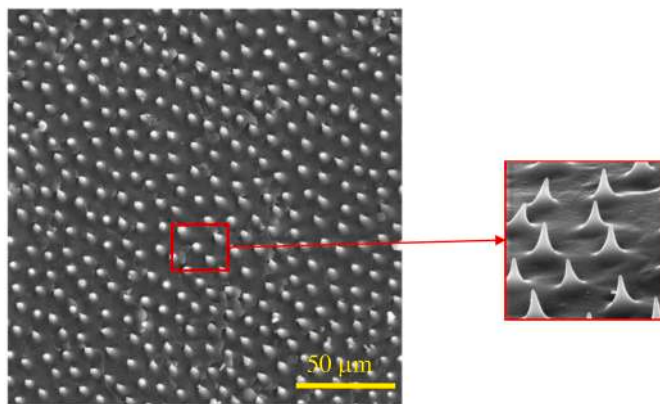


Fig. 3. (a) 3D reconstruction of *M. asper funereus* from a stack of MicroCT images. (b) frontal, (c) axial and (d) longitudinal cross sections of insect showing air filled space between elytra and the rest of the body.





**Fig. 4.** (a) Optical image of inner elytral surface of *M. asper funereus* in its natural state, exhibiting its original pigmentation. Enlarged portion in (b) shows blackbody-like (BB) structures (spherical-looking, with a black spot in the centre – red arrows). (c) Transmission optical image of elytron reveals a system of channels, branching from the central channel and surrounding each BB. (d) Elytron bleached in peroxide reveals a network of smaller channels, connecting the BB to the main microfluidic channels.



**Fig. 5.** SEM image of inner elytral surface of *M. asper funereus* with an array of microtrichia, enlarged in the inset.

elytra. That is why both types of hairs efficiently scatter the radiation and enhance the probability of radiation being absorbed.

### 3.3. Modelling of *M. asper funereus* elytron

#### 3.3.1. Blackbody array

Based on the anatomical features described in section 3.1, we were able to design a model of *M. asper funereus*. We took the oval zone of Fig. 4 as an elementary unit, composed of a layered blackbody surrounded by walls with microchannels. Blackbody is enclosed between two layers, one containing microlenses and the other covered by microtrichia.

We used 3D, open-source, computer graphics software (Blender, free

under GPL) to visualize the elementary unit of *M. asper funereus* elytra. Fig. 10(a) and (b) show two aspects of an elementary cell, so that the spatial relations between the microlenses, walls with microchannels and blackbody are clearly seen. Microlenses focus radiation directly into the elytron and microchannel filled with hemolymph (primarily water), as confirmed by ray tracing (Fig. 11) within a quite large angular range ( $-20^\circ$  to  $+20^\circ$ ).

We made a more exact finite element modelling of IR wave propagation in the cuticle. To do that, we needed complex refractive indices of hemolymph and insect cuticle at thermal infrared wavelengths. Hemolymph is mostly composed of water and we used the data from Hale and Querry (1973) – complex refractive index was averaged to  $n = 1.2 + i \cdot 0.0343$ , within 3–5  $\mu\text{m}$ , and  $n = 1.35 + i \cdot 0.13$ , within 8–12  $\mu\text{m}$ . Optical constants of insect cuticle at thermal infrared are not very well known and we used data extracted from Shi (2018) – within 3–5  $\mu\text{m}$  complex refractive index was  $n = 1.57 + i \cdot 0.005$  and within 8–12  $\mu\text{m}$ ,  $n = 1.57 + i \cdot 0.1$ . The absorption of melanin was not taken into account because it is found only in a thin superficial layer of elytra, its concentration is low, compared to that of chitin, and its absorption maximum is at UV.

Within the 8–12  $\mu\text{m}$  window, radiation is efficiently absorbed in the superficial layers of the cuticle due to the very high absorption coefficient of chitin (see Fig. 12(b)). The situation is more interesting within the 3–5  $\mu\text{m}$  window, where the absorption is an order of magnitude lower (Shi, 2018). There, the radiation is indeed focused onto the microchannels (Fig. 12(c)), while the multilayer structure of the BB efficiently reflects and expels the radiation from the central cavity. Within this spectral range, radiation penetrates deep and heats the internal structures of cuticle (Fig. 12(c)). If there is a constant flow of hemolymph through the cuticle (Unruh and Chauvin, 1993) heat will be convectively transferred to the central cavity of the blackbody. That is why we propose that tiny hairs lining the cavity might function as

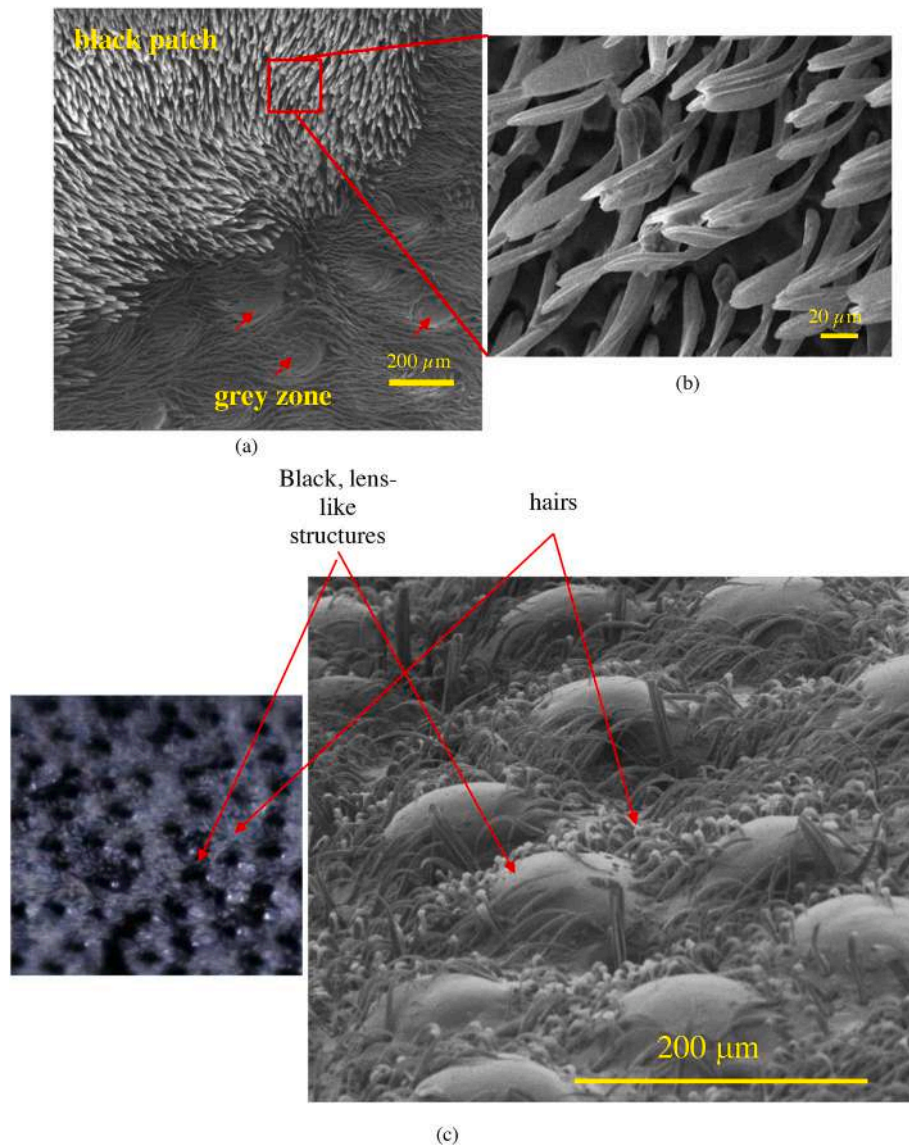


**Fig. 6.** SEM of the outer surface of the *M. asper funereus* elytra: (a) an edge between grey and black areas (red arrows indicate microlens-like protrusions); (b) enlarged SEM image of black scales. (c) Lens-like structures and hairs on the outer surface of *M. asper funereus*. Optical image is on the left and SEM image on the right. The captured area with lens-like structures is from the grey zone of the elytra.

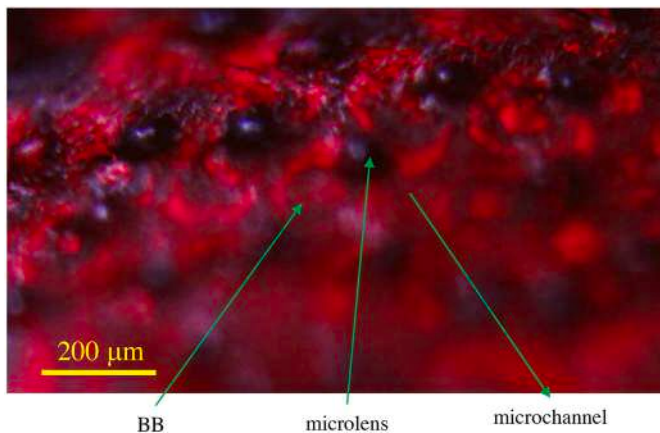


**Fig. 7.** Optical microscope image of elytron, simultaneously illuminated in reflection and transmission. Microlenses can be seen as black circular areas, blackbodies are doughnut-shaped zones within the network of channels.

sensilla, signalling the insect to search for a cooler place - which is a behavioural characteristic of this particular insect.

It seems that cuticular microlenses function like the cornea of an ommatidium, i.e. they focus radiation onto the sensitive layer. The architecture of *M. asper funereus* is well organized for the purpose.

### 3.3.2. Array of microtrichia

As can be seen from micro-CT images (Fig. 3), there is a thin (less than a millimetre) air-filled gap between the elytra and the insect body (see scheme at Fig. 13). Thermal energy is radiatively exchanged between those layers, thus filling the gap with infrared radiation. For the part of radiative energy propagating at grazing incidence, gap behaves as a hollow waveguide (such as those used for 10.6 μm CO<sub>2</sub> lasers – (Komachi et al., 2000)) with microtrichie as subwavelength scattering (diffractive) structures. In such waveguides, radiation propagates in a whispering-gallery manner.

In the following we will analyze their possible role in thermal radiation exchange of *M. asper funereus*. For the purpose of better understanding, we will treat microtrichie as a forest-like structure of almost conical protuberances on an otherwise flat surface. Each cone is 4.4 μm



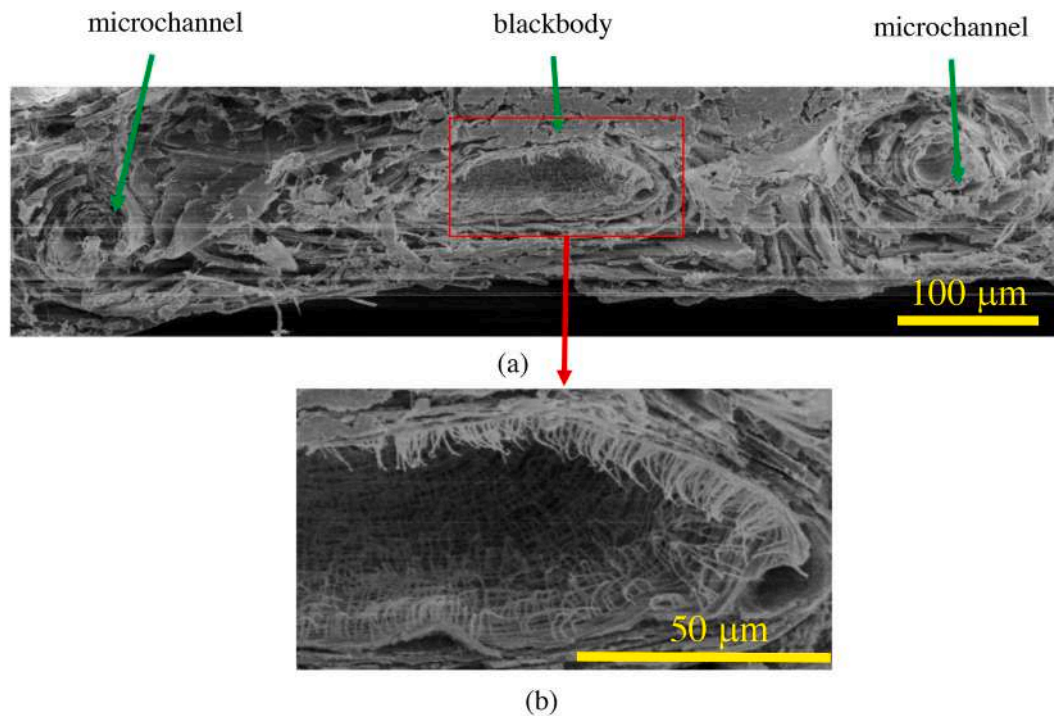


**Fig. 8.** (a) Cross section of *M. asper funereus* elytron with clearly visible blackbody with microchannels on both sides. (b) Enlarged image reveals the hair-like protrusions lining the internal surface of the blackbody.

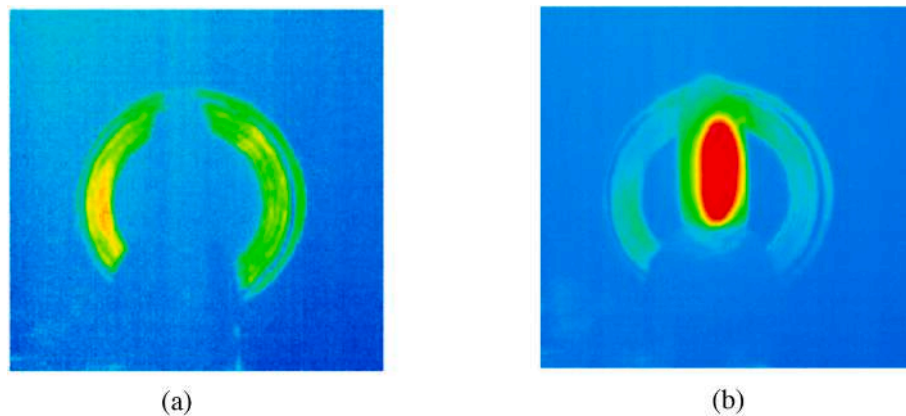


**Fig. 9.** (a) Thermal image of *M. asper funereus* elytra positioned in front of a blackbody. Emissivity is the same and they cannot be discerned. (b) When heated, the elytron becomes visible.

in diameter at its base and  $3.8 \mu\text{m}$  in height. An observer looking from above will see an arrangement like that in Fig. 14, schematically drawn using the section of Fig. 5 as a template. Looking from the side, as if sitting on the substrate, densely overlapping cone projections, even for a small number of microtrichia surrounding the central one, are observed. Thus, for the large number of microtrichia on the elytron, the radiation propagating close to the surface has a high chance of hitting a cone and being absorbed. This is a purely geometric optic analysis – in the following we will present a wave optics perspective.

Upon closer inspection of the spatial distribution of microtrichia (Fig. 5), we can see that it is neither regular nor completely random (rods in the chicken retina are arranged in a similar fashion (Jiao et al., 2014)). It is characterized by a ring-like Fourier transform, as in Fig. 15 (a). The spatial frequency of the prominent ring-like structure is  $0.1/\mu\text{m}$ , corresponding to the average  $10\text{-}\mu\text{m}$  distance between microtrichia (Fig. 15(b)). The amplitude of the Fourier transform goes to zero as the spatial frequencies approach the central Fourier peak. This is a

characteristic of hyperuniform point distributions, which were shown to behave as a complete photonic bandgap structure (Florescu et al., 2009). The slight ellipticity of the Fourier transform observed here is possibly a consequence of the ellipsoidal profile of the elytron.

For thermal radiation entrapped between the elytra and the body, A 2-dimensional hyperuniform system behaves as a random full-bandgap photonic crystal. This can be inferred from the ring-like Fourier transform (Fig. 15(a)), which can be understood as a superposition of sinusoidal gratings with a  $10\text{-}\mu\text{m}$  period oriented in all directions along the plane substrate. Under grazing incidence, gratings behave as Bragg reflectors, blocking the propagation of radiation with the wavelength:

$$\lambda = 2d/N$$

where  $d$  is a grating period,  $N$  is an integer, assuming the normal angle of incidence. For the  $10 \mu\text{m}$  average period of microtrichia and  $N = 2$ , the Bragg wavelength is  $10 \mu\text{m}$ , right in the middle of an  $8\text{--}12 \mu\text{m}$  atmospheric window. Additionally, for  $N = 4$ , the Bragg wavelength

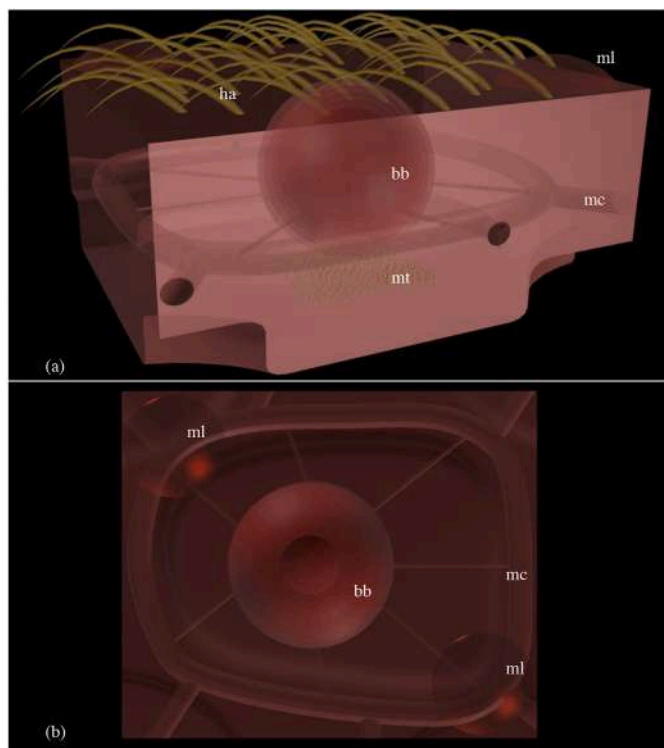


**Fig. 10.** (a) A semi-transparent 3D model of *M. asper funereus* elytron presenting internal structures hidden within the elytron (mt – microtrichia, mc – microchannels, ml – microlens, bb – black body, ha – hairs) (a) with microlenses and hairs clearly seen; (b) top view displaying alignment of microlenses and microchannels. The microchannel completely surrounds the blackbody and is connected to it via even smaller channels.

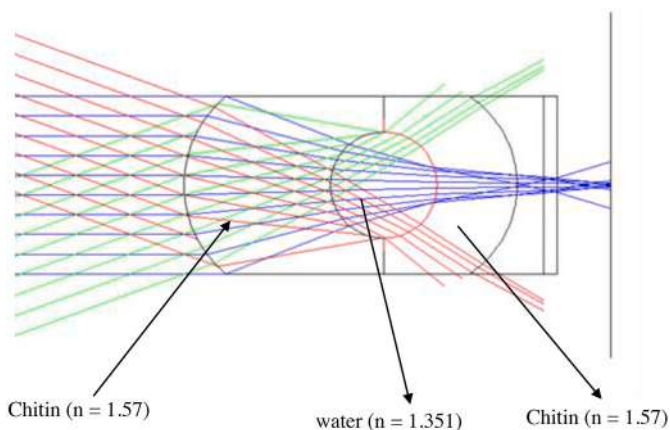


**Fig. 11.** Ray tracing through a microlens and microchannel (blue rays are incoming at normal incidence, while red and green rays obliquely, at  $+20^\circ$  and  $-20^\circ$ , illuminate the elytron). Calculations were done at  $3\ \mu\text{m}$ , where refractive indices are as indicated in figure.

corresponds to another window at  $3\text{--}5\ \mu\text{m}$ , but we were not able to check this experimentally.

#### 4. Discussion and conclusions

The search for highly absorbing structures is a long-standing one and many structured materials have been engineered so far (Mizuno et al., 2009), but only the vertically aligned nanotube array (VANTA black) (De Nicola et al., 2017) approaches the emissivity of a blackbody. In line with the research on silicon photonics for NIR silicon devices (Milošević

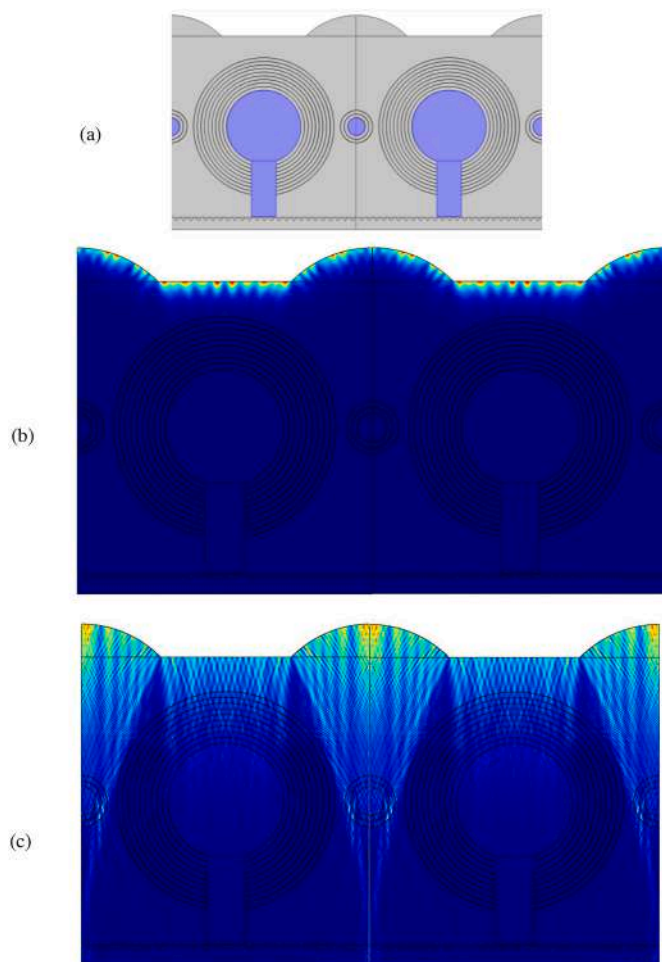


**Fig. 12.** (a) A model of *M. asper funereus* elytron used in FEM analysis (grey colour corresponds to chitin and purple to water). Distribution of thermal IR radiation inside *M. asper funereus* blackbody-like cuticular structure calculated by FEM. Two spectral windows were analysed: (b)  $8\text{--}12\ \mu\text{m}$  (image at  $10\ \mu\text{m}$  is shown) and (c)  $3\text{--}5\ \mu\text{m}$  (image at  $4\ \mu\text{m}$  is shown).

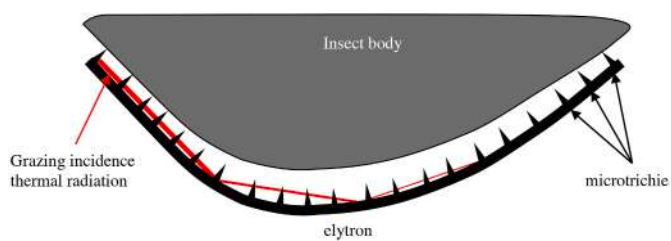


**Fig. 13.** *M. funereus* elytron and body with air filled gap acting as a hollow waveguide for grazing incidence thermal radiation.

et al., 2019), here we show that natural, less complex structures can achieve similar results owing to their forest-like structure and intrinsic curvature (Leonhardt and Tyc, 2009). A clever arrangement of hyper-uniform disordered structures efficiently competes with highly advanced nanotube structures. In contrast to artificial VANTA black material, which is fragile and complex to manufacture, the natural solution is robust and simple.

At this point, we are not able to estimate how important the role of microtrichia is. We must stress, however, that the amount of the radiation entrapped between elytra and the body is non-negligible due to Fresnel reflections and waveguiding. Simple calculation shows that, for the refractive index used in this study ( $n = 1.57$ ) and normal incidence,

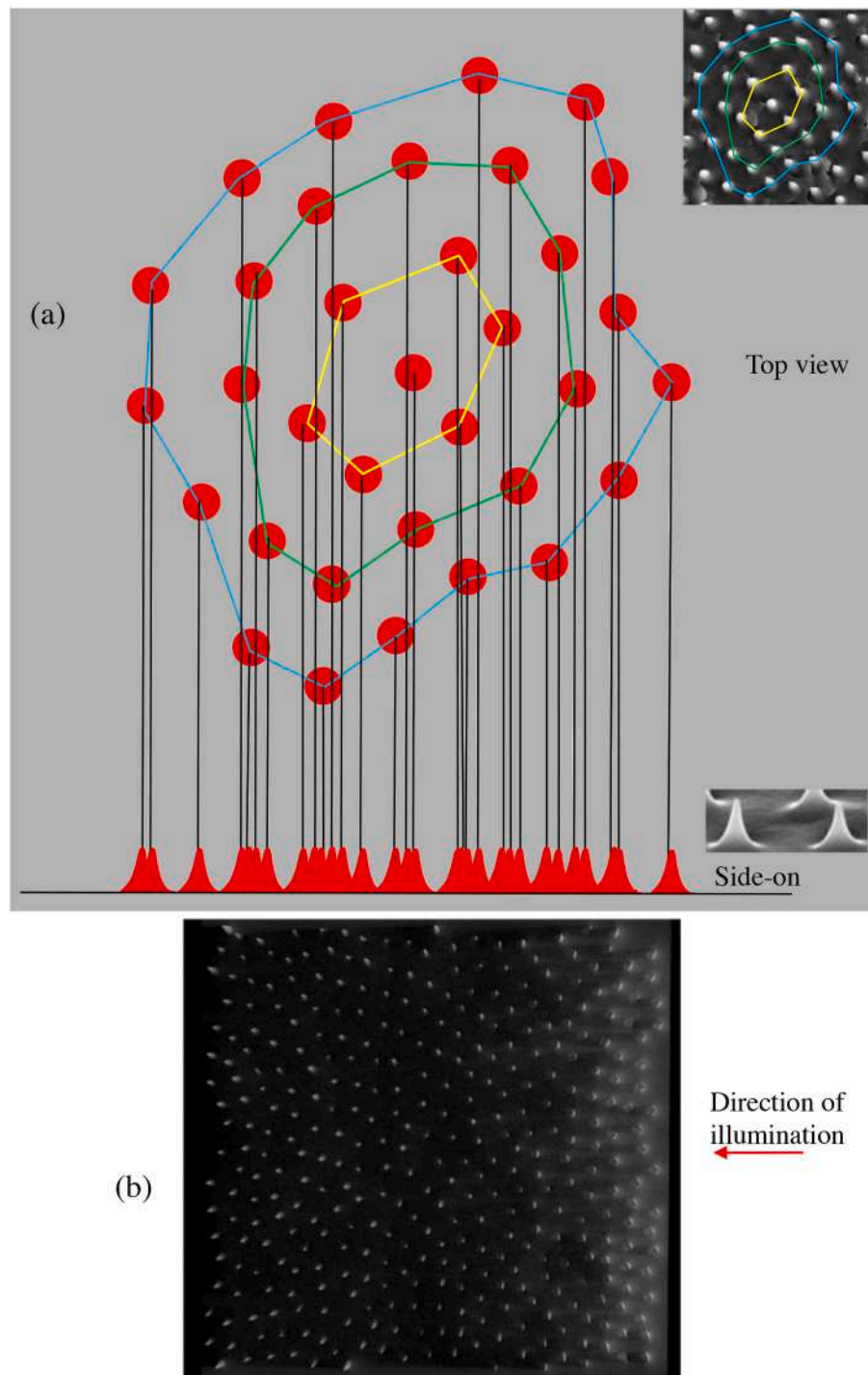


**Fig. 14.** (a) An arrangement of conical structures seen from above and drawn using Fig. 2 as a template. Inset in the upper right corner shows part of the SEM image used as a template. Side-on view is shown at the bottom of this figure. (b) Top view of a microtrichia 3D model illuminated obliquely from the right (red arrow) shows that microtrichia preclude the propagation of light.

4.99% of radiation is reflected, while for grazing incidence almost all radiation is reflected. Between those two extremes, due to uniform angular distribution of thermal radiation, it is clear that more than 4.99% of thermal radiation is entrapped and waveguided between body and elytra. More detailed answer to this question will be given in further studies.

In the interests of brevity and focus, several other elytral features that might be effective in thermal IR had to be left out of the scope of this paper. First of all, the chitinous lamellae of *M. asper funereus* have a

characteristic dimension of 4–5  $\mu\text{m}$  with the corresponding Bragg wavelength of 8–10  $\mu\text{m}$ . Each layer contains well-oriented microfibrils that certainly introduce birefringence, and the orientation of microfibrils is different in each layer (Supplement file). The exact value of the refractive index of chitinous structures is not very well known, in particular in the thermal infrared, and it is therefore difficult to make the correct theoretical calculations and numerical simulations. Thirdly, interfaces between each layer are rough and scatter radiation, so that the layers may act as planar waveguides to additionally absorb the



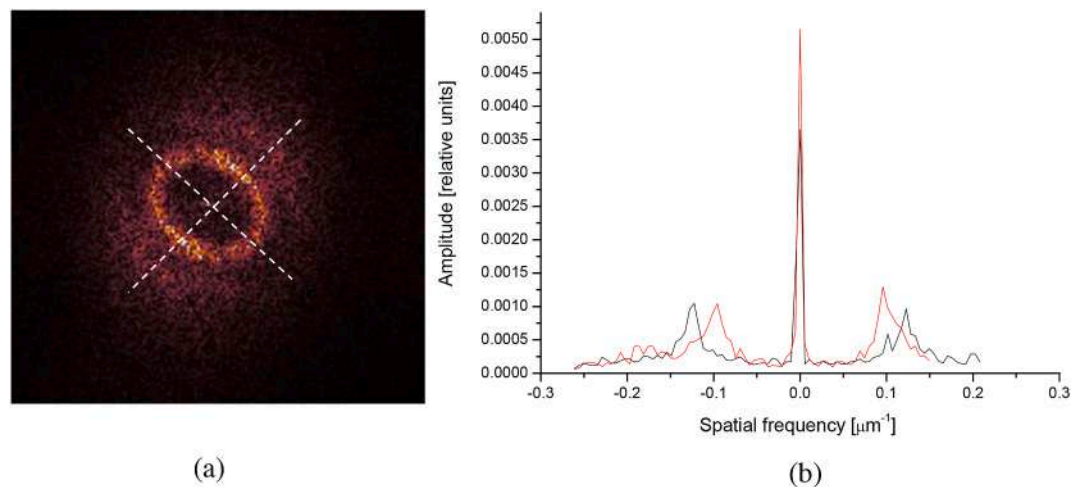


**Fig. 15.** (a) A Fourier transform of the image in Fig. 2 depicting the arrangement of microtrichia. Note the ring-like pattern with slight ellipticity. (b) Scanning along two orthogonal directions (see dotted lines in (a)) shows a pronounced peak at spatial frequency close to  $0.1/\mu\text{m}$ , corresponding to the average  $10\text{-}\mu\text{m}$  distance between microtrichia.

radiation. Finally, microtrichia can act as transmission gratings for non-obliquely impinging radiation and diffraction orders can be coupled into layers as planar waveguides.

From a theoretical point of view, it is quite difficult to treat inherently random structures (such as those of *M. asper funereus*) using exact methods like FEM, RCWA or FDTD. For large structures, periodic boundary conditions have to be introduced, thereby violating inherent randomness. If a random structure is to be simulated, computer memory requirements become extremely large and computational time intolerably long.

We performed other measurements that have revealed the excellent thermal insulation properties of this particular insect. By laser-heating one side of an elytron we observed that, in thermal equilibrium, the other side was approximately  $20\text{ }^{\circ}\text{C}$  lower in temperature. It is difficult to discern the contribution of radiative dissipation, with respect to other processes (convection and conduction) (Supplement file). However, the *M. asper funereus* elytron could be an excellent model to design similar thermally insulating materials.

Furthermore, taking into account that *M. asper funereus* lays its eggs in and emerging larvae feed on decaying wood (a saproxylic way of life), similarly to pyrophilous insects (Klocke et al., 2011), it is important for an insect to detect dead trees. Thermal fingerprint of a decaying wood is different, compared to healthy specimens, primarily due to the reduced amount of water. (Pitarma et al., 2019). Based on the structures and properties we have observed, we postulate that a number of infrared detectors on the elytron is used to detect the infrared fingerprint of wood and discriminate between healthy and decaying tree trunks. Even though the number of elytral IR detectors (approx. 400) is small, it is still a useable one, if compared to that of FLIR ONE Gen3 smart-phone, clip-on thermal cameras (60 x 80 IR pixels). By making this comparison we emphasize the “ingenuity” of evolution, in no way endorsing any particular IR camera.

It is well known that Coleoptera elytron has a complex layered structure with number of cavities, trabeculae, channels and pores (Sun and Bhushan, 2012). Research mostly dealt with mechanical significance of internal architecture of elytron (Du and Hao, 2018), and to a lesser degree with thermal effects (Le et al., 2019). By studying available literature we may say that many of structures might serve similar role in thermal radiation management, due to their characteristic dimensions being close to the wavelength of thermal radiation.

In conclusion, we have shown that a combination of micron-sized blackbodies and uniformly random microstructures possesses excellent properties to manage thermal radiation. The range of potential

applications is enormous and even might even extend from NIR to terahertz technology.

#### Funding

This work was supported by the Serbian Ministry of Education, Science and Technological Development, and the Science and Technology Development Programme – Joint Funding of Development and Research Projects of the Republic of Serbia and the People’s Republic of China: Mimetics of insects for sensing and security, No. I-2. BK acknowledges support from the F.R.S.- FNRS. DP acknowledges support from L’Oréal-UNESCO “For Women in Science”.

#### Ethical approval

All necessary permissions to collect the samples of *M. asper funereus* were obtained from the Ministry of Environmental Protection of the Republic of Serbia and the Institute for Nature Conservation of Serbia. The research did not include live insects.

#### Author statement

**Darko Vasiljević** : Formal analysis, Data Curation, Visualization.  
**Danica Pavlović**: Conceptualization, Formal analysis, Investigation, Resources, Writing-Original Draft Preparation.  
**Vladimir Lazović**: Formal analysis.  
**Branko Kolarić**: Project Administration, Writing Review and Editing.  
**Branislav Salatić**: Softwer, Formal analysis.  
**Wang Zhang**: Supervision, Validation.  
**Di Zhang**: Supervision, Validation.  
**Dejan Pantelić**: Conceptualization, Methodology, Investigation, Formal analysis, Writing-Original Draft Preparation.

#### Declaration of competing interest

The authors declare no conflict of interest.

#### Appendix A. Supplementary data

Supplementary data to this article can be found online at <https://doi.org/10.1016/j.jtherbio.2021.102932>.

## References

- Arikawa, K., Takagi, N., 2001. Genital photoreceptors have crucial role in oviposition in Japanese yellow swallowtail butterfly, *Papilio xuthus*. *Zool. Sci.* 18 (2), 175–179. <https://doi.org/10.2108/zsj.18.175>.
- Booth, C.O., 1963. Photocinetic function of aphid antennae. *Nature* 197, 265–266.
- Bosi, S.G., Hayes, J., Large, M.C.J., Poladian, L., 2008. Color, iridescence, and thermoregulation in Lepidoptera. *Appl. Opt.* 47, 5235–5241. <https://doi.org/10.1364/AO.47.005235>.
- Capinera, J.L., 2008. *Encyclopedia of Entomology*. Springer, New York.
- Carpaneto, G.M., Baviera, C., Biscaccianti, A.B., Brandmayr, P., Mazzei, A., Mason, F., Battistoni, A., Teofili, C., Rondinini, C., Fattorini, S., Audisio, P., 2015. A Red List of Italian Saproxyllic Beetles: taxonomic overview, ecological features and conservation issues (Coleoptera). *Fragm. Entomol.* 47, 53. <https://doi.org/10.4081/fe.2015.138>.
- Cossins, A., 2012. *Temperature Biology of Animals*. Springer Science & Business Media.
- De Nicola, F., Hines, P., De Crescenzi, M., Motta, N., 2017. Thin randomly aligned hierarchical carbon nanotube arrays as ultrablack metamaterials. *Phys. Rev. B* 96 (4), 045409. <https://doi.org/10.1103/PhysRevB.96.045409>.
- Desmond Ramirez, M., Speiser, D.I., Sabrina Pankey, M., Oakley, T.H., 2011. Understanding the dermal light sense in the context of integrative photoreceptor cell biology. *Vis. Neurosci.* 28, 265–279. <https://doi.org/10.1017/S0952523811000150>.
- Doucet, S.M., Meadows, M.G., 2009. Iridescence: a functional perspective. *J. R. Soc. Interface* 6 (Suppl. 1.2), S115–S132. <https://doi.org/10.1098/rsif.2008.0395.focus>.
- Du, J., Hao, P., 2018. Investigation on microstructure of beetle elytra and energy absorption properties of bio-inspired honeycomb thin-walled structure under axial dynamic crushing. *Nanomaterials* 8 (9), 667. <https://doi.org/10.3390/nano8090667>.
- Florescu, M., Torquato, S., Steinhardt, P.J., 2009. Designer disordered materials with large, complete photonic band gaps. *Proc. Natl. Acad. Sci. Unit. States Am.* 106 (49), 20658–20663. <https://doi.org/10.1073/pnas.0907744106>.
- Gillott, C., 2005. Food uptake and utilization. *Entomology (Tokyo)* 487–513. [https://doi.org/10.1007/1-4020-3183-1\\_16](https://doi.org/10.1007/1-4020-3183-1_16).
- Gullan, P.J., Cranston, P.S., 2004. *The Insects: An Outline of Entomology*. John Wiley & Sons.
- Hale, G.M., Querry, M.R., 1973. Optical constants of water in the 200-nm to 200- $\mu$ m wavelength region. *Appl. Opt.* 12 (3), 555–563. <https://doi.org/10.1364/ao.12.000555>.
- Hardersen, S., Bardiani, M., Chiari, S., Maura, M., Maurizi, E., Roversi, P.F., Mason, F., Bologna, M.A., 2017. Guidelines for the monitoring of *Morimus asper funereus* and *Morimus asper asper*. *Nat. Conserv.* 20, 205–236. <https://doi.org/10.3897/natureconservation.20.12676>.
- Heinrich, B., 2013. *The Hot-Blooded Insects: Strategies and Mechanisms of Thermoregulation*. Springer Science & Business Media, New York.
- Horton, K.G., Shriver, W.G., Buler, J.J., 2015. A comparison of traffic estimates of nocturnal flying animals using radar, thermal imaging, and acoustic recording. *Ecol. Appl.* 25 (2), 390–401. <https://doi.org/10.1890/14-0279.1.sm>.
- Jiao, Y., Lau, T., Hatzikirou, H., Corbo, J.C., Torquato, S., Mathematics, A., 2014. Avian photoreceptor patterns represent a disordered hyperuniform solution to a multiscale packing. *Phys. Rev.* 89 (2), 022721. <https://doi.org/10.1103/PhysRevE.89.022721>.
- Kastberger, G., Stachl, R., 2003. Infrared imaging technologies. *Behav. Res. Methods Instrum. Comput.* 35 (3), 429–439.
- Kemp, D.J., 2007. Female butterflies prefer males bearing bright iridescent ornamentation. *Proc. Biol. Sci.* 274 (1613), 1043–1047. <https://doi.org/10.1098/rspb.2006.0043>.
- Kingsolver, J.G., 1985. Butterfly thermoregulation: organismic. *J. Res. Lepid.* 24 (1), 1–20.
- Klocke, D., Schmitz, A., Soltner, H., Bousack, H., Schmitz, H., 2011. Infrared receptors in pyrophilous (“fire loving”) insects as model for new un-cooled infrared sensors. *Beilstein J. Nanotechnol.* 2 (1), 186–197. <https://doi.org/10.3762/bjnano.2.22>.
- Komachi, Y., Wakaki, M., Kanai, G., 2000. Fabrication of hollow waveguides for CO<sub>2</sub> lasers. *Appl. Opt.* 39 (10), 1555–1560. <https://doi.org/10.1364/ao.39.001555>.
- Le, V.T., Ha, N.S., Goo, N.S., 2019. Thermal protective properties of the allomyrina dichotoma beetle forewing for thermal protection systems. *Heat Tran. Eng.* 40, 1539–1549. <https://doi.org/10.1080/01457632.2018.1474603>.
- Leonhardt, U., Tyc, T., 2009. Broadband invisibility by non-Euclidean cloaking. *Science* 323 (5910), 110–112. <https://doi.org/10.1126/science.1166332>.
- Millott, N., 1968. The dermal light sense. In: *Symp. Zool. Soc. London*, pp. 1–36.
- Milošević, M.M., Man, W., Nahal, G., Steinhardt, P.J., Torquato, S., Chaikin, P.M., Amoah, T., Yu, B., Mullen, R.A., Florescu, M., 2019. Hyperuniform disordered waveguides and devices for near infrared silicon photonics. *Sci. Rep.* 9 (1), 1–11. <https://doi.org/10.1038/s41598-019-56692-5>.
- Mizuno, K., Ishii, J., Kishida, H., Hayamizu, Y., Yasuda, S., Futaba, D.N., Yumura, M., Hata, K., 2009. A black body absorber from vertically aligned single-walled carbon nanotubes. *Proc. Natl. Acad. Sci. Unit. States Am.* 106 (15), 6044–6047. <https://doi.org/10.1073/pnas.0900155106>.
- Nijhout, H.F., 1991. *The Development and Evolution of Butterfly Wing Patterns*, vol. 293. Smithsonian. Inst. Sch. Press.
- Parisi, V., Busetto, A., 1992. Revisione dei Coleotteri presenti nella collezione “A. Leosini”. Parte 2a. Scarabaeidae, Lucanidae, Cerambycidae. *Pubblicazioni del Museo di Storia naturale dell’Università di Parma* 5 (1), 1–93.
- Pitarma, R., Crisóstomo, J., Ferreira, M.E., 2019. Contribution to trees health assessment using infrared thermography. *Agriculture* 9 (8), 171. <https://doi.org/10.3390/agriculture9080171>.
- Polak, S., Maja, J., 2012. Phenology and mating behaviour of *Morimus funereus* (Coleoptera, Cerambycidae). *Saproxyllic beetles in Europe: monitoring, biology and conservation. Studia Forestalia Slovenica* 137, 43–52.
- Prokhorov, A., 2012. Effective emissivities of isothermal blackbody cavities calculated by the Monte Carlo method using the three-component bidirectional reflectance distribution function model. *Appl. Opt.* 51, 2322–2332. <https://doi.org/10.1364/AO.51.002322>.
- Romero-Samper, J., Bahülo, J., 1993. Algunas observaciones sobre la distribución y biología de *Morimus asper* Cerambycidae en la Península Ibérica. *Bol. Asoc. Esp. Entomol.* 17, 103–122.
- Scoble, M.J., 1992. *The Lepidoptera. Form, Function and Diversity*. Oxford University Press.
- Shi, N.N., 2018. *Biological and Bioinspired Photonic Materials for Passive Radiative Cooling and Waveguiding*. Doctoral dissertation. Columbia University.
- Shi, N.N., Tsai, C.C., Camino, F., Bernard, G.D., Yu, N., Wehner, R., 2015. Keeping cool: enhanced optical reflection and radiative heat dissipation in Saharan silver ants. *Science* 349 (6245), 298–301. <https://doi.org/10.1126/science.aab3564>.
- Solano, E., Mancini, E., Ciucci, P., Mason, F., Audisio, P., Antonini, G., 2013. The EU protected taxon *Morimus funereus* Mulsant, 1862 (Coleoptera: Cerambycidae) and its western Palaearctic allies: systematics and conservation outcomes. *Conserv. Genet.* 14 (3), 683–694. <https://doi.org/10.1007/s10592-013-0461-3>.
- Stabentheiner, S., Schmaranzer, A., 1987. Thermographic determination of body temperatures in honey bees and hornets: calibration and applications. *Thermology* 2, 563–572.
- Stabentheiner, A., Kovac, H., Hetz, S.K., Käfer, H., Stabentheiner, G., 2012. Assessing honeybee and wasp thermoregulation and energetics - new insights by combination of flow-through respirometry with infrared thermography. *Thermochim. Acta* 534, 77–86. <https://doi.org/10.1016/j.tca.2012.02.006>.
- Stanić, V., Ivanović, J., Janković-Hladni, M., Nenadović, V., Marović, R., 1985. Feeding habits, behavior, oviposition and longevity of the adult cerambycid beetle *Morimus asper funereus* Muls. (Col., Cerambycidae) under laboratory condition. *Acta Entomol. Jugosl.* 21, 87–94.
- Sun, J., Bhushan, B., 2012. Structure and mechanical properties of beetle wings: a review. *RSC Adv.* 2 (33), 12606–12623. <https://doi.org/10.1039/c2ra21276e>.
- Sun, J., Liu, C., Bhushan, B., Wu, W., Tong, J., 2018. Effect of microtrichia on the interlocking mechanism in the Asian ladybeetle, *Harmonia axyridis* (Coleoptera: Coccinellidae). *Beilstein J. Nanotechnol.* 9 (1), 812–823. <https://doi.org/10.3762/bjnano.9.75>.
- Sweeney, A., Jiggins, C., Johnsen, S., 2003. Polarized light as a butterfly mating signal. *Nature* 423, 31–32. <https://doi.org/10.1038/423031a>.
- Tucolesco, J., 1933. La dynamique de la larve de *Tenebrio molitor* et la théorie des tropismes. *Bull. Biol.* 4, 1–35.
- Unruh, T.R., Chauvin, R., 1993. Elytral punctures: a rapid, reliable method for marking Colorado potato beetle. *Can. Entomol.* 125 (1), 55–63.
- van de Kamp, T., Greven, H., 2010. On the architecture of beetle elytra. *Entomol. Heute* 22, 191–204.
- van de Kamp, T., Riedel, A., Greven, H., 2016. Micromorphology of the elytral cuticle of beetles, with an emphasis on weevils (Coleoptera: Curculionidae). *Arthropod Struct. Dev.* 45 (1), 14–22. <https://doi.org/10.1016/j.asd.2015.10.002>.
- Verstraete, C., Mouchet, S.R., Verbiest, T., Kolaric, B., 2019. Linear and nonlinear optical effects in biophotonic structures using classical and nonclassical light. *J. Biophot.* 12, 1–13. <https://doi.org/10.1002/jbio.201800262>.
- Vollmer, M., Möllmann, K.P., 2010. *Infrared Thermal Imaging: Fundamentals, Research and Applications*. John Wiley & Sons.
- Vukusic, P., Sambles, J.R., 2003. Photonic structures in biology. *Nature* 424 (6950), 852–855. <https://doi.org/10.1038/nature01941>.
- Vukusic, P., Sambles, J.R., Lawrence, C.R., Wootton, R.J., 2001. Now you see it - now you don't. *Nature* 410 (6824). <https://doi.org/10.1038/35065161>, 36–36.



Cite this: *Soft Matter*, 2021, 17, 6477

## Synergy of interference, scattering and pigmentation for structural coloration of *Jordanita globulariae* moth

Danica Pavlović,<sup>a</sup> Svetlana Savić-Šević,<sup>a</sup> Branislav Salatić,<sup>a</sup> Vladimir Lazović,<sup>a</sup> Wang Zhang,<sup>b</sup> Di Zhang<sup>b</sup> and Dejan Pantelić<sup>a</sup>

Structural and pigment colorations are omnipresent in insects, producing a range of colors for camouflage, warning, mimicry and other strategies necessary for survival. Structural coloration has attracted a lot of attention due to its significance in biophotonics, biomimetics and even esthetic appeal. The coupling of structural and pigment colorations has been largely unnoticed. Herein we show how pigments, scattering and interference work together in two-dimensional waveguiding structures to produce the coloration of *Jordanita globulariae* (Huebner, 1793), a moth whose forewings sparkle with slightly iridescent green scales. We show that subwavelength structures scatter and couple light into a concave multilayered structure to enhance the absorption of pigments. A finite element method (FEM) model, adequately describing the photonic properties of *J. globulariae*, was developed based on the nanoscale architecture of the insect's wing scales. The principle of absorption enhanced by scattering and waveguiding is present in many insect species and might be imitated to tailor the spectral properties of optical devices.

Received 29th January 2021,  
Accepted 25th May 2021

DOI: 10.1039/d1sm00157d

[rsc.li/soft-matter-journal](http://rsc.li/soft-matter-journal)

### 1. Introduction

Animals produce colors in two fundamentally different ways: by pigments and structurally. Most animals have pigmentary coloration that is based on the selective absorption of a certain range of wavelengths. However, the most intense and brightest colors are structural. They result from the interaction of light with micro- and nanostructures comparable with visible wavelengths.<sup>1</sup>

Pigment coloration is prevalent, except for blue and green, which seem to be rare, but nonetheless can be found in some vertebrates,<sup>2</sup> the most notable being the green coloration of frogs.<sup>3</sup> The same is true for insects, whose blue-green colors can be produced by bile pigments such as pterobilin, phorbabilin and sarpodobilin. Some butterfly species have a bluish- or greenish-pigmented hue obtained by bile pigments (seen in two Papilionidae genera: *Papilio* and *Graphium*). Pigmented blue has not been found in other insects.<sup>4</sup> Structural coloration seems to be an alternative, evolutionarily developed, way to generate shiny, pronounced shades of arbitrary colors, including blues and greens.

There are many different studies and advanced techniques dealing with structural coloration.<sup>5,6</sup> The genesis of green coloration is particularly interesting because of its significance in camouflage. Structural green sometimes arises solely from photonic structures<sup>7,8</sup> or due to color mixing within concave structures (as in the wing scales of some Papilionidae species (Lepidoptera) and Cicindelidae (Coleoptera)).<sup>9,10</sup> It is worth noting that green may be a result of the color-mixing of structural blue and pigmentary yellow.<sup>11,12</sup>

Such a peculiar coloration is even more interesting if it is found on the wings of moths (Heterocera: Lepidoptera). Moths are mostly nocturnal, and therefore, generally drab in color (brown or grey). However, there are some moth species that possess attractive coloration such as the tropical Madagascan sunset moth.<sup>13</sup> There is also a whole group of colorful, day-flying moths of the Zygaenidae family. The majority of zygaenids are tropical, but they are nevertheless quite well represented in temperate regions. The species *Jordanita globulariae* (subfamily Procrinae) caught our attention because of the dull, slightly iridescent green coloration of its forewings.

In this study we reveal the structure and function of the scales of the *Jordanita globulariae* moth through morphological characterization, spectral measurement and numerical simulation. The synergistic operation of structure and pigments is analyzed. We also discuss the role of this particular coloration in the moth's lifestyle.

<sup>a</sup> Institute of Physics Belgrade, Pregrevica 18, 11080 Zemun, Belgrade, Serbia.  
E-mail: danica.pavlovic@ipb.ac.rs

<sup>b</sup> State Key Lab of Metal Matrix Composite, Shanghai Jiao Tong University, 800 Dongchuan Road, Shanghai 200240, China



## 2. Materials and methods

### 2.1 Specimen details

*Jordanita globulariae* (Fig. 1) is a day-flying moth (fam. Zygaenidae, subfam. Procridinae). The species is widespread from the Iberian Peninsula in the west to the Urals in the east of Europe. The forewing's length is 10.5–17 mm in males and 7.7–10.1 mm in females. It flies during the sunny days from May to August, usually in limestone pastures.<sup>14</sup> Larvae are fed on species from the genera *Centaurea* L., *Cirsium* and *Globularia* L. On very hot days, the moth usually perches on flowers and other vegetation. Males occasionally fly at night.<sup>15</sup> Adults of this moth have green forewings, while the hind ones are grey-brown. When at rest, the hindwings are completely obscured under the green forewings, enabling the insect to hide in foliage. Several species within this family have similar morphological characteristics [e.g. *Adscita statices* (Linnaeus, 1758)]. We had three, conserved and pinned *J. globulariae* specimens at our disposal, collected during May and June of 2011 on Mt. Fruška Gora, near the city of Novi Sad, Serbia (leg. D. Stojanović).

### 2.2 Microscopy and spectroscopy

Field-emission gun scanning electron microscope (FEGSEM) (MiraSystem, TESCAN) was used to study the fine anatomy of the moth scales. Dried insect forewings were mounted and sputter-coated with 5–10 nm of Au/Pd in preparation for SEM. We used an Au/Pd target because it has a smaller grain size and it is the recommended metal coating for a wide range of sample types.

Individual scales were prepared for SEM by the double transfer method: a scale was detached with a low-surface-energy adhesive ("Post-it" sticky note), followed by transfer to a high-surface-energy tape (conductive carbon). In this way, the original scale orientation was preserved. During this process some of the scales were mechanically broken, revealing the inner structure and cross section of the scales.



Fig. 1 *Jordanita globulariae* with structurally green dorsal sides of the forewings.

Optical characteristics of the wings and scales were analyzed on a trinocular microscope MET104 (Colo Lab Experts) with a Plan Achromatic POL Polarizing objective lens (10X/20X/40X).

To record reflectance spectra, we used a fiber optic spectrometer (Ocean Optics, HR2000CG-UV-NIR) with a 400  $\mu\text{m}$  core diameter fiber. A halogen lamp was used as a light source and spectra were referenced to a standard white surface. Angular variation of the reflectance spectra was measured with a stationary sample illuminated by the light source at normal incidence. The spectrometer fiber was rotated within the angular range from  $10^\circ$  to  $50^\circ$ .

### 2.3 Optical modeling

A finite element method (FEM) was used to model the interaction of visible light with wing pigmented scale nanostructures. The model is two-dimensional because it saves computation time, which was approximately 20 min on our PC. It would be difficult to model the exact shape of photonic structures that are certainly not spherical, but somewhat irregular, rather oval and elongated along one axis (Fig. 2(b) and 3(a)). Thus, a 2D model (which is equivalent to a 3D infinite cylinder) is a satisfactory approximation, as the photonic structure studied here departs significantly from cylindrical only at its edges. The arrayed structure of wing scales is modeled using one unit cell with periodic boundary conditions. Perfectly matched layers (PMLs) are placed above and below the structure in order to minimize any reflected signal. In the model, the average mesh size was manually set to one-fifth

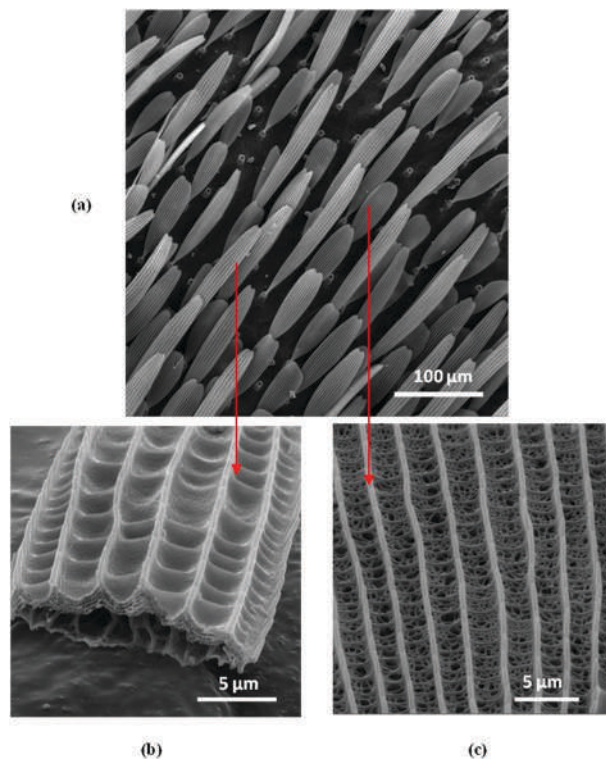


Fig. 2 (a) A SEM image of the *J. globulariae* forewing with two types of scales. Magnified SEM images of: (b) a long scale covered with several cup-shaped dips and (c) a short scale with a random, sponge-like structure.

of the minimum incident wavelength, which was 400 nm in our case. However, mesh density was adaptively adjusted to correctly model the tiniest structures of the model. To create a numerical simulation, it is necessary to know the complex refractive index of the biological structure. It is difficult to know the exact value, but we found that modest variation ( $\Delta n \sim \pm 0.03$ ) of the refractive index has only a slight impact on simulations. The real part of the complex refractive index was taken from the literature:  $n = 1.57$ .<sup>16,17</sup>

The extinction coefficient was determined experimentally by measuring the transmission of light through the structure and applying Beer–Lambert's law. We assumed that the structures analyzed here had a subwavelength size and could be regarded within the effective medium approximation. Imaginary part  $k$  of the refractive index was 0.011 at 400 nm, 0.019 at 500 nm and 0.01 at 800 nm.

### 3. Results

#### 3.1 Morphological and optical analysis of *J. globulariae* wing structures

The dorsal side of *J. globulariae* forewings is covered with scales that seem to be randomly distributed (Fig. 2(a)). The scales are either long with a regular internal architecture (Fig. 2(b)), or short with an irregular, sponge-like structure (Fig. 2(c)).

Long scales (with characteristic dimensions of approximately  $20 \mu\text{m} \times 150 \mu\text{m}$ ) seem to be more elaborate. At higher magnification (Fig. 3(a)), we can see that their upper lamina is ornamented with thin, lamellar ridges (separated by approximately  $3 \mu\text{m}$ ) connected by cross ribs. Together, ridges and cross ribs produce a sequence of concave dips (cup-like structures,  $0.5\text{--}3 \mu\text{m}$  deep) whose surface has a large number of tiny pores ( $20\text{--}50 \text{ nm}$ ). The interior of the whole scale is hollow, supported by large,  $1.5 \mu\text{m}$  high, trabeculae (Fig. 3(a)) connecting the upper and lower lamina (which is irregular, single-layered and about  $100 \text{ nm}$  thick).

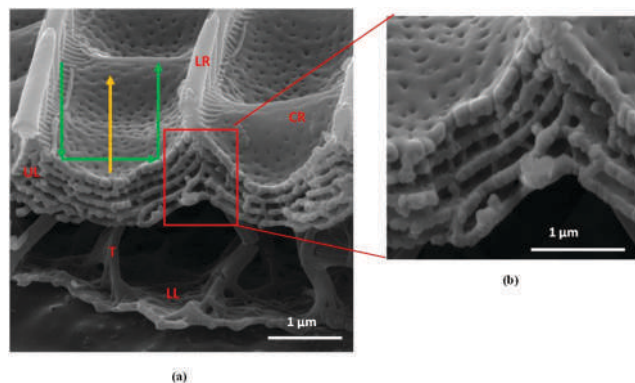


**Fig. 3** SEM image of *J. globulariae* long wing-scale structure. (a) A cross section of the scale showing concave, multilayered upper lamina and single-layer lower lamina separated by trabeculae (LR – lamellar ridges; CR – cross ribs; T – trabeculae; UL – upper lamina; LL – lower lamina). Green and yellow arrows indicate different wavelengths for radiation hitting the structure at its center or its edges. (b) A concave multilayer of the upper lamina with five chitin layers.

The cross section of the scale (Fig. 3(b)) shows the concave upper lamina with five chitin layers whose thickness is approximately  $110 \text{ nm}$ . They are mutually separated by tiny, pillar-like structures, producing  $90 \text{ nm}$ -thin, air-filled, voids. This arrangement will be further considered as a curved multilayer serving as a specific, spectrally selective, filter.

On the other hand, short scales (whose approximate size is  $40 \mu\text{m} \times 80 \mu\text{m}$ ) are quite different. They are almost hollow, filled with an intricate, irregular, sponge-like structure (Fig. 4(a) and (b)), but surface ridges and cross ribs can be seen as well.

From an optical point of view, the green color of the insect is diffuse, dim and slightly iridescent (Fig. 1) – *i.e.* we were able to observe a significant color shift only for large, almost grazing, angles of observation. If observed through an optical microscope, long scales reflect, while short ones absorb light (Fig. 5). If the image of a long scale is further magnified (inset in Fig. 5), a number of discrete blue-green and yellow dots can be seen.

Comparing SEM and optical images, we can see accurate matching between the morphology of long scales and the observed optical pattern. It is well known that the spectral reflection of a layered structure is influenced by the distance between the layers, the refractive index and the angle of incidence. In this case, reflection is strongly affected by the concave shape of the layers. We can see that light falling on the center of the concavity has a different angle of incidence compared to off-center zones. This is why we observe differently colored spots in the inset of Fig. 5. Macroscopically, colors are mixed to produce the insect's green color.

Apart from structural coloration, scales are slightly pigmented, as can be seen from the transmission optical image (Fig. 6(a) – scales were immersed in an index matching fluid to suppress Fresnel reflections). Interestingly, the long (structurally colored) scale has significantly higher (0.25) absorption than the short (nonstructural) one (0.16).

Absorption is much higher in the blue part of the spectrum and decreases towards the green-red part (as can be seen in Fig. 6(b)). We found that the average coefficient of absorption is between  $0.35 \text{ 1}/\mu\text{m}$  in the blue part of the spectrum and  $0.1 \text{ 1}/\mu\text{m}$  in the red. All the above facts signify that the effect of pigments cannot be disregarded, as we will further show.

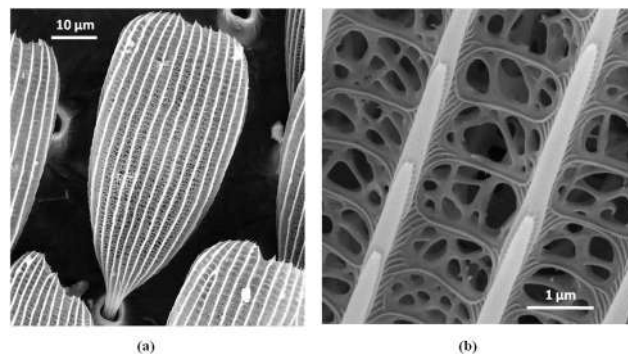


**Fig. 4** SEM images of (a) a short wing scale of *J. globulariae* and (b) its hollow, sponge-like internal structure.

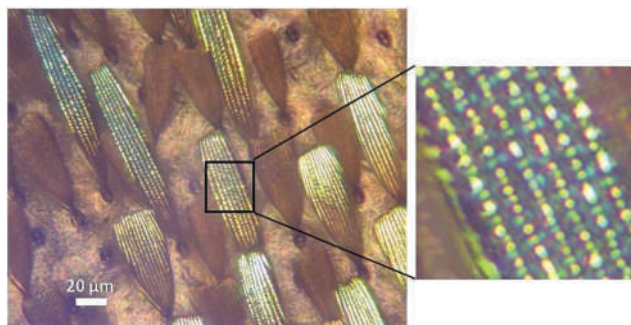
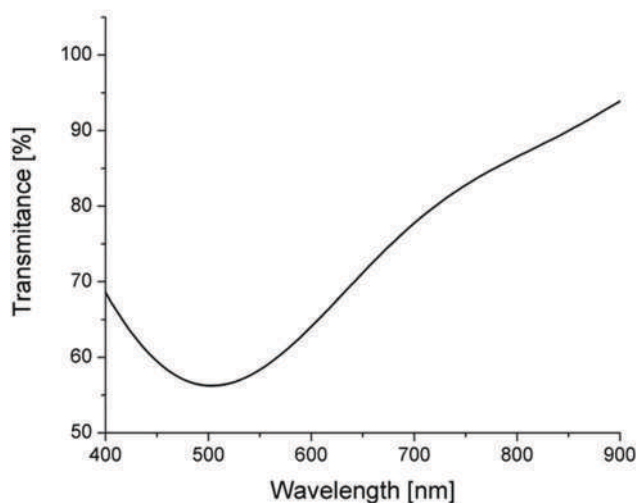


Fig. 5 Optical micrograph of *J. globulariae* wing scales. An enlarged part of a structurally colored one is shown on the right (with yellow and blue-green dots).



(a)



(b)

Fig. 6 *J. globulariae* moth: (a) Transmission optical image of long (L) and short (R) scales. (c) Transmittance spectrum of the long, structurally colored scale.

We measured the angular variation of the spectrum by rotating the detector (spectrometer fiber) and keeping the wing and illuminator positions fixed. Illumination was at normal incidence with respect to the wing. The reflection was recorded within the angular range of 10–50 degrees. Under these conditions we observed a slight spectral shift of 40 nm (Fig. 7(a)). This corresponds to the perception of unsaturated green color,

irrespective of the angle of observation. As a final remark, we emphasize that the spectrum fits nicely into the spectrum of foliage (Fig. 7(b)), enabling the insect to hide effectively in its natural environment.

### 3.2 Optical modeling of *J. globulariae* wing scales

Here we present an optical model of structurally colored scales (Fig. 8(a)) designed to simulate all the characteristic features observed in SEM images (Fig. 3):

- concave dip (1.5  $\mu\text{m}$  radius) with five chitin layers, 110 nm thick, and refractive index 1.57;
- layers separated by (20 nm  $\times$  90 nm) producing 90 nm air spaces;
- outer surface with a number of 10 nm-diameter holes.

On this basis, we will establish a link between the architecture and the optical response of wing scales.

In a simplified model and before going into more detail, we will approximate the structure with a collection of Bragg gratings with different orientations. According to Bragg's law:

$$\lambda = 2nd \cos \theta \quad (1)$$

where  $\lambda$  is the wavelength of multilayer reflectance maximum,  $d$  is the grating period,  $n$  is the effective refractive index of the grating, and  $\theta$  is the angle of incidence of radiation. Observe that the incident plane wave irradiates the concave structure within the range of angles – 0 degrees in the center and 50 degrees at the edges. At the center of a concave dip (angle of incidence  $\theta = 0^\circ$ ) the Bragg wavelength can be estimated at 520 nm (assuming a grating period of 200 nm and an effective refractive index of 1.3). Towards the edge, the Bragg resonance drops to 370 nm. Due to only five Bragg layers, the reflection maxima are broad (Fig. 8(b)) and the resulting spectra cover the UV-blue part of the spectrum.

We can conclude that, without an additional mechanism, *J. globulariae* wings will evenly reflect visible light, making the insect appear to be bluish. Absorption alone is not enough to modify the reflection spectrum due to the thinness of individual scales and small amount of pigment (Fig. 6). In the following we will prove that scattering amplifies absorption in accordance with the theory of Yablonovitch described in ref. 18. It was shown that rough surfaces amplify the radiation intensity within planar layers by  $2n^2$  factor, where  $n$  is the refractive index of the material. This leads to increased absorption of up to  $4n^2$  times compared to ideally flat layers. For chitinous structures of scales ( $n = 1.57$ ), absorption may thus increase up to 9.9 times.

The Yablonovitch theory is universally applicable to layers of any thickness, as it is based on the basic laws of radiation. For subwavelength multilayer structures, as is the case here, the effects of evanescent waves certainly lead to radiation being redistributed among the layers. However, the total thickness of all layers taken together is significantly larger than the wavelength and the radiation stays entrapped and waveguided. Here we add that the theory is limited to randomly distributed (Lambertian) incoming radiation. This is usually the case for the environmental, solar, irradiation omnipresent in most natural surroundings. We have previously used the theory to



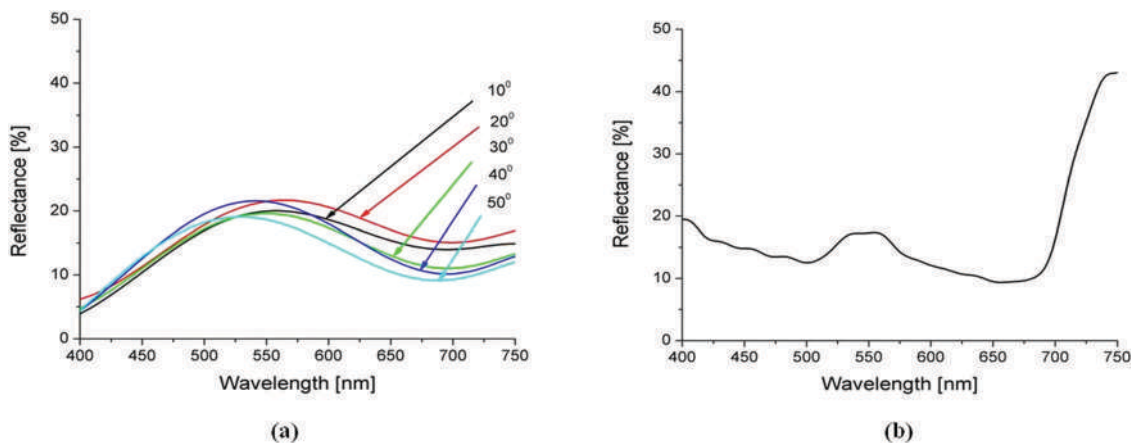


Fig. 7 (a) A slight angular variation (within a 10–50° range) of the *J. globulariae* wing reflectance spectrum. (b) A reflectance spectrum of the green leaves of Hibiscus.

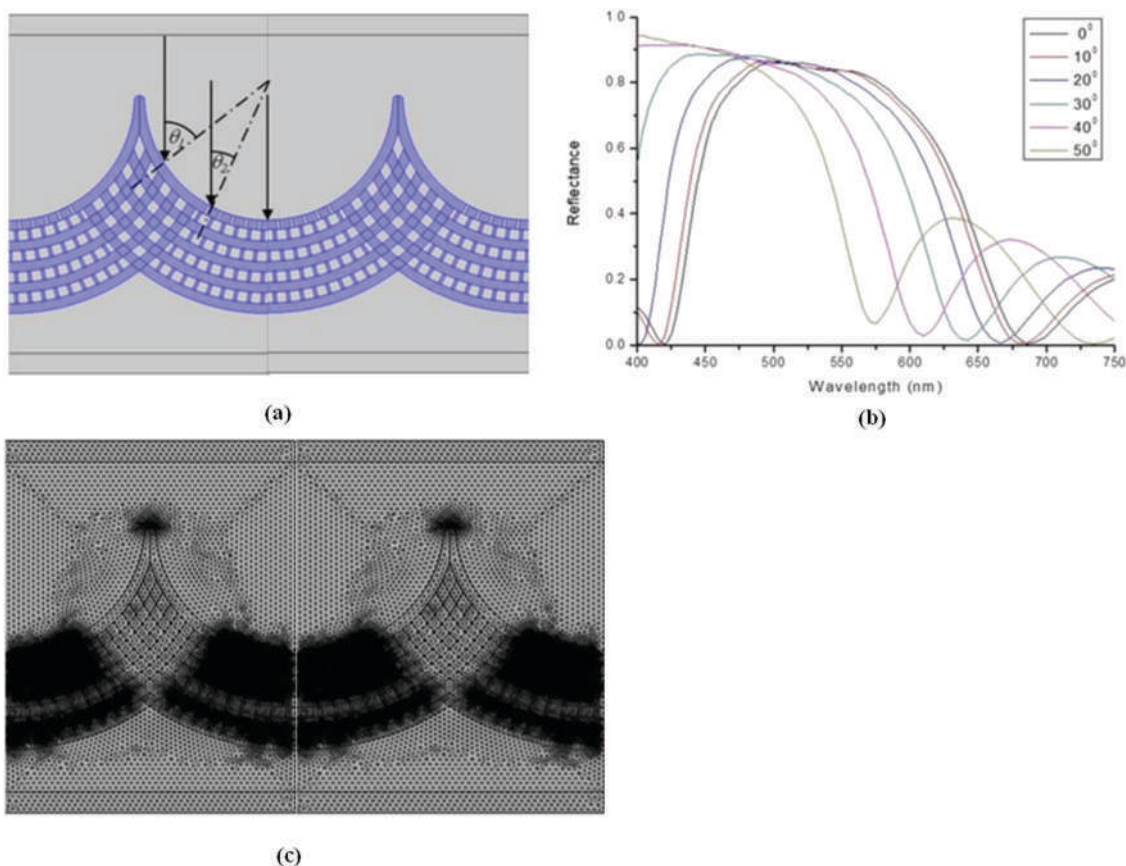


Fig. 8 (a) Geometry of a concave multilayer model used in FEM. Arrows indicate the radiation direction and  $\theta$  is the angle of incidence. (b) Strong spectral shift for different angles of incidence. (c) A model, depicted in (a), is adaptively meshed for correct FEM analysis of the smallest features.

explain a golden coloration of rather simple wing scales of *Diachrysis chrysitis* moths.<sup>19</sup>

In the case of *J. globulariae* wing scales, scatterers are numerous and include nanometer scale pits on the surface, nanopillars between the layers and many of the other defects of otherwise regular structures. The whole problem is too

complicated to be analyzed analytically because it includes the effects of scattering on subwavelength structures, spectrally dependent absorption, waveguiding and radiation localization, as well as interference effects on a very specific concave Bragg grating. This is why we had to use FEMs to calculate the reflection spectrum of the scales. A model in Fig. 8(a) was

adaptively meshed (*i.e.* finer structures were meshed more densely – Fig. 8(c)) in order to obtain the correct results.

First, we calculated the electromagnetic intensity distribution (square of the amplitude) without taking into account absorption (Fig. 9(a)). We clearly observed the localization of the field within the concave Bragg structure due to wave-guided modes. They were introduced into the structure because of scattering on subwavelength structures (pillars and pits) in accordance with the Yablonovitch theory. Resulting spectra are wide and independent on the angle of incidence (Fig. 9(b)).

If absorption is introduced into the model, in accordance with the characteristics of real scales, we can clearly see that waveguided modes are strongly absorbed (Fig. 9(c)) and the resulting spectra are narrowed (Fig. 9(d)) and independent on the angle of illumination, to match those observed experimentally (Fig. 7(a)). This is in stark contrast to the completely flat Bragg grating – its reflectance is very high (up to 90%) but its angular dependence is significant (the shift is larger than 150 nm).

It seems that natural evolution has brought about a nicely balanced set of features: concave structures to induce angular insensitivity of coloration, residual pigments to absorb light and subwavelength structures to enhance scattering and waveguiding. As a result, *J. globulariae* becomes quite inconspicuous within its environment.

We can note that theoretical spectra have a number of local minima and maxima, resulting from a very complex structure with many resonances (Fig. 9(b) and (d)). In reality, the resulting spectrum is obtained by reflection from a large number of scales. They are not identical, and the resonances are averaged to produce a smooth curve as in Fig. 7(a).

To further refine the model, we sliced a spherical multilayer into 8 planar cross-sections and approximated each one as a collection of cylindrical layers (as shown in Fig. 10(a)). Due to symmetry of the structure, there were only 4 different sections (designated 1–4 in Fig. 10(a)) to which we applied an FEM technique in the manner described above. By averaging spectral distributions of all cross sections, we obtained the resulting spectrum in Fig. 10(b), which is comparable to the experimentally recorded curves in Fig. 7(a).

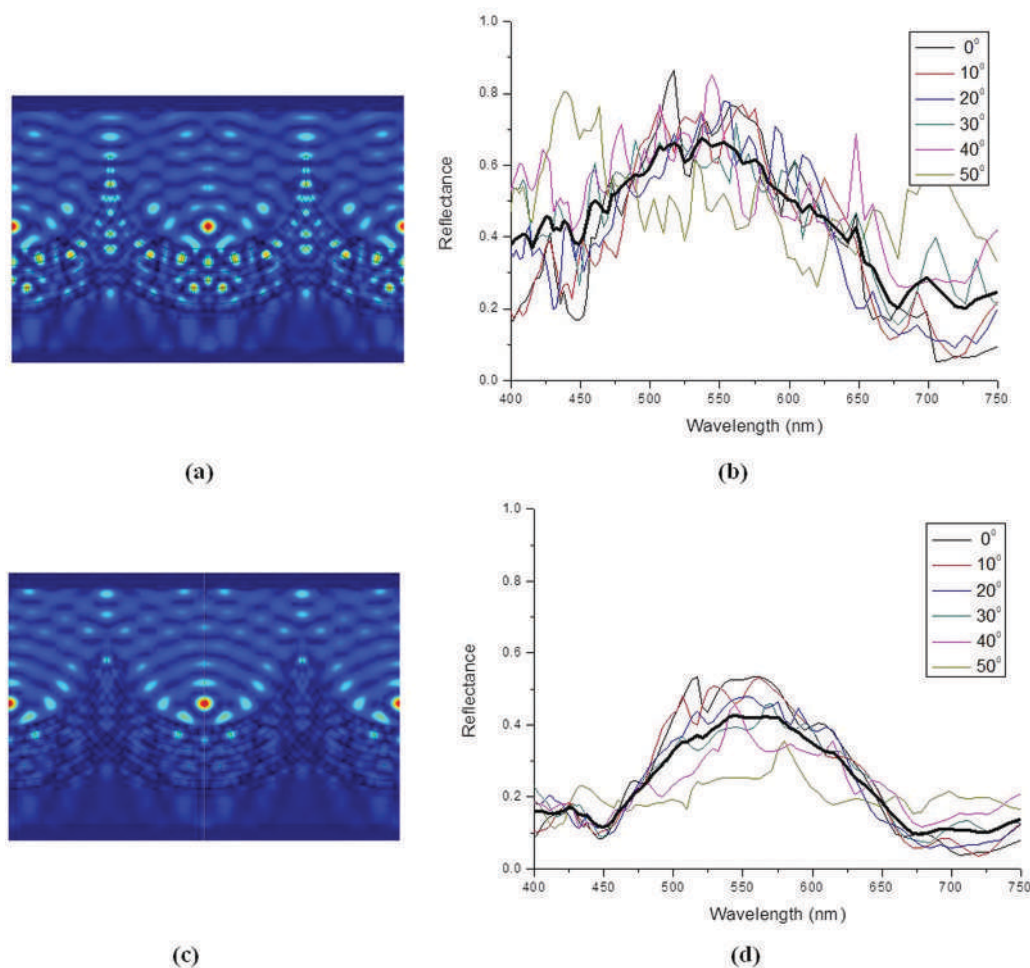


**Fig. 9** (a) Strong localization of the electromagnetic field ( $\lambda = 479$  nm) inside the structure (WITHOUT pigmentation taken into account), and (b) the corresponding spectra at different angles of incidence. (c) Absorption of a localized electromagnetic field ( $\lambda = 479$  nm) inside the structure (WITH pigmentation taken into account), and (d) the corresponding spectra at different angles of incidence.

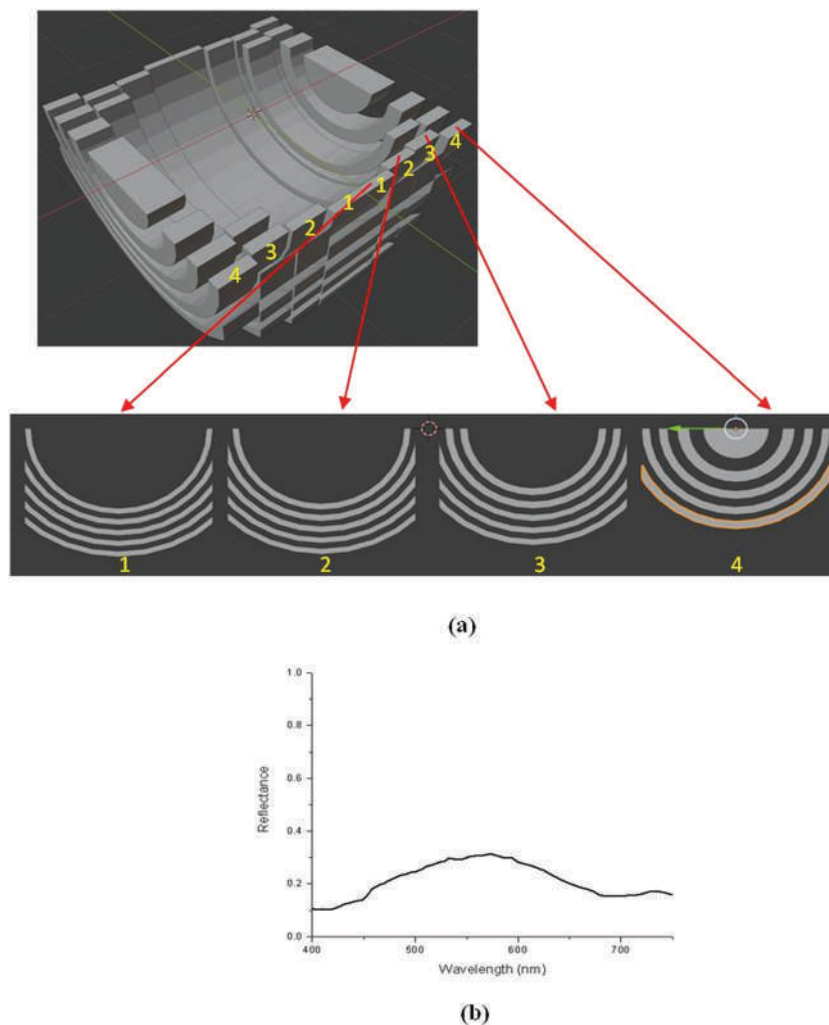


Fig. 10 (a) A characteristic multilayer dip of *J. globulariae* wing scale is modeled as a collection of cylindrical cross-sections designated by numbers 1–4. (b) The resulting spectral distribution, obtained by angular averaging spectra of cross-sections 1–4.

## 4. Discussion

We have shown that the wings of the *J. globulariae* moth possess a set of structural features that produce a slightly iridescent (*i.e.* observable only at grazing incidence) green structural color. This is important for a day-flying insect to remain unseen on the green background of vegetation. To do this, wings evolved with low angular variation and reflectance comparable to that of green surroundings.

Similar structural coloration was also observed in other insects. It was found that *Papilio palinurus* produces its green coloration as a result of color mixing between reflected and retroreflected light from a concave multilayer structure.<sup>10</sup> There, the effects of scattering and pigmentation were not analyzed, and the coloration was explained solely by the multilayer interference.

The question of adequate modeling is an important (and still open) problem for understanding the interaction of light with biophotonic structures. Three-dimensional modeling is extremely demanding, with respect to execution time and

memory requirements. Massively parallel computers are used with computational time of the order of several hours (for a single 3D geometry and single wavelength) and tens (even hundreds) of gigabytes of working memory.<sup>7</sup>

Overall architecture of *J. globulariae* structures is variable – ranging from almost spherical to cylindrical, with several layers and a number of randomly distributed nano-pillars and holes. Such complexity is beyond the capability of most computers. Even the fastest ones are incapable of calculating irregular, stochastically distorted, nano-patterned geometries on a reasonable timescale. Here, we used 2D, cylindrical models of essentially three-dimensional structures. This is quite sufficient for oblong structures, while for those closer to spherical symmetry, a dip was sectioned in order to make the approximation more adequate. Anyway, optical microscopy (Fig. 5) shows that the overall optical effect is quite tolerant to random variation of size, shape and nanostructure. The computational results presented here confirm that slightly absorbing nanostructures restrict the radiation to the green-red part of the spectrum



(compare Fig. 9(b) and (d)) in accordance with the theory of absorption enhancement by scattering.

The role of pigments was analyzed in ref. 20. The authors described the *Eudocima materna* moth whose cover scales act as an interference mirror (not the multilayer one), while ground scales are strongly pigmented. For certain angles of observation, cover scales mirror the incoming radiation, thereby making underlying pigmented scales invisible. For other angles, radiation is redirected by the mirror scales outside the viewing direction, making the underlying pigmented scales visible. Again, interference, scattering and absorption are not interlinked and enhanced.

A somewhat different analysis of the interplay between wing coloration and visual pigments was performed in ref. 21. It was found that additional visual pigment in the photoreceptors of Lycaenidae is well tuned to the characteristic structural coloration of butterflies within this family.

A good overview of photonic structures has been given in ref. 22. The authors remark that green pigments are absent in butterfly wing scales and analyze blackness and fluorescence enhancement caused by structures.

Structures at all dimensional scales are included and work in synergy to produce the coloration of *J. globulariae*. At the molecular level, dark pigments (melanin) are needed to selectively absorb the blue part of the spectrum. However, in this particular insect there is only a small amount of pigment, which is not enough to significantly absorb the blue part of the spectrum as shown in Fig. 9(b). Therefore, nanoscales, pillars, pits and other subwavelength structures are necessary to preferentially scatter blue light and enhance its absorption. Micron-sized concave multilayers selectively filter the red part of the spectrum while making it angularly independent.

On a higher scale (in the order of hundreds of micrometers and millimeters), the wing as a whole must be accounted for. Our model shows that the reflectivity of a single structural scale is in the order of 40% (Fig. 9(d)). However, the reflectivity of the wing is much lower (20–25%, Fig. 7) as a result of sparse scale population, attenuation by nonstructural scales and the wing membrane. The resulting value corresponds well to the reflectivity of vegetation, making the insect almost invisible in its environment. We have calculated the CIE xy color coordinates of the green leaves of *Hibiscus*.<sup>23,24</sup> *J. globulariae* and our model show how well nature has “adjusted” the insect to the environment (Fig. 11). Here, a CIE diagram is used as a simple way to compare complex spectra, not as a measure of human color perception, which is certainly quite different compared to that of insects.

For reference, we have shown the color coordinates of a model without scattering and absorption. In this case, the insect's color would have been blue, making it highly visible.

In this paper we had no space to analyze the “nonstructural” scales, but it seems that there are structural effects too. By looking closely at Fig. 6(a), we can see that the absorption of a nonstructural scale is lower than that of the structural one, yet it is highly absorbing on the wing (Fig. 5). It seems that scattering enhances the absorption of the rather hollow structure of a “nonstructural” scale as well.

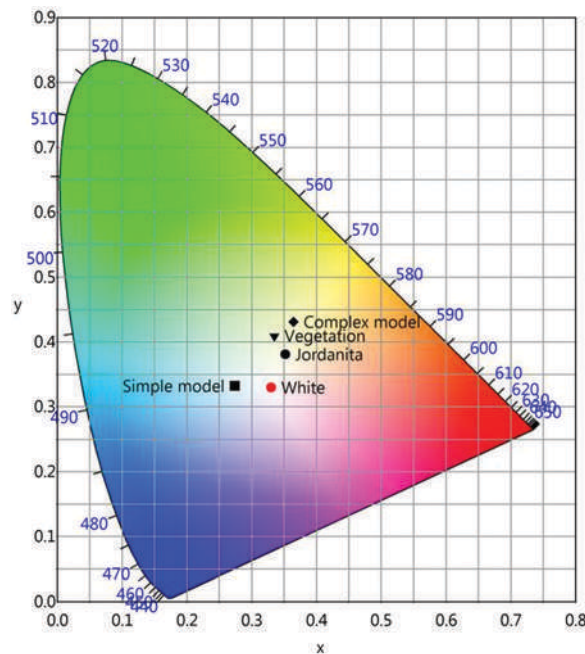


Fig. 11 A CIE diagram showing the xy chromatic coordinates of vegetation, *J. globulariae* and a complex model (concave layer with scattering structures and absorption). Coordinates of achromatic white and a simple, flat, layer model have been shown for reference.

From a biological point of view, the color green usually has a cryptic role in insects,<sup>25–27</sup> providing very effective camouflage among leaves. This greenish color, which is not highly reflective, indicates a primary defensive role in *J. globulariae*. Slight iridescence and color contrast, which are very important in communication between species, further speak in favor of the protective role of such an optical signal.<sup>28</sup>

On the other hand, species of this family (including *J. globulariae*) also possess a chemical defense mechanism. All Zygaenidae<sup>15</sup> contain hydrogen cyanide (HCN), taken from plants or synthesized from plant glucose.<sup>29</sup> Therefore, they are poisonous or, at least, distasteful to potential predators. Sending a warning is another reason why the species of this family may have such coloration. The color green becomes highly visible during feeding on flowers<sup>14</sup> when it acquires its second, aposematic role.<sup>30</sup> Other examples are also known among Lepidoptera where warning and camouflage coloration are not contradictory.<sup>31</sup> We can therefore assume that the role of *J. globulariae* can be cryptic, when resting, hidden in leaves, and aposematic, during nectar feeding.

In most moths, the dorsal side of the front wings is visible during rest.<sup>32</sup> Given that all Zygaenidae are diurnal species, evolution has ensured that they have structural coloration only on the dorsal surface of their forewings.<sup>15</sup>

## 5. Conclusion

This paper reveals the delicate combination of interference, scattering, absorption and color mixing, all working together,

to facilitate the survival of *J. globulariae*. The fine tuning of many structural factors, from submicron to macroscopic levels, is amazing and its imitation provides a new way to control the spectral content of light.

## Conflicts of interest

There are no conflicts to declare.

## Acknowledgements

The authors acknowledge funding provided by the Institute of Physics, Belgrade, through a grant from the Ministry of Education, Science and Technological Development of the Republic of Serbia and the Science and Technology Development Program – Joint Funding of Development and Research Projects of the Republic of Serbia and the People's Republic of China: Mimetics of insects for sensing and security, No. I-2. DP acknowledges support from L'Oréal-UNESCO "For Women in Science". We express our gratitude to Dejan Stojanović from the Institute of Lowland Forestry and Environment, Novi Sad, Serbia, who donated *J. globulariae* specimens from his insect collection.

## References

- 1 J. Sun, B. Bhushan and J. Tong, *RSC Adv.*, 2013, **3**, 14862–14889.
- 2 J. T. Bagnara, P. J. Fernandez and R. Fujii, *Pigment Cell Res.*, 2007, **20**, 14–26.
- 3 C. Taboada, A. E. Brunetti, M. L. Lyra, R. R. Fitak, A. F. Soverna, S. R. Ron, M. G. Lagorio, C. F. B. Haddad, N. P. Lopes, S. Johnsen, J. Faivovich, L. B. Chemes and S. E. Bari, *Proc. Natl. Acad. Sci. U. S. A.*, 2020, **117**, 18574–18581.
- 4 P. Simonis and S. Berthier, How nature produces blue color. in *Photonic Crystals – Introduction*, ed. A. Massaro, Applications and Theory, InTech, Rijeka, 2012, pp. 3–24.
- 5 P. Kaspar, D. Sobola, P. Sedláč, V. Holcman and L. Grmela, *Microsc. Res. Tech.*, 2019, **82**, 2007–2013.
- 6 D. Sobola, S. Talu, P. Sadvovskiy, N. Papez and L. Grmela, *Adv. Electr. Electron. Eng.*, 2017, **15**, 569–576.
- 7 K. Michielsen, H. De Raedt and D. G. Stavenga, *J. R. Soc., Interface*, 2010, **7**, 765–771.
- 8 B. D. Wilts, K. Michielsen, J. Kuipers, H. De Raedt and D. G. Stavenga, *Proc. R. Soc. B*, 2012, **279**, 2524–2530.
- 9 S. Berthier, *Iridescences, les couleurs physiques des insectes*, Springer Science & Business Media, 2007.
- 10 P. Vukusic, J. R. Sambles and C. R. Lawrence, *Nature*, 2000, **404**, 457.
- 11 D. L. Fox, *Animal biochromes and structural colours: physical, chemical, distributional & physiological features of coloured bodies in the animal world*, University of California Press, 1976.
- 12 D. G. Stavenga, M. A. Giraldo and H. L. Leertouwer, *J. Exp. Biol.*, 2010, **213**, 1731–1739.
- 13 S. Yoshioka, T. Nakano, Y. Nozue and S. Kinoshita, *J. R. Soc., Interface*, 2008, **5**, 457–464.
- 14 K. A. Efetov and G. M. Tarmann, *Forester Moths: The genera Theresimima Strand, 1917, Rhagades Wallengren, 1863, Jordanita Verity, 1946, and Adscita Retzius, 1783 (Lepidoptera: Zygaenidae, Procrinae)*, Apollo Books, 1999.
- 15 C. M. Naumann, G. M. Tarmann and W. G. Tremewan, *The Western Palaearctic Zygaenidae (Lepidoptera)*, Apollo Books, 1999.
- 16 N. N. Shi, C. C. Tsai, F. Camino, G. D. Bernard, N. Yu and R. Wehner, *Science*, 2015, **349**, 298–301.
- 17 H. L. Leertouwer, B. D. Wilts and D. G. Stavenga, *Opt. Express*, 2011, **19**, 24061.
- 18 E. Yablonovitch and G. D. Cody, *IEEE Trans. Electron Devices*, 1982, **29**, 300–305.
- 19 D. Pantelić, S. Savić-Šević, D. V. Stojanović, S. Curčić, A. J. Krmpot, M. Rabasović, D. Pavlović, V. Lazović and V. Milošević, *Phys. Rev. E*, 2017, **95**, 032405.
- 20 J. L. Kelley, N. J. Tatarnic, G. E. Schröder-Turk, J. A. Endler and B. D. Wilts, *Curr. Biol.*, 2019, **29**, 2919–2925.
- 21 Z. Bálint, K. Kertész, G. Piszter, Z. Vértesy and L. P. Biró, *J. R. Soc., Interface*, 2012, **9**, 1745–1756.
- 22 L. P. Biró and J. P. Vigneron, *Laser Photonics Rev.*, 2011, **5**, 27–51.
- 23 C. Buschmann and E. Nagel, *Int. J. Remote Sens.*, 1993, **14**, 711–722.
- 24 C. Buschmann, S. Lenk and H. K. Lichtenthaler, *Isr. J. Plant Sci.*, 2012, **60**, 49–64.
- 25 F. Liu, H. Yin, B. Dong, Y. Qing, L. Zhao, S. Meyer, X. Liu, J. Zi and B. Chen, *Phys. Rev. E: Stat., Nonlinear, Soft Matter Phys.*, 2008, **77**, 1–4.
- 26 A. R. Parker, D. R. McKenzie and M. C. J. Large, *J. Exp. Biol.*, 1998, **201**, 1307–1313.
- 27 D. G. Stavenga, Surface Colors of Insects: Wings and Eyes, in *Functional Surfaces in Biology. Little Structures with Big Effects*, ed. S. N. Gorb, Springer, The Netherlands, 2009, vol. 1, 285–306.
- 28 P. Vukusic, J. R. Sambles, C. R. Lawrence and R. J. Wootton, *Proc. R. Soc. B*, 1999, **266**, 1403–1411.
- 29 O. Niehuis, S. H. Yen, C. M. Naumann and B. Misof, *Mol. Phylogenet. Evol.*, 2006, **39**, 812–829.
- 30 C. Wiklund and B. Sillen-Tullberg, *Evolution*, 1985, **39**, 1155.
- 31 K. L. Prudic, A. K. Skemp and D. R. Papaj, *Behav. Chem. Ecol.*, 2007, **18**, 41–46.
- 32 N. P. Kristensen, *Handbook of Zoology, Vol. IV, Part 3.: Lepidoptera: Moths and Butterflies. Morphology, Physiology, and Development*, Walter DeGruyter Press, Berlin, 2004.



## Photonic structures improve radiative heat exchange of *Rosalia alpina* (Coleoptera: Cerambycidae)



Danica Pavlović<sup>a,\*</sup>, Darko Vasiljević<sup>a</sup>, Branislav Salatić<sup>a</sup>, Vladimir Lazović<sup>a</sup>, Goran Dikić<sup>b</sup>, Ljubiša Tomić<sup>c</sup>, Srećko Ćurčić<sup>d</sup>, Petar Milovanović<sup>e</sup>, Dajana Todorović<sup>f</sup>, Dejan V. Pantelić<sup>a</sup>

<sup>a</sup> Photonics Center, Institute of Physics, University of Belgrade, Pregrevica 118, 11080 Zemun, Belgrade, Serbia

<sup>b</sup> The School of Electrical and Computer Engineering of Applied Studies, Vojvode Stepe 283, 11010 Belgrade, Serbia

<sup>c</sup> Military Technical Institute, Ratka Resanovića 1, 11030 Belgrade, Serbia

<sup>d</sup> Institute of Zoology, University of Belgrade - Faculty of Biology, Studentski Trg 16, 11000 Belgrade, Serbia

<sup>e</sup> Laboratory for Anthropology and Skeletal Biology, Institute of Anatomy, University of Belgrade – Faculty of Medicine, Dr Subotića 4/2, 11000 Belgrade, Serbia

<sup>f</sup> Department of Insect Physiology and Biochemistry, Institute for Biological Research “Siniša Stanković”, University of Belgrade, Despot Stefan Blvd. 142, 11060 Belgrade, Serbia

### ARTICLE INFO

#### Keywords:

Longicorn beetle  
Behavioral thermoregulation  
Structural coloration  
Texture enhanced absorption

### ABSTRACT

The insect cuticle serves a multitude of purposes, including: mechanical and thermal protection, water-repelling, acoustic signal absorption and coloration. The influence of cuticular structures on infrared radiation exchange and thermal balance is still largely unexplored. Here we report on the micro- and nanostructured setae covering the elytra of the longicorn beetle *Rosalia alpina* (Linnaeus, 1758) (Coleoptera: Cerambycidae) that help the insect to survive in hot, summer environments. In the visible part of the spectrum, scale-like setae, covering the black patches of the elytra, efficiently absorb light due to the radiation trap effect. In the infrared part of the spectrum, setae of the whole elytra significantly contribute to the radiative heat exchange. From the biological point of view, insect elytra facilitate camouflage, enable rapid heating to the optimum body temperature and prevent overheating by emitting excess thermal energy.

### 1. Introduction

Environment affects the body temperature of animals through thermal energy exchange. Animals have adapted to thermal conditions in order to maintain the optimal temperature of their bodies necessary for survival. This is why evolution has developed many ways to control heat transfer, e.g. bird feathers (Torre-Bueno, 1976), mammalian fur (Preciado et al., 2002) or subcutaneous fat of marine animals (Twiss et al., 2002), to mention just a few.

Insects have developed diverse thermoregulatory adaptations by physiological or behavioral means (Heinrich, 2013). Endothermic insects produce heat internally by physiological processes mostly associated with flying species, with moths and bees being the most common examples (Heinrich, 1974). However, the majority of insects are primarily ectothermic (Angilletta et al., 2002) and rely on external heat sources, such as solar radiation (Nijhout, 1991); for example, some butterflies regulate heat gain behaviorally, by orientation and posture relative to the sun (Kingsolver, 1985).

Insects exchange heat through the cuticle, whose color, structure

and material properties determine the amount of absorbed and dissipated energy. The cuticle is, thus, evolutionarily adapted to use available mechanisms of heat transfer (convection, conduction, radiation, transpiration) (Church, 1960), depending on the environmental conditions and the insect's lifestyle. The cuticle is often patterned on the micro- and nano-scale levels, producing natural photonic structures that strongly interact with light and electromagnetic wavesthrough absorption, interference, diffraction and scattering. The structures may have a variety of regular and stochastic architectures, such as diffraction gratings, layers, optical crystals that produce striking visual effects and act as selective optical filters, absorbers or antireflection coatings (Vukusic and Sambles, 2003; Vukusic et al., 2001).

Radiative transfer is an important, but often overlooked, mechanism used to heat or cool insects through the absorption (Scoble, 1992) and reflection of sunlight (Shi et al., 2015). In this respect, visible light is usually absorbed by pigments and selectively reflected by photonic structures (Vukusic et al., 2004; Biró et al., 2003). Infrared (IR) radiation is important too (Gallego et al., 2016), and some insects use it to receive energy from the environment, while others dissipate heat by

\* Corresponding author.

E-mail address: [danica.pavlovic@ipb.ac.rs](mailto:danica.pavlovic@ipb.ac.rs) (D. Pavlović).

<https://doi.org/10.1016/j.jtherbio.2018.07.014>

Received 5 April 2018; Received in revised form 7 June 2018; Accepted 22 July 2018

Available online 23 July 2018

0306-4565/ © 2018 Elsevier Ltd. All rights reserved.



radiating in the IR atmospheric window (Shi et al., 2015).

It was found that photonic structures of insects have an important function in this respect (Shi et al., 2015). To better understand the interaction of infrared radiation and biological structures, appropriate mathematical models are necessary. These are based on Kirchhoff's law of radiation, which establishes the equality of emissivity (as a measure of how effectively a body emits radiation) and absorptance. It is therefore sufficient to calculate the absorptance and unequivocally determine the emissivity. To do this, standard methods for calculating electromagnetic wave propagation have been used, such as scattering matrix methods to analyze butterflies in the IR (Herman et al., 2011), or a finite-difference time-domain technique to simulate the IR radiation transfer of Saharan silver ant (Shi et al., 2015).

The grayish body of the longicorn beetle *Rosalia alpina*, (Linnaeus 1758) (Coleoptera: Cerambycidae), with several prominent black patches on its elytra, attracted our attention. We studied the effect of cuticular setae (scale- and hair-like structures) on the absorptive and emissive properties of the cuticle and the overall thermal balance of the insect. In our previous conference paper (Dikić et al., 2016) we performed pulsed thermal imaging of this insect and presented the corresponding qualitative results. Here, our research is extended by (i) a new, well-controlled set of optical and thermal measurements, (ii) a detailed morphological analysis of photonic structures (elytral setae) and the development of a corresponding thermo-optical model, (iii) the contribution of biophotonic structures to the thermal balance of the insect under the high thermal load of direct, summer sunlight.

## 2. Materials and methods

### 2.1. Insect

*Rosalia alpina* is a longicorn beetle, characterized by a body length of 14–40 mm (antennae excluded), distinctive markings and coloration (Campanaro et al., 2017). The hind wings and abdomen are protected by subcylindrical blue-gray elytra (hardened forewings), with several dominating black patches (Fig. 1). The long antennae and legs have the same blue-gray coloration, with striking black tufts of hair-like structures on the central segments of the antennae. The specific, velvety appearance is created by a large number of very fine setae – transparent hair-like structures (hairs in the further text) on the blue-gray areas (Fig. 1), and dark, scale-like structures (scales in the further text) in the black patches (Fig. 1). They form a dense tomentum, which covers the body (Bense, 1995; Duelli and Wermelinger, 2005).

The species is strictly protected in Serbia and most of Europe by the Habitats Directive. Within the IUCN Red List of Threatened Species, it is designated as vulnerable (A1c) the IUCN Red List of Threatened Species, (2017). A limited number of insects was collected by the Faculty of Biology of the University of Belgrade during the summer of 2010 on Mt. Avala, near the city of Belgrade, with the permission of the Serbian Ministry of Environmental Protection (N<sup>o</sup>: 353–01-335/2010–03). We had five dry specimens at our disposal. The size of the insects was within the limits stated in (Campanaro et al., 2017). All our samples

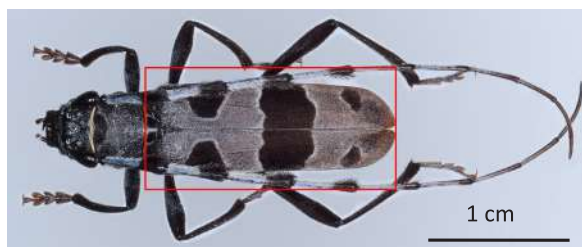


Fig. 1. *Rosalia alpina* is characterized by six prominent black patches and a blue-gray body. Elytra are shown within the red rectangle.

possess a common dorsal pattern with six, almost symmetrical black spots. The hind spots are the smallest while the mid spots are the largest (Fig. 1). It is known that variability among individuals is due to the size and shape of the elytral patches (Campanaro et al., 2017); however, the given variability is not important for the general thermal models in this study.

### 2.2. Microanalysis

We used reflection and transmission optical microscopy to study the optics of individual scales. A field emission gun scanning electron microscope (FEGSEM) (MiraSystem, manufactured by TESCAN) was used for ultrastructural analysis.

Micro-computed tomography (micro-CT) was employed to view the overall anatomy of the beetle and measure the thickness of the elytra. We had at our disposal the Skyscan 1172 system, manufactured by Bruker. To ensure the optimum signal/noise ratio during micro-CT imaging, the specimens were scanned without filter, with scanning parameters set as follows: 40 kV, 244  $\mu$ A, 530 ms, rotation step 0.2° (pixel size 13.5  $\mu$ m).

Microspectrometry was utilized to record spectral absorption due to pigmentary coloration. The device consisted of a fiberoptic spectrometer attached to an optical microscope.

### 2.3. IR analysis

Heat transfer was analyzed by two IR thermal cameras corresponding to atmospheric windows at 3–5  $\mu$ m (FLIR SC7200, 320  $\times$  256 pixels, noise equivalent temperature difference better than 20 mK, spectral range 1.5–5.1  $\mu$ m) and 8–14  $\mu$ m (FLIR SC620, 640  $\times$  480 pixels, 40 mK thermal resolution, spectral range 7.5–13  $\mu$ m). Thermal measurements were corrected for surface emissivity. To study radiative energy exchange, we used a xenon flashlamp (Bowens Gemini 1500Pro, pulse duration 0.9 ms, pulse energy 1.5 J) to uniformly irradiate the insect body. The elytra were also illuminated by a 405-nm wavelength laser in order to locally heat the black patch and study the thermal effects. Laser power was controlled by a variable beam splitter and the duration of irradiation by an Arduino microcontroller. A power-meter (Ophir, Nova, with photodiode sensor) was used to measure laser power.

The IR spectral properties of the insect elytra were recorded by the Fourier transform infrared (FTIR) system Nicolet 6700 FT-IR, Thermo Scientific, USA and analyzed by the OMNIC, software package, Version 7.0.

## 3. Results

### 3.1. Photonic structures of *R. alpina*

The elytra of *R. alpina* are in the form of a thin elongated shell, with six prominent black patches on a blue-gray background. The anatomy of a dried specimen was visualized using micro-CT at 13.5  $\mu$ m resolution (see Fig. 2(a)), revealing an almost uniform thickness (30–40  $\mu$ m) of the elytra (Fig. 2(b)). There is a large space between the elytra and the abdomen, where the hindwings are folded and packed, which functions as a thermally-insulating layer.

FEGSEM images revealed that the scales on a black patch are bunched on the elytra, inclined towards each other and touching at the tips, thus forming a number of tent-like structures (Fig. 3(a)). The scales stand almost vertically to the surface, as can be seen in Fig. 2(b) and its inset. The cuticle beneath is rugged, with irregular, polygonal impressions (Fig. 3(b)). The periodicity of scale placement (and that of the corresponding polygonal impressions) is between 10 and 20  $\mu$ m, which is comparable to the wavelengths of environmental IR radiation.

In contrast to the black patches, the blue-gray areas of *R. alpina* elytra are covered with transparent, prostrated hairs (Fig. 3(c)), while

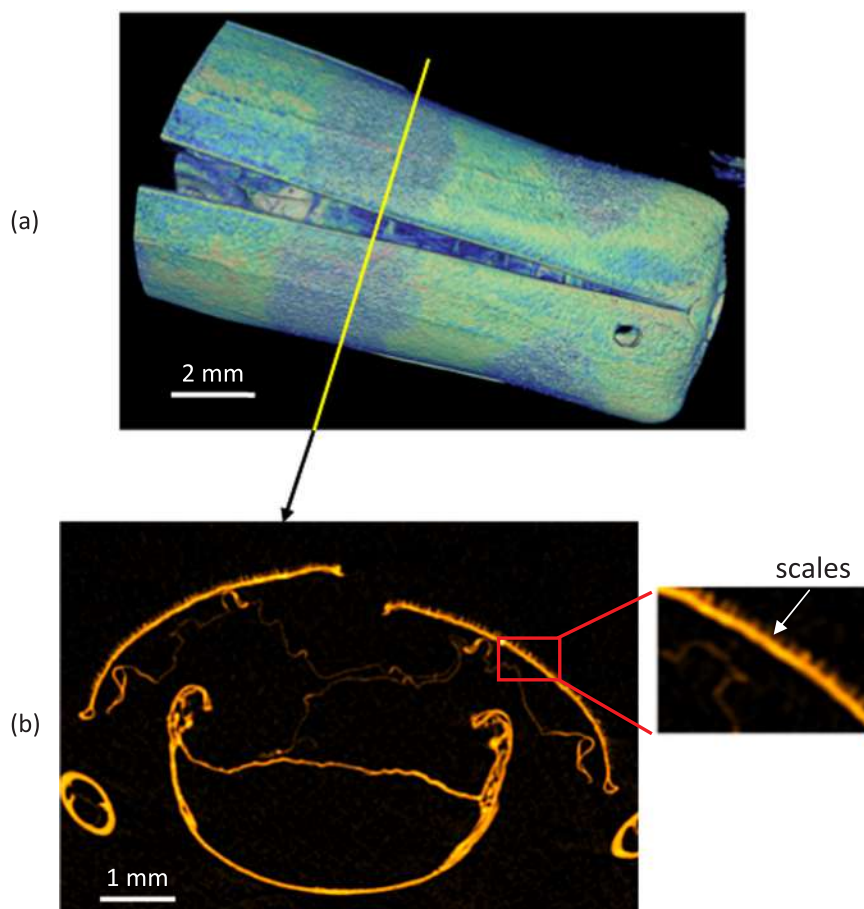


Fig. 2. (a) 3D reconstruction of *R. alpina* micro-CT image stack. (b) A single micro-CT slice through the black patch of *R. alpina* elytra (with scales visible on the enlarged portion of the slice).

the cuticle beneath is black and shiny. Together, the scales and cuticle present a velvety blue-gray appearance.

Grating-like structures are conspicuous features of the scales (Fig. 4), as observed at higher magnifications. A coarser grating (Fig. 4(a)), with a 1- $\mu\text{m}$  period, runs along the length of the scale. A much finer, irregular, sub-wavelength grating (with an approximately 100-nm period) extends diagonally between the coarse grating lines (Fig. 4(b)).

From the optical point of view, the structures on the gray and black areas of the elytra have completely opposite functions. The gray area is easily visible due to intense scattering (on the left in Fig. 5(a)), while the black area so strongly absorbs the light that only reflections from the polygonal impressions are partially visible (as revealed in optical microscope images in Fig. 5(a) and (b), at two magnifications). The scales themselves almost completely absorb the light and can be seen indirectly as dark shadows on the background, reflected from the cuticle beneath (Fig. 5(a)).

Individual scales are flattened (1–2  $\mu\text{m}$  thick, 20  $\mu\text{m}$  wide and 100  $\mu\text{m}$  long), asymmetrical and somewhat similar to butterfly-wing scales (Figs. 4(a) and 6(a)). They are strongly pigmented, with transmission gradually increasing from the blue to the red part of the spectrum, as can be verified by splitting the color image from Fig. 6(a) into its RGB components (see the three small images in Fig. 6(a)). The corresponding spectrum is shown in Fig. 6(b) and resembles that of melanin (Stavenga et al., 2012), a pigment frequently encountered in the cuticles of dark insects.

Reflectance of the black elytral patches was measured through an optical microscope by detecting the reflected intensity. A measured value was referenced to a white diffuse standard and corrected for

internal microscope objective scattering. We found that the reflectance in the blue and green parts of the spectrum is 2.6%, while in the red spectral range it is slightly higher, 3.5%.

The IR spectrum was between 2.5 and 15  $\mu\text{m}$  (using an FTIR spectrometer) and found to be completely in agreement with the one measured in (Herman et al., 2011), showing two strong transmission minima at approximately 3 and 6  $\mu\text{m}$  (Fig. 6(c)), corresponding to the atmospheric infrared windows (3–5  $\mu\text{m}$  and 8–14  $\mu\text{m}$ ).

### 3.2. Measurement and modeling of thermal properties of *R. alpina* elytra

Two thermal cameras (sensitive within 1.5–5.1  $\mu\text{m}$  and 7.5–13  $\mu\text{m}$  ranges and corresponding to atmospheric windows) were used to monitor dried insect specimens mounted on the substrate whose temperature was measured. A tape with emissivity of 0.95 was used as a reference. The insect dorsal surface appeared uniform in thermal equilibrium (see Fig. 7(a)), without any difference between the black spots and gray patches (both at 1.5–5.1  $\mu\text{m}$  and 7.5–13  $\mu\text{m}$  ranges). This is an interesting fact, showing that the gray and black areas contribute equally to the radiative energy exchange. However, there is a difference in emissivity between the two spectral ranges: average emissivity is 0.95 at 1.5–5.1  $\mu\text{m}$  (in line with (Stabentheiner and Schmaranzer, 1987)), and 0.85 at 7.5–13  $\mu\text{m}$ .

To simulate environmental conditions, we used a flashlamp to uniformly irradiate the insect body. Here we analyzed the heating and cooling of the insect body using a thermal camera at 7.5–13  $\mu\text{m}$  (measurements at 1.5–5.1  $\mu\text{m}$  have a similar character and will not be shown). As expected, the black areas efficiently absorbed the light and converted it to heat (Fig. 7(b)), followed by a quick temperature rise of

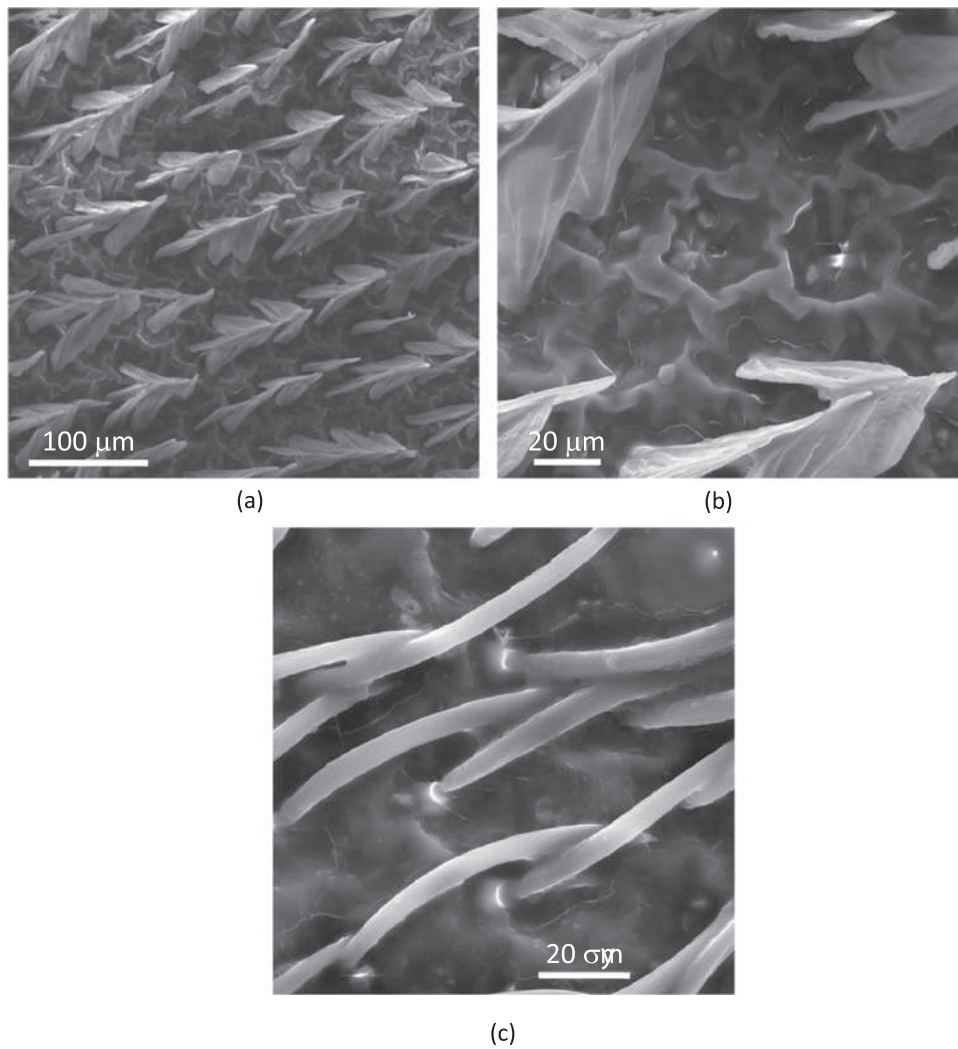


**Fig. 3.** FEGSEM images of *R. alpina*: (a) tent-like-organized scales concentrated in the black patch of elytra; (b) rugged elytral surface with polygonal depressions and dark scales; (c) hairs covering the blue-gray zone of elytra.

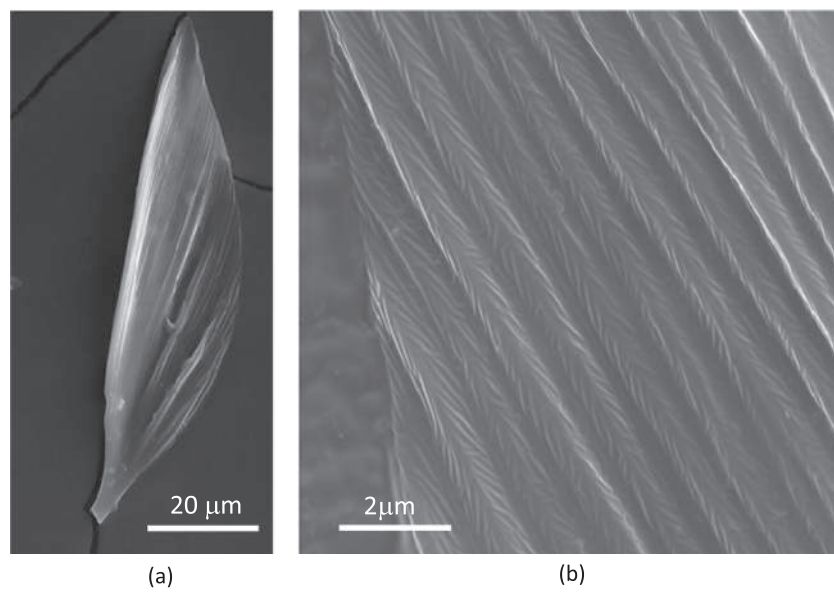


**Fig. 4.** (a) An individual scale of *R. alpina*, recorded on a FEGSEM. (b) 1-μm period grating-like structure and a herringbone shaped sub-wavelength grating, observable on the *R. alpina* scale at higher magnification.



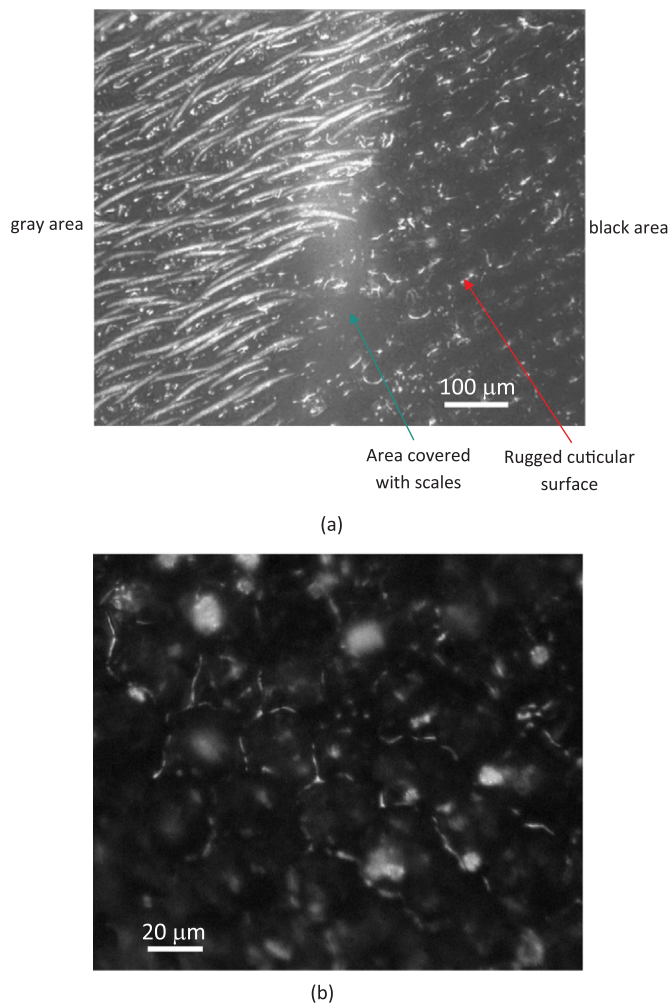


**Fig. 5.** (a) Optical reflection microscope image of a boundary between gray (on the left) and black (on the right) areas of *R. alpina* elytra. In the black area, the scales are just a dark shadow (shown by green arrow) on the rugged cuticular surface (red arrow); (b) black elytral area devoid of scales, showing irregular reflections from the edges of polygonal depressions (see Fig. 3(b)).

almost 7 °C, while the temperature rise was lower for the gray area (see the corresponding graph in Fig. 7(b) representing temperature diagrams). This proves that the black areas absorbed the visible light more efficiently.

To measure the thermal properties of black elytral patches, we illuminated them with a 405-nm laser beam with an energy density of 1.67 mJ/mm<sup>2</sup>. An IR image of the laser-heated insect is shown in Fig. 7(c). Even though low power was used, the black patches efficiently absorbed the radiation and the temperature increase was up to 20 °C (temperature variation is shown in a graph in Fig. 7(c)). The corresponding spatial variation of temperature was radially symmetrical (see the circular bright spot and the corresponding radial intensity distribution in Fig. 7(c)). Radial intensity distribution varied during irradiation and quickly reached a steady state (equilibrium) (Fig. 7(d)), without significant spreading of heat (which means that the thermal conductivity of elytra was small).

Further, we established a thermal model of *R. alpina* elytra to reveal the relative contribution of three basic thermal exchange mechanisms. This was done by fitting an experimentally recorded cooling curve to the theory based on radiation, convection and conduction (Levesque,

2014; Torres et al., 1993). The general, one-dimensional model includes all three mechanisms and is described by the following partial differential equation:

$$\frac{\partial T(z, t)}{\partial t} = -\frac{1}{\rho\tau c} [\varepsilon\sigma(T(z, t)^4 - T_0^4) + h(T(z, t) - T_0) + k\nabla_z T(z, t)] \quad (1)$$

where  $T$  and  $T_0$  are material and environmental temperature, respectively,  $z$  is the spatial coordinate,  $t$  is the time variable and  $\sigma$  is a Stefan-Boltzmann constant. Material is described by its thickness  $\tau$  and several constants: material density  $\rho$ , specific heat  $c$ , surface emissivity  $\varepsilon$ , coefficient of thermal conductivity  $k$  and convection coefficient  $h$ . This is a partial differential equation that would be quite complicated if the exact morphology of the elytra is taken as a boundary condition.

We simplified the model by assuming that the temperature across the elytra is uniform (due to its thinness) and the thermal conduction along the elytra is so small that it can be neglected (as shown in the previous section). The only mechanisms of heat dissipation taken into account were therefore radiation and heat loss through the surrounding air (conduction and convection). Spatial distribution was assumed to be constant along the  $z$ -axis, with the jump at the air-elytra interface. The equation is simplified to:

$$\frac{dT(t)}{dt} = -\frac{1}{\rho\tau c} \left[ \varepsilon\sigma(T(t)^4 - T_0^4) + h(T(t) - T_0) + \frac{k}{\tau}(T(t) - T_0) \right] \quad (2)$$

The last two terms describe heat dissipation at the elytra-air interface due to conduction and convection in air (proportional to the corresponding temperature difference). Due to the small thermal conductivity of the elytra (revealed experimentally and described in the previous section), we assumed that the heated layer of the elytra is an order of magnitude smaller than the physical thickness of the elytra, and this value was taken as a thickness  $\tau$  in a model. Table 1

Chitin and cuticular proteins are the dominant constituents of the elytra (Capinera, 2008; Gullan and Cranston, 2014). Our measurements are based on literature data on the physical properties of cuticle (Ishay and Pertsis, 2002; Vincent and Wegst, 2004) and chitin (Neville, 1975; Hammer et al., 2002).

Eq. (1) was solved numerically by the Runge-Kutta method and we were able to fit the experimental cooling curve within  $\pm 1.5$  K (see Fig. 8(a)). We numerically separated the contributions of three basic dissipation mechanisms to the total losses. It was found that radiative cooling is the most important mechanism, because in less than a second, heat loss by radiation reached more than 50% (see Fig. 8(b)).

Here and in the previous sections we describe the experimentally measured and theoretically calculated thermal response of *R. alpina*. In the next sections we will show the contribution of underlying micro- and nanostructures to the observed thermal effects. Analysis will proceed by, first, calculating the absorptive properties of elytral structures of *R. alpina* in the visible part of the spectrum and will be concluded by calculating the emissive properties of the elytra. This is important, because the insect's lifestyle is such that the elytra must efficiently dissipate the light energy absorbed primarily through the black patches in order to maintain body temperature within tolerable limits.

### 3.3. Absorption of visible light by elytral structures of *R. alpina*

We have constructed an optical model of black elytral patches, based on SEM images (Fig. 3(a) and (b)) of *R. alpina*. A 2D model (shown in Fig. 9) imitates the tent-like arrangement of cuticular scales, which optically function as an optical beam dump. From the point of view of geometrical optics, beams entering the input aperture (within

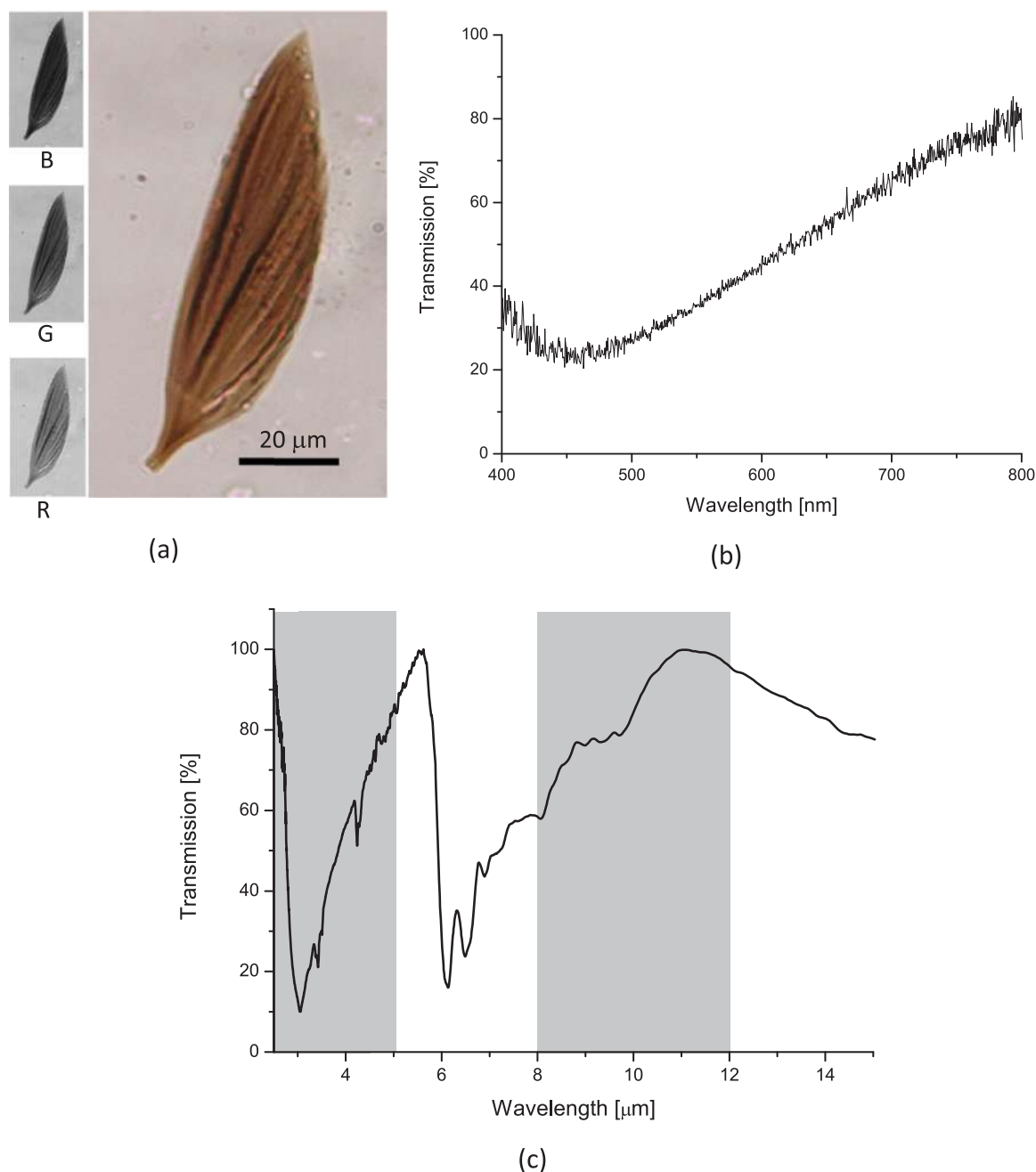


**Fig. 6.** (a) A single scale of *R. alpina* recorded in transmission (large image) and its RGB components shown on the left (three small images). Transmission gradually increases from blue to red channel. (b) Transmission spectrum of a single scale increases towards the red part of the spectrum (which is characteristic of melanin). (c) IR spectrum of a black patch of *R. alpina*. Gray areas show the sensitivity ranges of the IR cameras used in this research.

the 134° angular range, as estimated from SEM images; Figs. 3(a) and 4(a)) are being reflected several times from the wing scales, thus efficiently enhancing absorption. This is particularly true in the visible range, where the high concentration of melanin in the scales guarantees strong absorption.

To estimate the total absorption of the black patch, we must first calculate the absorption for a single reflection from a cuticular scale, which is a dominant elytral component of black patches. We noted that the scale surface was corrugated with high- and low-frequency gratings (Fig. 4(b)), above and below the wavelength of the visible light, respectively. At this point, we had to use wave optics to correctly model the interaction of light and the scale. Thus, small-scale morphology of the scale (Fig. 10(a)) is approximated by a two-dimensional elementary cell shown in Fig. 10(b). In the model, an elementary cell periodically

repeats itself along the  $x$ -axis, it is infinite along the  $z$ -axis and bounded by perfectly matched layers (PML) along the  $y$ -axis. The feature (A) in Fig. 10(b) approximates the ridges of a low-period (1 μm) grating, while two smaller structures (B) approximate the high-frequency grating, sitting atop a low-frequency one. This model is used in a FEM to calculate the local electromagnetic field and spectral variation of absorbance.

The physical parameters were as follows. The refractive index of chitin is 1.57 and the extinction coefficient was determined from FTIR measurements (see the corresponding spectrum in Fig. 6(c)) and found to vary from 0.008 to 0.001 (within a 8–14 μm range) and from 0.013 to 0.0016 (within a 3–5 μm range). The corresponding reflection spectra were calculated for a range of angles of incidence and averaged to simulate the diffuse environmental radiation in the beetle's habitat.

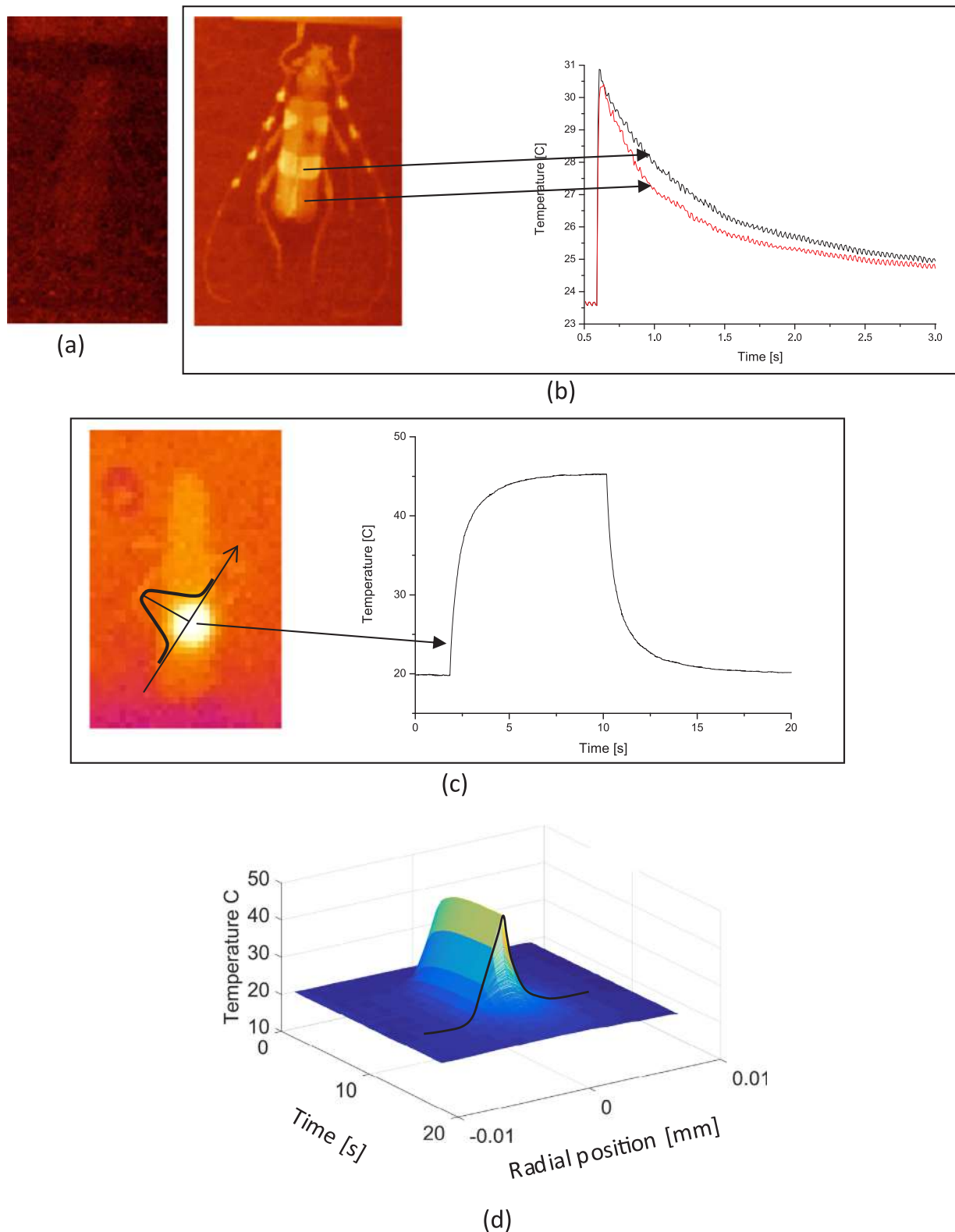


**Fig. 7.** (a) IR image of *R. alpina* in thermal equilibrium – black patches of elytra are not discernible. (b) IR image of *R. alpina* after irradiation with a flashlamp and the corresponding temperature variation of black (black diagram line) and gray (red diagram line) areas. (c) *R. alpina* heated by a laser beam (for 7.5 s) aimed at a black patch and the temperature variation at the center of the laser beam. (d) Temporal variation of radially symmetric temperature distribution of laser-heated *R. alpina* black patch. All images were recorded with a thermal camera sensitive within the range of 7.5–13  $\mu\text{m}$ .

Averaged absorption spectra after single and triple reflections are shown in Fig. 10(d). Three reflections were chosen as an average between a minimum of two and a maximum of four possible reflections (see rays in Fig. 9). Both spectra are compared to the reflection

spectrum of an unpatterned (flat-surface) scale, shown in the same graph. It is obvious that patterning doubles the amount of absorbed radiation. This is the consequence of the strong electromagnetic-field localization within the cuticular scale, as illustrated in Fig. 10(c). This



**Table 1**  
Parameter values used in a thermal model of *R. alpina*.

Parameters	Numerical value
conductivity of air, $k$	0.0257 W/m·K
convection coefficient of air, $h$	1.5 W/m <sup>2</sup> ·K (at 21 °C)
surface emissivity $\epsilon$	0.85
thickness $\tau$	$3.25 \times 10^{-6}$ m
density $\rho$ , [ 31, 30 ]	1.560 g/cm <sup>3</sup>
specific heat $c$ [32, 29]	1400 J/kg·K

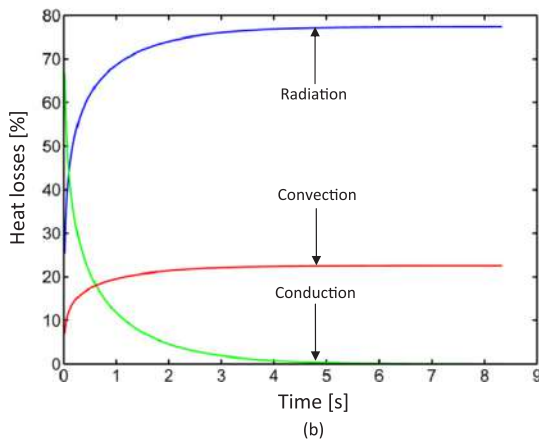
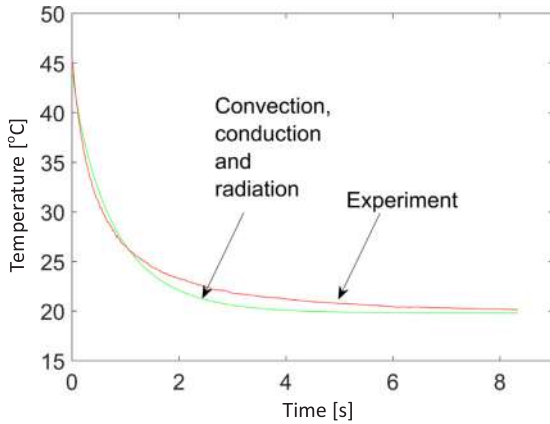


**Fig. 8.** (a) Experimentally recorded temperature decay (red curve) is approximated using a model that includes convective, conductive and radiative losses (green curve). (b) Contribution of radiative (blue curve), convective (red curve) and conductive (green curve) losses to the total heat dissipation.

makes this insect very efficient in capturing direct and diffused solar radiation and using it to heat its body.

Theoretical results are in agreement with the experiment showing 97.4% absorptance in the blue-green part of the spectrum. Discrepancy is greater in the red spectral range where theory predicts lower absorptance (80%) compared to the experiment (96.5%). This is certainly due to our inability to accurately model intricate cuticular structures – especially their randomness.

### 3.4. Emission of IR radiation by elytral structures of *R. alpina*

After modeling the absorptive properties of *R. alpina*, we analyzed the IR properties of the same structures. We measured emissivity across beetle elytra in the IR and found it identical for both gray and black areas (see Section 4). To better understand the IR properties of elytra, we constructed models of black patch and blue-gray areas. Absorptance

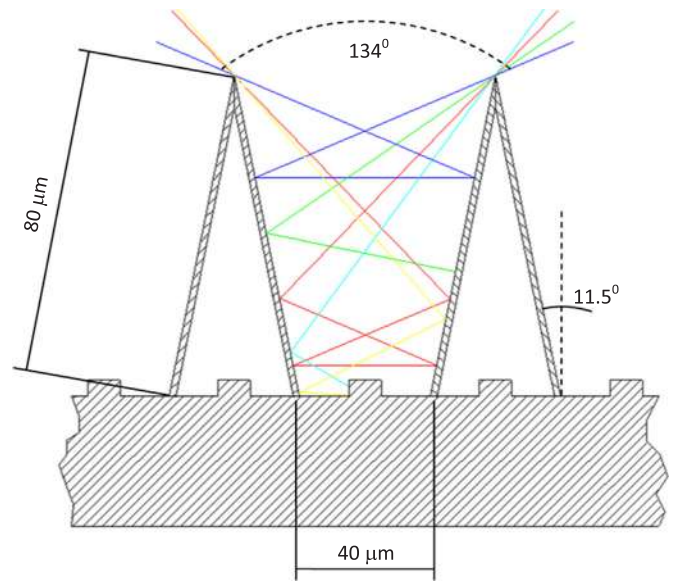


**Fig. 9.** An optical model of the *R. alpina* black patch operating as a beam dump in the visible part of the spectrum. Depending on the angle of incidence, beams (designated by different colors) may reflect 2–4 times.

was calculated using FEM, at the same time giving us the value of emissivity according to Kirchhoff's law.

We used a model of black patch shown in Fig. 11(a) that simulates scales (Fig. 3(a)), together with the underlying, corrugated cuticular structure (Fig. 3(b)). To determine the emissivity of this structure, it is enough to calculate the absorptance (which is equal to emissivity, according to the Kirchhoff's law). It was averaged within an angular range of IR collected by the thermal camera lens (determined by its F-number), thus simulating the experimental situation of recording an infrared image of the insect.

FEM analysis shows that the light is localized within the elytra or scales (Fig. 11(b)), depending on the wavelength and morphology of the elytra. This significantly amplifies innate absorption of chitin (see its transmission spectrum in Fig. 6(c)) due to increased optical path length within the structure. In order to establish the influence of scales, we also calculated the absorption of the elytra alone (without scales – modeled as in Fig. 11(c)). The corresponding graphs for elytra with and without scales, at 3–5 μm and 8–14 μm ranges, are shown in Fig. 11(d). Obviously, scales improve the absorptive/emissive characteristics of an insect by more than 20%.

The same line of reasoning was applied to the blue-gray elytral areas covered with hairs. Again, we found that the elytral hairs significantly improved the absorption and emissivity (Fig. 12(a) – (d)).

### 3.5. Radiative balance of *R. alpina*

Here we present a detailed energy balance, assuming the maximum insolation (1 kW/m<sup>2</sup>) of an insect. Total visible light energy absorbed by the elytra of *R. alpina* is equal to:

$$P_A = P_S (A_B S_B + A_G S_G) \tag{3}$$

where  $P_A$  is the total absorbed power,  $P_S$  is the solar constant,  $A_B$  is the absorption coefficient of the black patch,  $S_B$  is the total area of black patches,  $A_G$  is the absorption coefficient of blue-gray areas, while  $S_G$  is the total area of the blue-gray-colored surface. On the other hand, IR energy emitted by the whole elytra is:

$$P_E = 2\pi S_T \left[ \epsilon_M \int_M E(\lambda, T) d\lambda + \epsilon_F \int_F E(\lambda, T) d\lambda \right] \tag{4}$$

where  $P_E$  is total energy emitted by the elytra within two IR atmospheric windows,  $S_T$  is the total area of the cuticle ( $S_T = S_B + S_G$ ),  $\epsilon_M$  is the

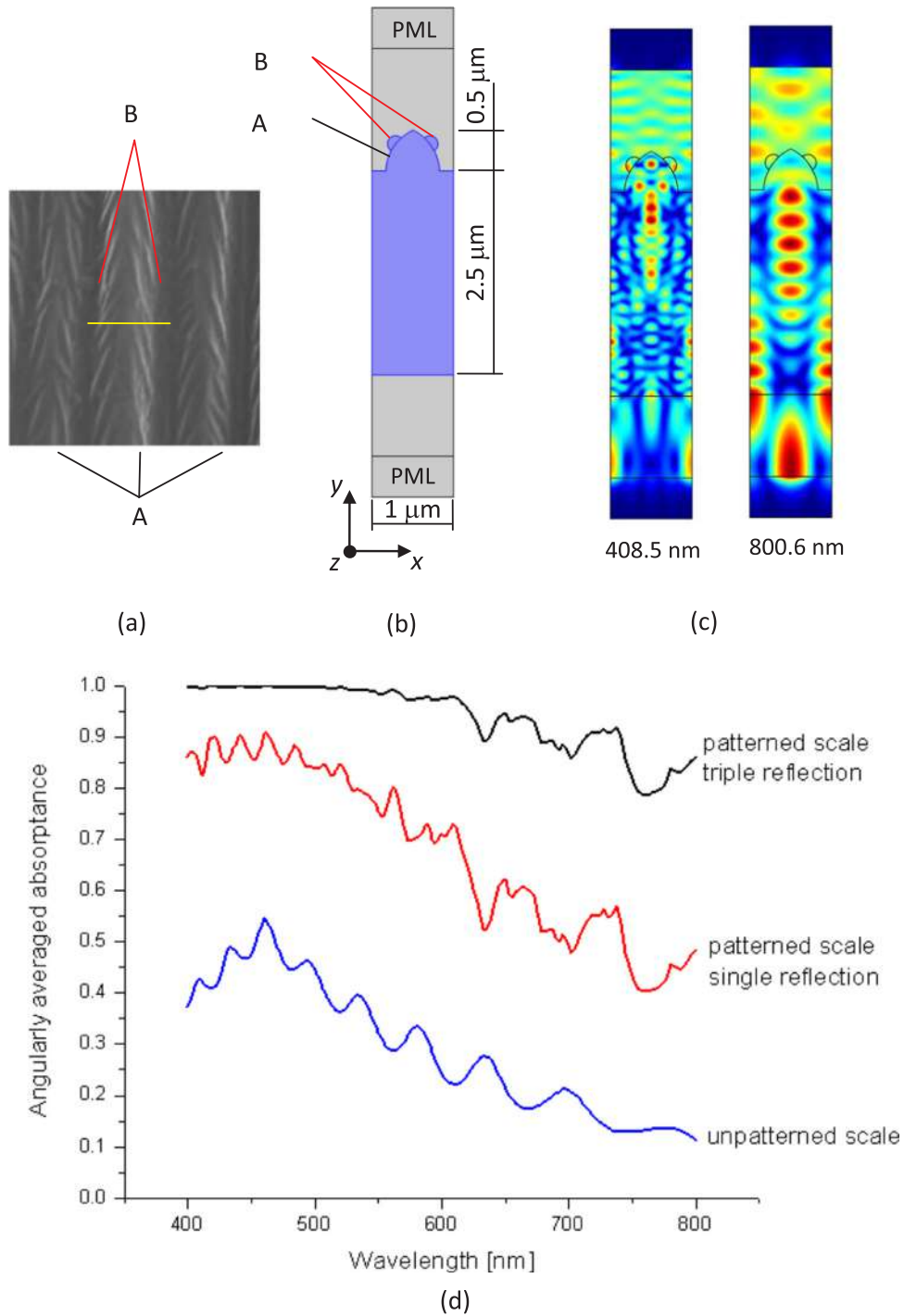


**Fig. 10.** (a) Characteristic pattern on the *R. alpina* scale. The letter A designates the low-period (approximately 1 μm) grating, and B designates the high-period, herringbone-shaped grating. The yellow line corresponds to one grating period, used to design (b), a model of *R. alpina* scales used in FEM calculations (PML – perfectly matching layer). (c) A field distribution at two wavelengths showing strong electromagnetic-field localization within the scale. (d) Increase of scale absorbance due to surface pattern.

emissivity within the mid-infrared atmospheric window ( $M = 3\text{--}5\ \mu\text{m}$ ),  $\epsilon_F$  is the emissivity within the far-infrared atmospheric window ( $F = 8\text{--}14\ \mu\text{m}$ ),  $\lambda$  and  $T$  are wavelength and absolute temperature, respectively, while  $E(\lambda, T)$  is the radiance of a black body.

As the next step, we found a temperature corresponding to the

balance of radiative gain in the visible and radiative losses in the infrared (i.e.  $P_A = P_E$ ). By Eqs. (3) and (4) we get:

$$P_S(A_B S_B + A_G S_G) = 2\pi S_T \left[ \epsilon_M \int_M E(\lambda, T) d\lambda + \epsilon_F \int_F E(\lambda, T) d\lambda \right] \quad (5)$$

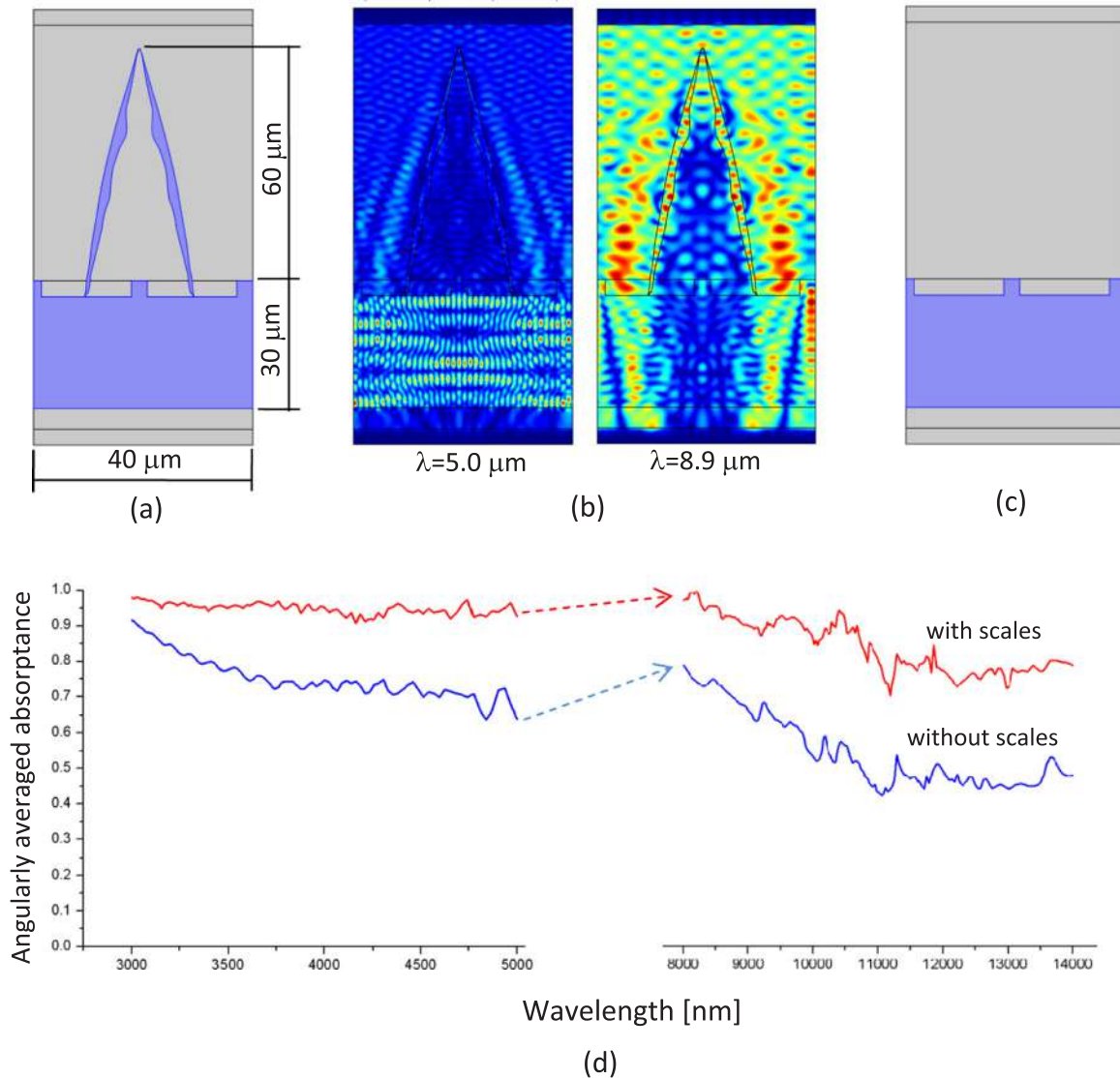


Fig. 11. IR properties of the *R. alpina* black patch. (a) A FEM model of a tent-like scale structure. (b) The corresponding EM field distribution at 5 μm and 8.9 μm. (c) A model of elytra without scales used to investigate the contribution of scales to total absorbance. (d) Angularly averaged absorbance of elytra with and without scales.

and, after a slight rearrangement:

$$P_3 \left( A_B \frac{S_B}{S_T} + A_G \frac{S_G}{S_T} \right) = 2\pi \left[ \varepsilon_M \int_M E(\lambda, T) d\lambda + \varepsilon_F \int_F E(\lambda, T) d\lambda \right] \quad (6)$$

We found that black patches occupy approximately one third of the whole elytral area ( $S_B/S_T=0.33$ ), while the rest of the elytra is gray ( $S_G/S_T=0.67$ ). Experimentally measured emissivities for the mid-infrared range and far-infrared were  $\varepsilon_M=0.95$  and  $\varepsilon_F=0.85$ , respectively, while the absorbance of the black patches was  $A_B=0.95$ , and that of the gray areas was  $A_G=0.12$ . We emphasize that the values of absorbance and emissivity are only averages and may vary across the insect elytra and between insect specimens.

Simple calculation, using Eq. (6), showed that the radiative balance between the visible and IR radiation was established somewhere between 300 K and 310 K, which is close to the maximum daily temperature in the summer months of the temperate areas where *R. alpina* lives (Anders et al., 2014). This result was obtained by assuming the normal angle of incidence of radiation with respect to the insect's elytra – which is the worst-case condition. However, the mutual position of the sun and the insect varies during the day, establishing the radiation balance at lower temperatures in an average situation.

#### 4. Discussion and conclusions

*R. alpina* is a saproxylic beetle present in Europe (except its northern parts), predominantly inhabiting thermophilic beech (*Fagus sylvatica*) forests (Duelli and Wermelinger, 2005), but it is also found on other broadleaved trees (Cizek et al., 2009). The peculiar, visually attractive coloration is explained by the insect's need to camouflage itself within its habitat (Starzyk, 2004). Nevertheless, an unavoidable question arises: why did nature create scales on the surface of the elytra? Why not just smooth, shiny black patches, without any cuticular appendages? Such black patches, without scales, would have the same camouflage role, without wasting life energy in producing a complicated nano-sized architecture on the elytral surface. The answer lies in the biology and ecology of the beetle and the optical properties of these surface nanostructures.

It was found that *R. alpina* adults search for decomposing beech wood on isolated trees and sun-exposed sites (Campanaro et al., 2017; Russo et al., 2011). The life cycle lasts about three years with the life span of an adult being just several weeks (Duelli and Wermelinger, 2005). Adults are the most active during the hottest months of the year (from July till August) and during the hottest part of the day (12–14 h) (Campanaro et al., 2017; Drag et al., 2011).



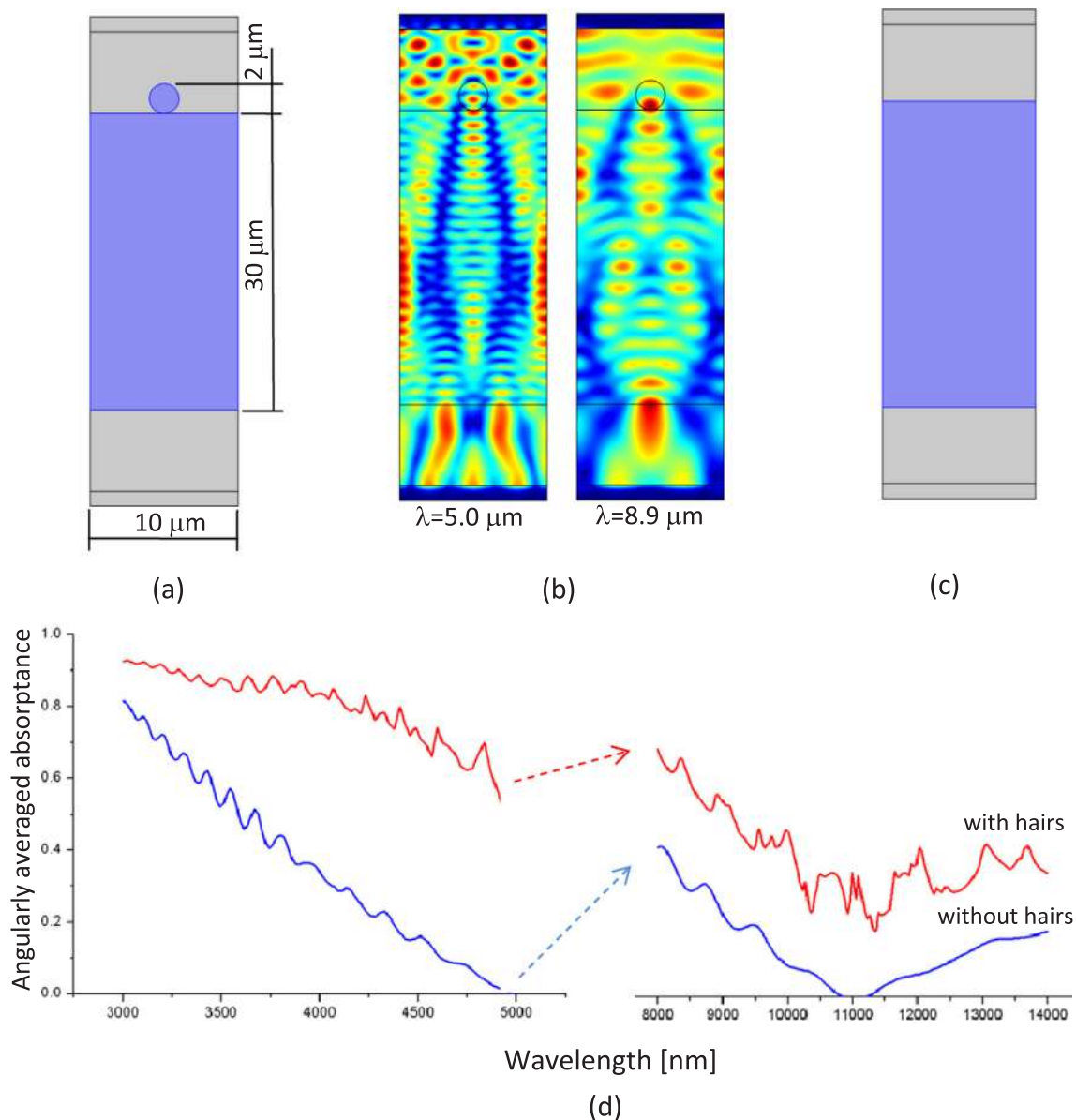


**Fig. 12.** IR properties of the blue-gray elytra of *R. alpina*. (a) A FEM model of the cuticle with hairs. (b) The corresponding EM field distribution at 5  $\mu\text{m}$  and 8.9  $\mu\text{m}$ . (c) A model of elytra without hairs used to investigate the contribution of hairs to total absorbance. (d) Angularly averaged absorbance of the elytra with and without hairs.

Despite the significance of this endangered species, little is known about its biology and ecology (Russo et al., 2011; Drag et al., 2011). Some conclusions about the biology of the species can be made by comparison with related species (Tsherepanov, 1981; Ray et al., 2009). The related *R. coelestis*, Semenov 1911, as well as many other Cerambycidae species, require no food as adults. This is supported by (Drag et al., 2011; Lachat et al., 2013) where no feeding was observed in *R. alpina* for 1500 adult capture events.

Adults are active and mobile, and they fly, but since they do not feed, their energy resources are very limited (Tsherepanov, 1981). This could be the reason why *R. alpina* is always found on sun-exposed trunks and branches. In order to fly, it needs energy, to warm up its thoracic muscles, which run up the hindwings (alae). Like butterflies (Kingsolver, 1985) and other ectotherms, the insect relies on an external heat source – solar radiation. This is in complete correlation with research (Duelli and Wermelinger, 2005; Russo et al., 2011) proving that insect-occupied trees were not randomly distributed: insects were only found in open forests, while unmanaged forests were avoided.

Only trees with a high sun index were selected. Occupied trees were always found in open sites with a low canopy closure and low or no undergrowth, allowing more sunlight to break through. Several other studies (Lindhe et al., 2005; Vodka et al., 2009; Buse et al., 2007) underline the importance of sun-exposed substrates for saproxylic beetles, which form a warm microclimate for the development of larvae.

Our research throws new light on the biology, ecology and evolution of *R. alpina*, proving that sun-exposed habitats are not just important for larvae development but also for the survival of adults. In order to maintain a temperature balance, heat gain and loss must be balanced. One of the possible mechanisms is regulation of heat exchange between the body and the external environment (behavioral mechanism). Here we show the significance of elytral setae (scales and hairs) of *R. alpina* for thermal regulation in adults. Direct solar radiation is efficiently absorbed by black patches, resulting in rapid heat gain. Additionally, excess heat is equally well dissipated by IR radiation through the whole surface of the elytra (both gray and black areas). Since *R. alpina* is a flying species, heat is produced during flight, but the

above mentioned mechanism also helps in establishing the temperature balance.

It seems that evolution needed to solve two problems. The first one was to provide an efficient camouflage for the insect on the bark of a beech, which required the emergence of black patches similar to blemishes on the tree bark. The second problem is a consequence of the first: the efficient dissipation of thermal energy absorbed through the black patches. The solution was found by making the black areas serve a dual purpose. In the visible part of the spectrum they function as an efficient beam dump, absorbing almost all the radiation. In the IR, structures interchange radiation with the environment and quickly attain equilibrium. The rest of the body efficiently scatters the visible light and produces a uniform grayish color, very similar to the base color of beech bark. Simultaneously, the IR properties of the black and gray areas are almost the same. In this way, energy absorbed through the black patches is efficiently dissipated throughout the entire body surface. These effects not only reduce the possibility of overheating if exposed to direct solar radiation, but also enable radiative heating if insolation is diminished. Thus, the insect is capable of establishing a thermal balance under conditions of the highest thermal load (direct sunlight exposure), as well as under diffuse light irradiation (reduced insolation, at the end of the day or in cloudy weather).

In this study, a thermal model of *R. alpina* was constructed based on experiments with dry specimens, which contain only 1% of water (according to (Lomakin et al., 2010)). However, the contribution of water to radiation effects is unimportant, because the absorption of water is insignificant within the atmospheric windows used by the insect to dissipate the excess heat. On the other hand, even if wet, the elytra are a thermal insulator and the contribution of conduction to overall thermal properties is small compared to that of radiation and convection (see Fig. 7(b)). Lipids and waxes are present as a superficial layer and are of no significance. Therefore, our results also apply to live insects.

It is possible that temperature affects the flow of the hemolymph and air through the tracheoles. However, in this particular insect, micro-CT has revealed the presence of quite compact elytra, meaning that the amount of fluids is minute and incapable of significantly influencing the thermal balance of *R. alpina*.

Absorption enhanced by surface texture was previously established in solar radiation collection research (Yablonoich and Cody, 1982; Niggemann et al., 2008). In this respect, it seems that nature was well ahead of man. From a practical point of view, such structures observed in *R. alpina* could be used for photovoltaic conversion of solar energy to dissipate the fraction of light energy converted to heat. In this way, solar cells will remain within the optimal thermal limits.

## Acknowledgments

We express our gratitude to the Serbian Ministry of Education, Science and Technological Development for the financial support through projects, Nos. ON171038, III45016, III47029, III45005, ON173027 and 173038. The authors are grateful to Dr. Ljubodrag Vujisić and Dr. Boban Anđelković from the Faculty of Chemistry, University of Belgrade, Serbia, who measured the FTIR spectrum of *R. alpina* elytra. We also thank Dr. Zlatko Prolić and Dr. Dejan Stojanović for their support and useful comments.

## Ethical approval

All necessary permissions to collect the samples of *R. alpina* were obtained from the Ministry of Environmental Protection of the Republic of Serbia and the Institute for Nature Conservation of Serbia.

## Author contributions

D.T. observed the structural nature of black patches of certain Cerambycidae. D.V.P. initiated the thermal analysis study. P.M.

performed the micro-CT analysis and V.L. performed the SEM analysis. B.S. calculated the optical and IR properties of the photonic structures, while G.D. made mathematical analyses of the thermal exchange mechanisms. Lj.T., D.P. and D.V. made the infrared measurements. D.P. and S.Ć. covered the biological, behavioral and environmental aspects of the work. D.V.P. supervised the research and performed the thermal balance calculations. D.P., D.V. and D.V.P. wrote the manuscript, taking into account the comments of the other coauthors.

This work was carried out as partial fulfillment of the requirements for the PhD degree of Danica Pavlović at the University of Belgrade –Faculty of Biology.

## Conflict of interest

The authors declare no conflict of interest.

## References

- Anders, I., Stagl, J., Auer, I., Pavlik, D., 2014. Climate change in central and eastern Europe. In: Managing protected areas in central and eastern Europe under climate change. Springer, Dordrecht, pp. 17–30.
- Angilletta Jr, M.J., Niewiarowski, P.H., Navas, C.A., 2002. The evolution of thermal physiology in ectotherms. *J. Therm. Biol.* 27, 249–268.
- Bense, U., 1995. Longhorn beetles: Illustrated key to the Cerambycidae an Vesperidae of Europe. Margraf Verlag.
- Biró, L.P., et al., 2003. Role of photonic-crystal-type structures in the thermal regulation of a Lycaenid butterfly sister species pair. *Phys. Rev. E* 67 (2), 021907.
- Buse, J., Schröder, B., Assmann, T., 2007. Modelling habitat and spatial distribution of an endangered longhorn beetle—a case study for saproxylic insect conservation. *Biol. Conserv.* 137 (3), 372–381.
- Campanaro, A., et al., 2017. Guidelines for the monitoring of *Rosalia alpina*. *Nat. Conserv.* 20, 165–203.
- Capinera, J.L., 2008. Encyclopedia of entomology. Springer, New York.
- Church, N.S., 1960. Heat Loss and the body temperatures of flying insects, II Heat conduction within the body and its loss by radiation and convection. *J. Exp. Biol.* 37, 186–212.
- Cizek, L., Schlaghamerský, J., Bořucký, J., Hauck, D., Helešič, J., 2009. Range expansion of an endangered beetle: alpine longhorn *Rosalia alpina* (Coleoptera: Cerambycidae) spreads to the lowlands of central Europe. *Entomol. Fenn.* 20 (3), 200–206.
- Dikić, G., Pavlović, D., Vasiljević, D., Tomić, Lj., Pantelić, D. (2016). The thermographic analysis of photonic characteristics of *Rosalia alpina* surfaces. Proceedings of 3rd International Conference on Electrical, Electronic and Computing Engineering IcETRAN 2016, Zlatibor, Serbia, June 13–16, 2016, ISBN 978-86-7466-618-0, pp. MOI1.2.1-5.
- Drag, L., Hauck, D., Pokluda, P., Zimmermann, K., Cizek, L., 2011. Demography and dispersal ability of a threatened saproxylic beetle: a mark-recapture study of the *Rosalia longicorn* (*Rosalia alpina*). *PLoS One* 6 (6), e21345.
- Duelli, P., Wermelinger, B., 2005. Der Alpenbock (*Rosalia alpina*). Ein seltener Bockkäfer als Flaggschiff art. *Merkbl. für die Prax.* 3 9, 1–8.
- Gallego, B., Verdú, J.R., Carrascal, L.M., Lobo, J.M., 2016. A protocol for analysing thermal stress in insects using infrared thermography. *J. Therm. Biol.* 56, 113–121.
- Gullan, P.J., Cranston, P.S., 2014. The insects: an outline of entomology. (John Wiley & Sons).
- Hammer, D.X., et al., 2002. Investigation of the transduction mechanism of infrared detection in *Melanophila acuminata*: photo-thermal-mechanical hypothesis. *Comp. Biochem. Physiol., Part A132*, 381–392.
- Heinrich, B., 1974. Thermoregulation in endothermic insects. *Science* 185 (4153), 747–756.
- Heinrich, B., 2013. The hot-blooded insects: strategies and mechanisms of thermoregulation. Springer Science & Business Media, New York.
- Herman, A., Vandenbem, C., Deparis, O., Simonis, P., Vigneron, J.P., 2011. Nanoarchitecture in the black wings of *Troides magellanus*: a natural case of absorption enhancement in photonic materials. In: Proceedings of SPIE Vol. 8094, Nanophotonic materials, 80940H-80941H.
- Ishay, J.S., Pertsis, V., 2002. The specific heat of the cuticle and the morphological differences between the brown and yellow cuticles of hornets. *J. Electron Microsc.* 51 (6), 401–411.
- Kingsolver, J.G., 1985. Butterfly thermoregulation: organismic. *J. Res. Lepid.* 24 (1), 1–20.
- Lachat, T., Ecker, K., Duelli, P., Wermelinger, B., 2013. Population trends of *Rosalia alpina* (L.) in Switzerland: a lasting turnaround? *J. Insect Conserv.* 17 (4), 653–662.
- Levesque, L., 2014. Law of cooling, heat conduction and Stefan-Boltzmann radiation laws fitted to experimental data for bones irradiated by CO<sub>2</sub> laser. *Biomed. Opt. Express* 5, 701–712.
- Lindhe, A., Lindelöw, Å., Åsenblad, N., 2005. Saproxylic beetles in standing dead wood density in relation to substrate sun-exposed and diameter. *Biodivers. Conserv.* 14 (12), 3033–3053.
- Lomakin, J., et al., 2010. Mechanical properties of the beetle elytron, a biological composite material. *Biomacromolecules* 12 (2), 321–335.
- Neville, A.C., 1975. Biology of arthropod cuticle. Springer Verlag, Berlin, Heidelberg.

- Niggemann, M., Riede, M., Gombert, A., Leo, K., 2008. Light trapping in organic solar cells. *Phys. Stat. Sol. (A)* 205, 2862–2874.
- Nijhout, H.F., 1991. *The development and evolution of butterfly wing patterns* (Smithsonian Institution Press, Washington-London).
- Preciado, A.J., 2002. et al., Radiative properties of polar bear hair. *ASME Proceedings of the International Mechanical Engineering Congress and Exposition*, pp. 57–58.
- Ray, A.M., et al., 2009. Male-produced aggregation pheromone of the cerambycid beetle *Rosalia funebris*. *J. Chem. Ecol.* 35 (1), 96–103.
- Russo, D., Cistrone, L., Garonna, A.P., 2011. Habitat selection by the highly endangered long-horned beetle *Rosalia alpina* in Southern Europe: a multiple spatial scale assessment. *J. Insect Conserv.* 15 (5), 685–693.
- Scoble, M.J., 1992. *The Lepidoptera. Form, function and diversity* (Oxford University Press, New York).
- Shi, N.N., et al., 2015. Keeping cool: enhanced optical reflection and radiative heat dissipation in Saharan silver ants. *Science* 349 (6245), 298–301.
- Stabentheiner, A., Schmaranzer, S., 1987. Thermographic determination of body temperatures in honey bees and hornets: calibration and applications. *Thermology* 2 (4), 563–572.
- Starzyk, J.R., 2004. in *Polska czerwona ksiega zwierzat. Bezkręgowce*. [Polish red data book of animals. Invertebrates.] (AR Poznan IOP. PAN, Kraków. pp. 148–149.
- Stavenga, D.G., Leertouwer, H.L., Hariyama, T., De Raedt, H.A., Wilts, B.D., 2012. Sexual dichromatism of the damselfly *Calopteryx japonica* caused by a melanin-chitin multilayer in the male wing veins. *PLoS One* 7 (11).
- The IUCN Red List of Threatened Species, Available at [www.iucnredlist.org](http://www.iucnredlist.org) (Version 2017-3).
- Torre-Bueno, J.R., 1976. Temperature regulation and heat dissipation during flight in birds. *J. Exp. Biol.* 65 (2), 471–482.
- Torres, J.H., Motamedi, M., Pearce, J.A., Welch, A.J., 1993. Experimental evaluation of mathematical models for predicting the thermal response of tissue to laser irradiation. *Appl. Opt.* 32, 597–606.
- Tsherepanov, A.I., 1981. *Longicorn beetles of North Asia (Cerambycinae)*. (Nauka, Novosibirsk).
- Twiss, S.D., et al., 2002. Behavioral evidences of thermal stress from overheating in UK breeding gray seals. *Mar. Mammal. Sci.* 18 (2), 455–468.
- Vincent, J.F., Wegst, U.G., 2004. Design and mechanical properties of insect cuticle (187-development199). *Arthropod Struct. Dev.* 33 (3) (187-development199).
- Vodka, S., Konvicka, M., Cizek, L., 2009. Habitat preferences of oak-feeding xylophagous beetles in a temperate woodland: implications for forest history and management. *J. Insect Conserv.* 13, 553–562.
- Vukusic, P., Sambles, J.R., 2003. Photonic structures in biology. *Nature* 424 (6950), 852.
- Vukusic, P., Sambles, J.R., Lawrence, C.R., Wootton, R.J., 2001. Structural colour: now you see it—now you don't. *Nature* 410 (6824), 36.
- Vukusic, P., Sambles, J.R., Lawrence, C.R., 2004. Structurally assisted blackness in butterfly scales. *Proc. R. Soc. Lond. B: Biol. Sci.* 271 (Suppl 4), S237–S239.
- Yablonovich, E., Cody, G.D., 1982. Intensity enhancement in textured optical sheets for solar cells. *IEEE Trans. Electron Devices* 29, 300–305.





Cite this: *Soft Matter*, 2018, 14, 5595

# Golden moth-inspired structures with a synergistic effect of interference, absorption and scattering

Svetlana Savić-Šević,<sup>a</sup> Dejan Pantelić,<sup>a</sup> Branislav Jelenković,<sup>a</sup> Branislav Salatić<sup>a</sup> and Dejan V. Stojanović<sup>b</sup>

We describe a new type of photonic material inspired by a *Diachrysia chrysitis* moth, whose nano-structured wings exhibit a prominent golden color. This is a layered photonic structure with a large refractive index contrast, whose alternating layers are rough at the nanoscale level. Theoretical analysis shows that the scattering and interference interact to enhance the local field within the layers and increase the absorption of the material, particularly in the UV–blue part of the spectrum. Theory is experimentally verified using holographically manufactured Bragg gratings in the dichromated-pullulan (DCP). Alternating air-pullulan layers are produced and held in place by sparsely separated nano-pillars. Air voids are filled with 20–100 nm diameter spherical nanoparticles which act as scatterers. Such materials, with a high refractive index contrast and nano-scale scatterers, are important for achieving large reflectance and a broad spectrum, with scattering as an additional mechanism for spectral control.

Received 2nd April 2018,  
Accepted 1st June 2018

DOI: 10.1039/c8sm00683k

[rsc.li/soft-matter-journal](http://rsc.li/soft-matter-journal)

## Introduction

Natural nanotechnology still surpasses the technological achievements of our civilization. This is most evident, even visible by the naked eye, in the world of insects whose structural colors constantly amaze keen observers. The shiny blue colors of *Morpho* butterflies,<sup>1</sup> the violet tints of *Apatura iris* (Linnaeus, 1758) and *Apatura ilia* (Denis & Schiffermüller, 1775) butterflies,<sup>2</sup> the green colors of beetles (*Coleoptera*),<sup>3</sup> or the yellow-greens of certain bugs (Hemiptera),<sup>4</sup> are marvels of natural nanotechnology. They are produced quickly, effortlessly and in huge amounts, during the short lifecycle of insects.

Structural colors in nature mostly have a spectral distribution within a rather limited wavelength range and produce well defined colors – typically blues and greens. In spite of that, certain insects reflect light in a wide spectral range, resulting in silvery,<sup>5</sup> gold<sup>5</sup> or bronze<sup>6</sup> colors. Such broad spectral distributions are usually caused by chirped Bragg gratings, but color mixing<sup>7</sup> or local spectra averaging<sup>8</sup> can be found in certain insect species.

The richness of insect structures provides a constant inspiration for researchers to look for new ways of imitating natural optics and photonics structures.<sup>9,10</sup> There are quite a number of techniques used for biomimetics of photonic structures and a

good overview is given in the paper of Butt *et al.*<sup>11</sup> Certain techniques are complex, slow and expensive, such as the one using focused Ga<sup>+</sup> ion beam chemical vapor deposition to manufacture free-standing butterfly-type structures with 80 nm resolution.<sup>12</sup> Other methods are simpler and use natural structures as templates for directly copying into other materials, such as TiO<sub>2</sub>.<sup>13</sup> That is why industrial-scale production methods of simple biomimetic surfaces were developed, such as layer-by-layer spraying.<sup>14</sup>

Holography and interference methods stand out for their capability to generate complex, large-area photonic structures cheaply and efficiently.<sup>15</sup> Several laser beams interfere in a suitable photo-sensitive material: polymer dispersed liquid crystals,<sup>16</sup> photoresists,<sup>17</sup> dichromated gelatin<sup>18</sup> or silver-halide emulsions.<sup>19</sup> After chemical processing, nanostructures are generated, whose minimum dimension is limited by the wavelength of light. This method was used to create *Morpho*-butterfly-like structures on a photoresist.<sup>20</sup>

We were inspired by the Burnished brass moth, *Diachrysia chrysitis* (Linnaeus, 1758), whose wing scales and membranes represent a layered structure with rough surfaces. Here we see that several optical effects – interference, scattering and absorption<sup>8</sup> – cooperate to produce the golden wing color. Other insects<sup>7,10</sup> or their fossilized remnants<sup>21</sup> were found with a similar type of structure, resulting in the same, rather broad, reflection spectra.

In this paper we propose a new class of photonic materials characterized by layers with irregular, rough surfaces, residual absorption and high refractive index contrast. From the theoretical

<sup>a</sup> Institute of Physics, University of Belgrade, Pregrevica 118, 11080 Zemun, Serbia.  
E-mail: [savic@ipb.ac.rs](mailto:savic@ipb.ac.rs)

<sup>b</sup> Institute of Lowland Forestry and Environment, University of Novi Sad, Antona Čehova 13, 21000 Novi Sad, Serbia

point of view, such structures exhibit a useful interplay between scattering, local field enhancement, planar waveguiding and interference. As a result, radiation is reflected in a broad spectral range. We use a transfer matrix method<sup>22</sup> and surface scattering theory<sup>23</sup> with associated intensity enhancement<sup>24</sup> to theoretically explain the observed optical properties.

As a proof of concept, we used holography (interference lithography) to pattern a pullulan – a linear homo-polysaccharide produced by the yeast-like fungus *Aureobasidium pullulans*. Pullulan was photo-sensitized by doping with chromium ions – we named the resulting material dichromated pullulan (DCP).<sup>25</sup> After exposure and simple chemical processing, the material exhibited just what we needed: a number of pullulan layers densely covered with randomly dispersed nano-spheres. The layers are separated by nano-scale pillars and the space between them is void. The resulting spectrum is wide and closely resembles the spectra of metallic gold and *D. chrysitis* moth wings.

### Properties of the *Diachrysia chrysitis* moth wing and its holographically generated analogue

*D. chrysitis* is an attractive insect with large, golden-color patches covering its fore wings (Fig. 1a). The wings are covered with scales which are almost transparent if observed individually. However, in their natural position on the wing (Fig. 1b), wing membranes, ground and cover scales act together to produce the resulting color.<sup>8</sup> The spectrum is wide and visually closely corresponds to the color of gold.

From the morphological point of view, the wings have the standard structure of the vast majority of Lepidopterans

(Fig. 1c), with two wing membranes (approximately 1  $\mu\text{m}$  thick) covered ventrally and dorsally with two layers of scales (cover and ground). There are actually six distinct layers because each scale has two, air-spaced, laminae (air layers and laminae are 100 nm thick, each). The ventral side of the wing is not of much interest here, because wing-scales are pigmented, strongly attenuate the radiation and are incapable of reflecting a significant amount of light. All layers are structured: wing membranes have a number of hemispherical protuberances, the external surfaces of scales' upper laminae have a regular grating structure (Fig. 2a), while their internal surfaces are rough (Fig. 2b and c).

In order to imitate the optical characteristics of *D. chrysitis*, it is necessary to manufacture the layered structure having rough surfaces. We did that by holographically generating Bragg grating inside the dichromated pullulan – a homemade material produced by sensitization of pullulan with ammonium dichromate.

Diffraction gratings with spherical inclusions are fabricated by combination of the holographic method (top-down technique) and non-solvent-induced phase separation (bottom-up method).<sup>26–28</sup> The whole process involves several steps:

- (1) preparation of a DCP film on a glass plate,
- (2) film exposure using a laser,
- (3) chemical development,
- (4) desiccation in a non-solvent bath at room temperature, and
- (5) drying in a closed vessel.

In the first step, the DCP is prepared by mixing 8% aqueous solution of pullulan (purchased from Sigma-Aldrich) and 45% of ammonium dichromate (by weight of pullulan). The solution

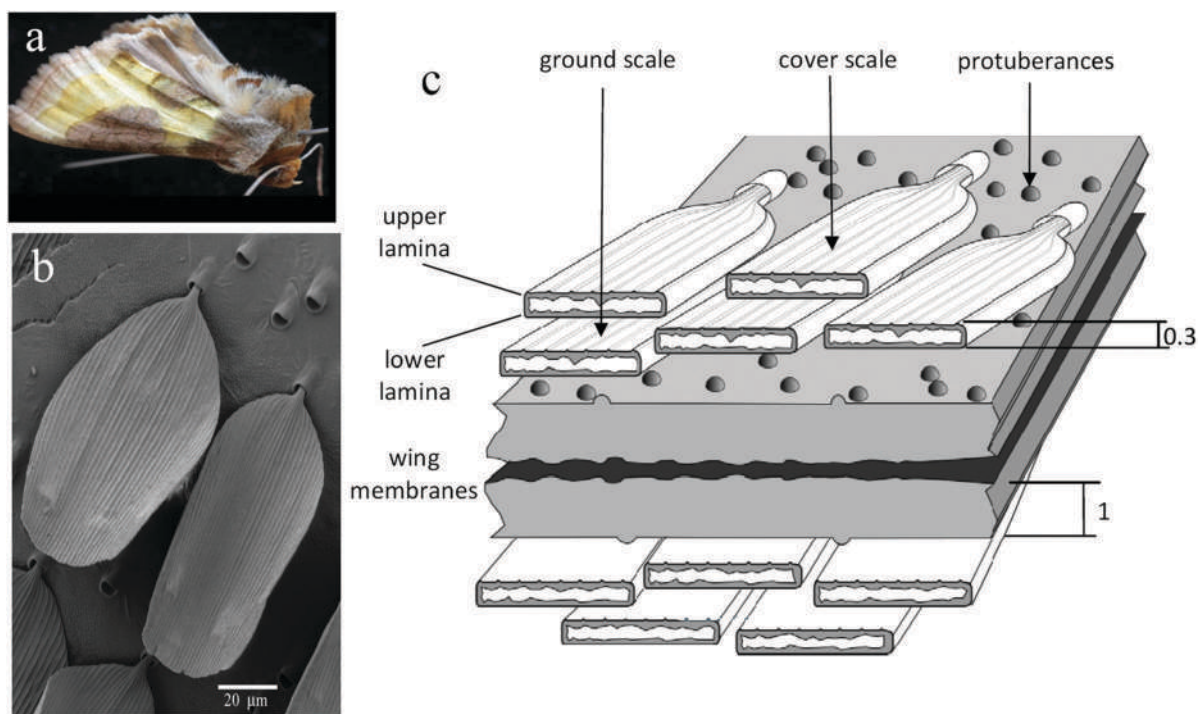


Fig. 1 (a) *Diachrysia chrysitis* moth. (b) Wing scales on the wing membrane of *D. chrysitis* moth, observed under a scanning electron microscope. (c) A scheme of the *D. chrysitis* wing's. The whole structure is cross-sectioned to display rough internal surfaces of wing scales. Dimensions are in  $\mu\text{m}$ .

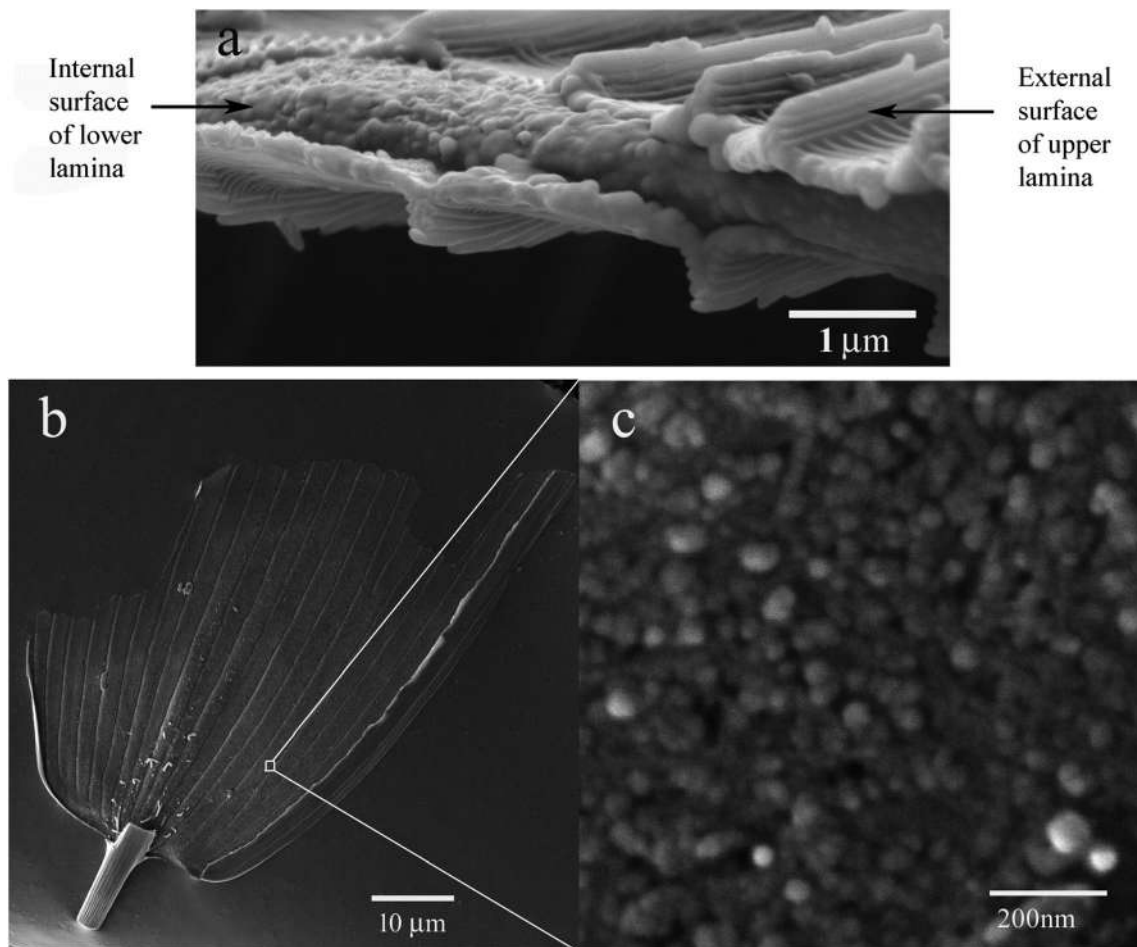


Fig. 2 (a) A broken and folded *D. chrysitis* scale revealing simultaneously the external grating-like structure and internal random structure. (b) Wing scale of *D. chrysitis* with intentionally removed lower lamina. (c) Enlarged portion of the image in (b) showing the rough internal surface in more detail.

was coated onto a clean glass slide in a horizontal position and the film was dried overnight under normal laboratory conditions. The resulting DCP film is 10 μm thick, yellowish, transparent and photosensitive.

The dried film is exposed at normal incidence using a single longitudinal mode, diode-pumped Nd-YAG laser, at 532 nm. After propagation through the film, the laser beam is back-reflected from a mirror behind the DCP plate. Two counter-propagating beams interfere to create a standing wave pattern consisting of parallel planes with spacing equal to  $\lambda/2n$  ( $\lambda$  is the wavelength of the laser and  $n$  is the refractive index, which is 1.45 for pullulan<sup>29</sup>).

The DCP plate was further chemically processed using a mixture of water and isopropyl alcohol (ratio 3 : 1 respectively). Treatment lasted for two minutes, followed by pure isopropyl-alcohol dehydration. Finally, the material is fully dried in a closed vessel.

The morphology of the resulting DCP grating was investigated using a high resolution field emission gun scanning electron microscope (FEGSEM). A number of DCP layers with a spacing of about 135 nm and a similar thickness are visible.

The space between them is void and they are supported and separated by tiny pillars (Fig. 3a and b). The layers are covered with nano-sized spherical particles distributed according to the Weibull distribution<sup>30</sup> (Fig. 3c), which exhibits maximum at 45 nm and mean at 55 nm (maximum and mean are different due to the asymmetry of the distribution).

There is a complex mechanism leading to the generation of structures in the DCP, which is based on pullulan's solubility in water and insolubility in isopropyl alcohol. During exposure, hexavalent chromium ion  $\text{Cr}^{6+}$  is photo-reduced to trivalent  $\text{Cr}^{3+}$ , which covalently cross-links with pullulan molecules in exposed areas. Cross-linking hardens the pullulan making it insoluble in water. This causes a solubility difference between exposed and unexposed regions.

After exposure, the DCP grating is chemically processed using a mixture of water and isopropyl alcohol as a developer. The unexposed regions (areas of destructive interference) are chemically unaffected and are dissolved in the developer. In contrast, areas of constructive interference are not dissolved during development, as a consequence of hardening by cross-linking. As a result, solid DCP layers are produced. At this stage,



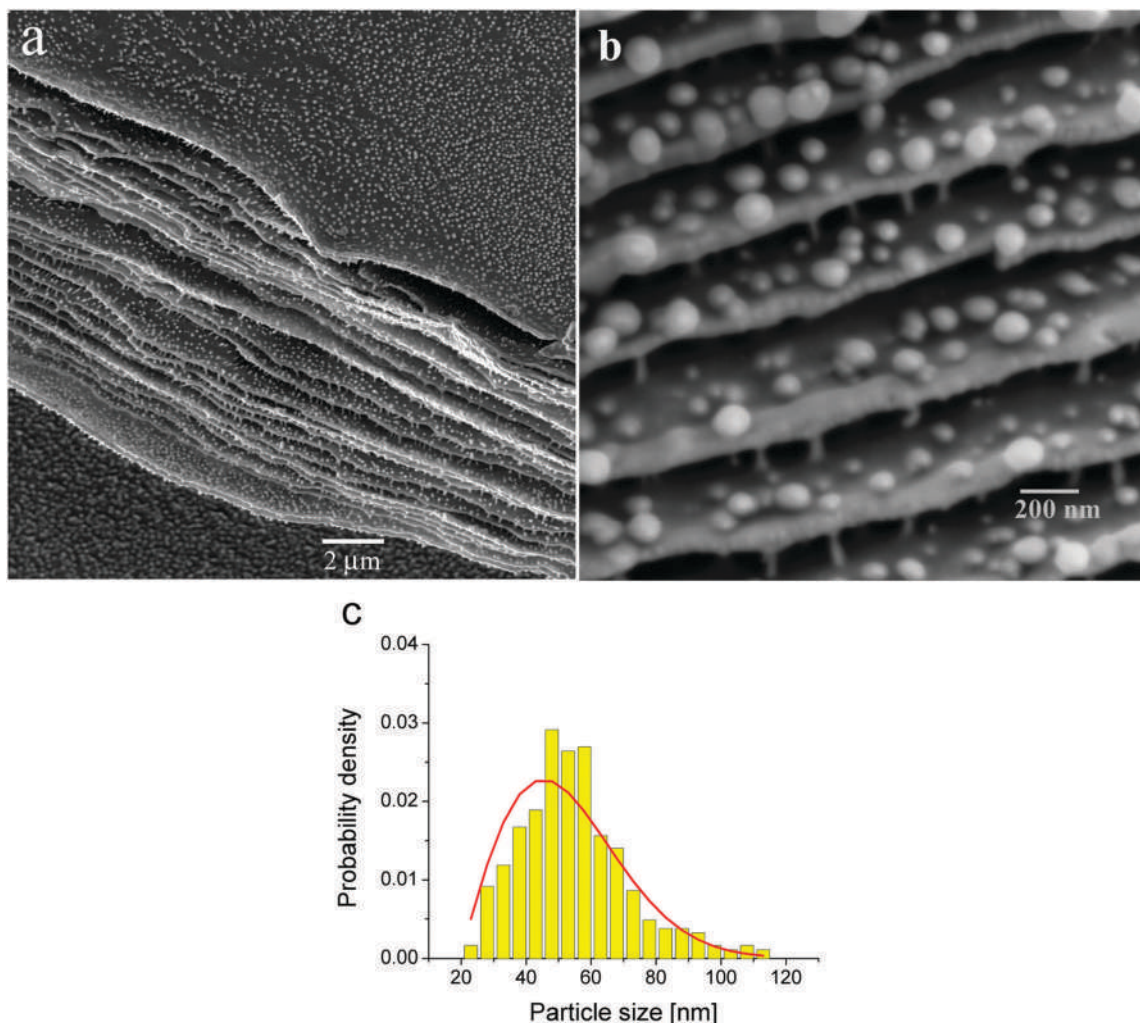


**Fig. 3** (a) FEGSEM image of a cross-section of the DCP grating. Particle density is  $58 \pm 12$  particles  $\mu\text{m}^{-2}$ . (b) Enlarged portion of a DCP grating with nano-spheres of average size  $55 \pm 17$  nm. (c) Size distribution of nanospheres between DCP layers (yellow bar chart) and the corresponding Weibull distribution (red line). Distribution maximum is at 45 nm and its mean is at 55 nm.

the developer with dissolved pullulan remains trapped between solid layers. The processing is finished by immersing the DCP in pure isopropyl alcohol, which removes water and forces dissolved pullulan to aggregate into nanoparticles (as a result of non-solvent phase separation).

Fig. 4a shows the DCP sample displaying a golden color. On the microscopic level, color variation is detected (see differently colored dots in Fig. 4b), which means that the macroscopically observed color results from local spectra mixing. Transmission and reflection spectra, Fig. 4c and d, respectively, were measured using a spectrometer (Ocean Optics) attached to an optical microscope. The reflection spectrum of DCP is quite similar to that of *D. chrysitis*.<sup>8</sup> Both spectra are broad with a cut-off wavelength of approximately 500 nm, visually corresponding to a golden color. However, the maximum reflectance  $R$  of DCP is significantly higher ( $R \approx 0.6$ ), compared to *D. chrysitis* ( $R \approx 0.4$ ). This is due to the much larger number of layers in the DCP (40) vs. only 6 in *D. chrysitis*. In both cases,

the reflectance is enhanced by the high refractive index contrast between air and material.

### Theoretical analysis of the optical properties

Here we present a theoretical analysis of photonic structures characterized by regularly spaced layers with irregular surfaces and a large refractive index contrast. We treat structures as Bragg gratings, schematically shown in Fig. 5a, with scattering and internal field enhancement effects taken into account.

We first demonstrate that the scattering on the internal grating surfaces leads to significant dispersal of incident light. The wavelength of the incident visible light (inside material) is much larger than the scatterers and, widely used, scalar surface-scattering theory<sup>23,31</sup> is applicable to determine the amount of scattered radiation.

Under these circumstances, the incident light is split into two parts: one, regular, propagating as if the surface is perfectly flat, and the other diffusely scattered (haze), see Fig. 5b.

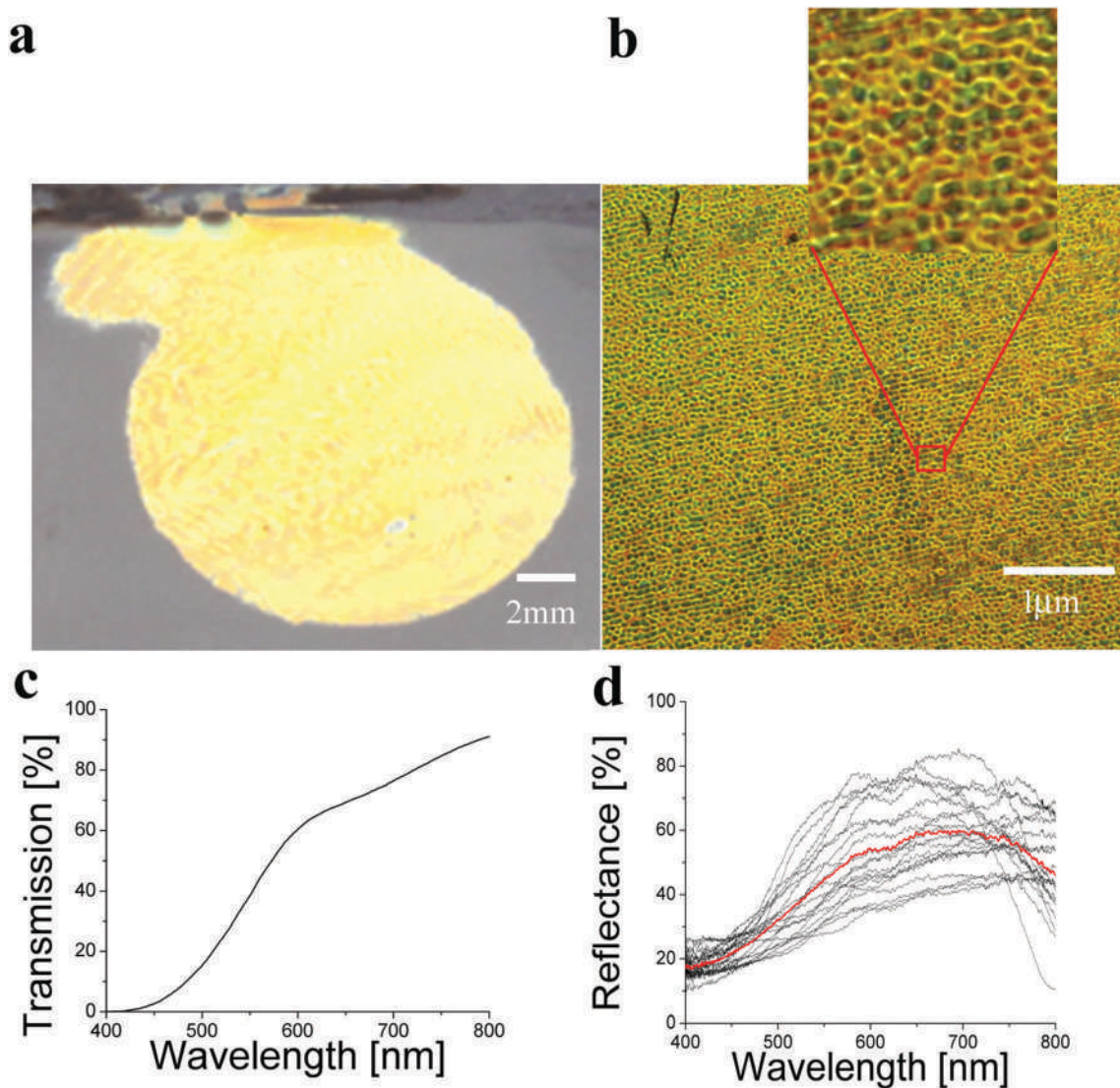


Fig. 4 (a) Golden appearance of the DCP layer. (b) Reflection from the DCP layer recorded under the reflection microscope. (c) Transmission spectrum of unexposed, chemically unprocessed dichromated pullulan, showing the strong absorption in the blue–green part of the spectrum. This spectrum is quite uniform across the sample. (d) Experimentally recorded reflection spectra of the DCP grating recorded at several positions. Individual, local, spectra (black curves) were recorded under the optical microscope and averaged (red curve).

Regularly propagating light obeys classical Fresnel reflection/transmission laws and “sees” the material as a volume Bragg grating. The haze and the regular component are described relative to transmittance  $T_0$  and reflectance  $R_0 = 1 - T_0$  of an ideally flat surface (assuming that the Fresnel equations hold). Accordingly, the haze transmittance  $T_H(\lambda)$  and reflectance  $R_H(\lambda)$  of a rough surface are described by:<sup>2,3</sup>

$$T_H(\lambda) = T_0 \left[ 1 - \exp \left( - \left[ \frac{2\pi\sigma}{\lambda} (n_i \cos \phi_i - n_t \cos \phi_t) \right]^2 \right) \right] \quad (1)$$

$$R_H(\lambda) = R_0 \left[ 1 - \exp \left( - \left[ \frac{4\pi\sigma}{\lambda} n_i \cos \phi_i \right]^2 \right) \right] \quad (2)$$

where  $T_0$  and  $R_0$  are the transmittance and the reflectance of a perfectly flat surface, respectively,  $\lambda$  is the wavelength of light

under vacuum,  $\phi_i$  and  $\phi_t$  are the angles of incidence and refraction,  $n_i$  and  $n_t$  are the corresponding refractive indices, while  $\sigma$  is the root mean square (RMS) roughness of the surface.

We have computed the intensity of scattering for materials within the RMS range of several tens of nano-meters, and shown them in Fig. 6a and b. The intensity of transmitted haze does not depend on whether it comes from a high or low refractive index medium, Fig. 6a. In contrast, the intensity of reflected haze depends on the side from which the radiation comes, Fig. 6b. By comparing Fig. 6a and b, it is obvious that the scattering is 4–5 times stronger in transmission, compared to reflection. For both reflected and transmitted radiation, haze is much stronger at shorter wavelengths (as in Rayleigh scattering). As can be seen in Fig. 6 the intensity of scattering is much higher inside the blue–UV spectral range.

On the other hand, scattered radiation excites planar waveguide modes of Bragg layers. It was verified by the finite element

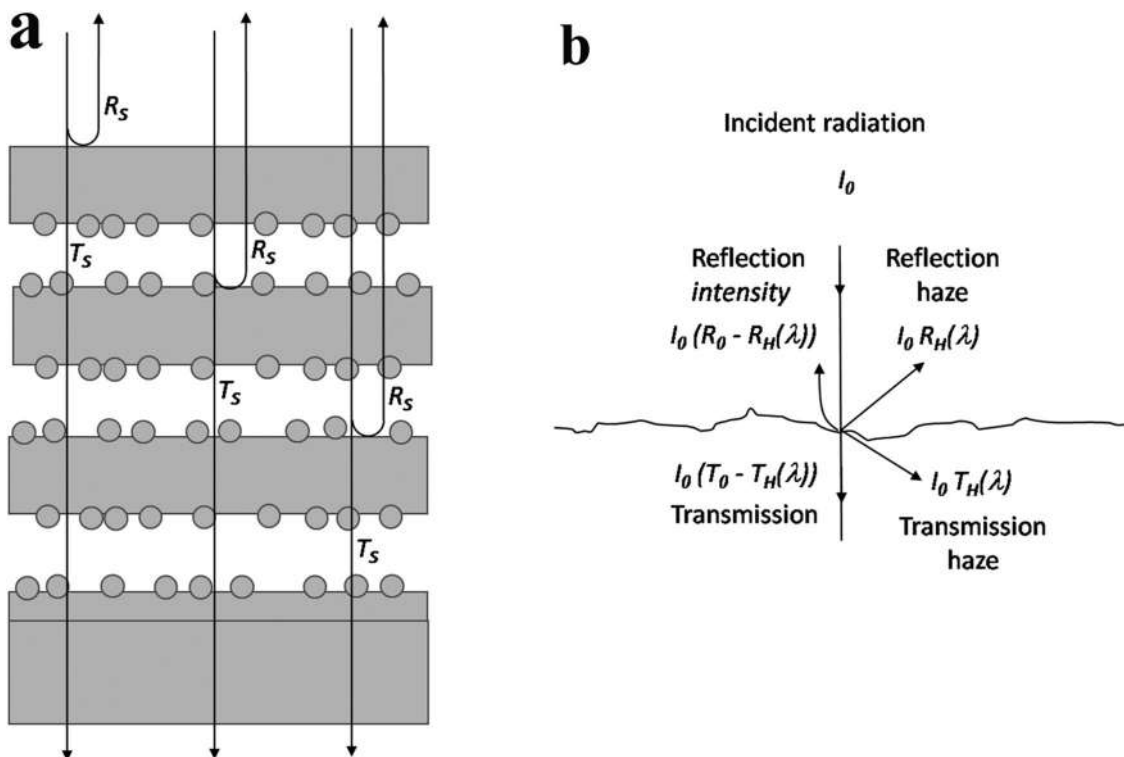


Fig. 5 (a) Scheme of a DCP diffraction grating with nano-sized particles.  $R_s$  and  $T_s$  are specular reflection and transmission coefficients, corrected for scattering effects. (b) Incident radiation is divided into specular and haze components.

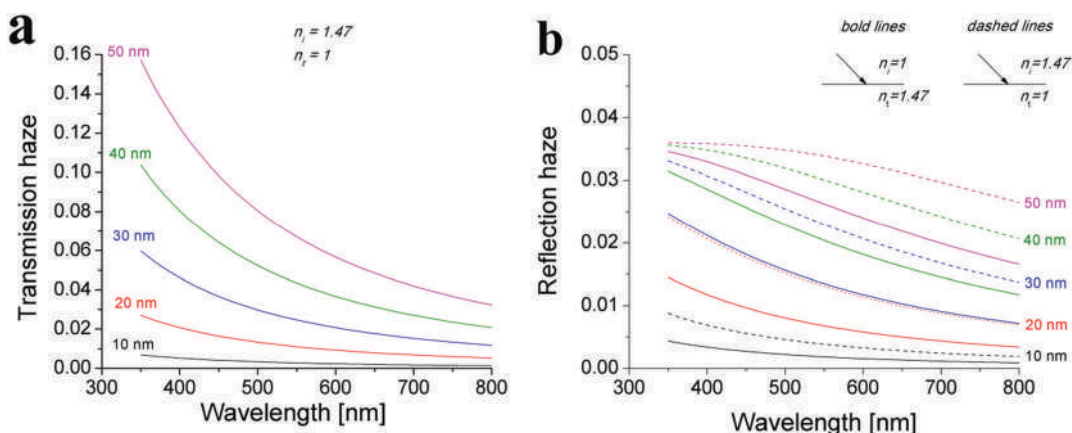


Fig. 6 Spectral dependence of haze from an interface with RMS roughness (ranging from 10 nm to 50 nm) as a parameter: (a) transmission and (b) reflection (in this case haze depends on whether light comes from the high index (dashed curves) or low index material (bold lines)). Haze was calculated for a single surface between air and pullulan.

method (FEM) applied to the DCP structure with a layer thickness of 135 nm, an air space of 130 nm and a refractive index of 1.45. The roughness was simulated using nanoparticles of 55 nm diameter (see Fig. 7a). Periodic boundary conditions were used in a simulation, and perfectly matching layers were positioned above and below the grating. Fig. 7b shows excited planar modes at the resonant wavelength, under the assumption that there is no absorption. It is interesting to note that by redistributing the spheres, the overall modal structure remains almost the same, with a possible slight shift

of the wavelength of planar modes. By reducing the number of particles, the planar modes gradually disappear, as the system approaches the pure multilayer geometry (without any inclusions).

So far, all the calculations have been done assuming non-absorbing materials. In reality this cannot be neglected. Calculations show that absorption efficiently suppresses the modes (Fig. 7c) and influences the diffraction efficiency, as predicted by the model developed by Yablouovich and Cody.<sup>24</sup>

The FEM method cannot account for the stochastic nature of scattering surfaces. It would be possible to run many



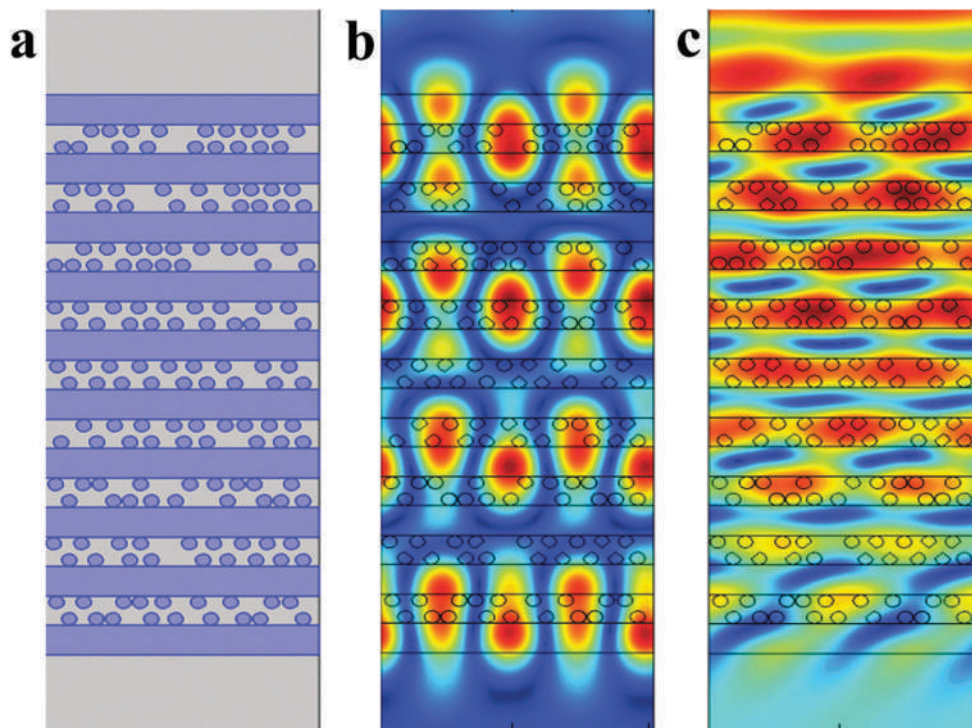


Fig. 7 (a) A geometry of the FEM model. (b) Intensity of electro-magnetic field at the resonance wavelength. Calculation were performed assuming that the angle of incidence is  $\alpha = 0$ , wavelength 624 nm and there is no absorption. (c) Field distribution with absorption included in the model. Parameters are the same as in (b).

variations of the same model with different surface profiles (but the same RMS) and then average the results. However, this would be very time consuming, and periodic boundary conditions would still introduce periodic repetition of spherical particle arrangements. To efficiently model this type of interaction we modified a transfer matrix method (TMM) to calculate the reflectance of the Bragg grating. This is a well known technique used to calculate the propagation of electromagnetic (EM) waves in a multilayer medium. Fresnel equations are used to establish the matrix relation between the EM field at the beginning and end of each layer.<sup>32</sup> The resulting EM field of the whole structure is obtained as a result of matrix multiplication of matrices corresponding to individual layers. Scattering was accounted for by simply correcting the Fresnel reflection coefficient by subtracting the intensity of scattered radiation. Absorption losses, due to scattering, were calculated using the theory of Yablonoich and Cody.<sup>24</sup> TMM software, developed by Junesch *et al.*<sup>33</sup> and made publicly available, was modified to account for scattering enhanced absorption. Further details can be found in the previous publication.<sup>8</sup>

We used parameters corresponding to pullulan diffraction gratings recorded in our experiments: 40 layers with 135 nm thickness and 130 nm air space, refractive index  $n_i = 1.45$ . The RMS roughness was calculated from the statistics of nanosphere size and their surface distribution, as determined from a series of FEGSEM images (two of them can be seen in Fig. 3). We found that the average particle size is  $55 \text{ nm} \pm 17 \text{ nm}$  and their density is  $58 \pm 12 \text{ particles } \mu\text{m}^{-2}$  (corresponding to the

average distance of  $131 \pm 14 \text{ nm}$ ). The associated RMS roughness is calculated by averaging integral of the square of the surface profile over the interval  $L$  and taking a square root of the result. The resulting RMS roughness is  $34.4 \pm 16.4 \text{ nm}$ .

There is an important word of caution: in order to get a golden wing color, the dimensional and optical parameters of each individual layer should be kept within quite tight tolerances – a condition completely impossible to satisfy in the real world. It is more realistic to expect significant variability of all the parameters. We have chosen to vary the most important ones – RMS roughness and layer thickness within  $\pm 30\%$  (according to the normal distribution). The particular value of  $\pm 30\%$  was chosen in accordance with the large variability of particle size ( $\pm 30\%$ ) and their surface density ( $\pm 20\%$ ). The angle of incidence was also allowed to fluctuate within  $\pm 10$  degrees – thus imitating the finite angular range of the incident radiation.

As a result, 160 different spectra were calculated. Each individual spectral curve is irregular with multiple peaks, corresponding to irregularities in the volume grating structure. Individual spectra were averaged – corresponding to natural spectral averaging by the detecting instrument or an observer. Our calculations have shown that the best fit of the experimentally recorded spectrum is obtained assuming that the surface roughness is 45 nm. This is larger than the 34.4 nm RMS roughness, found from FEGSEM images, but still within the uncertainty interval of  $\pm 16.4 \text{ nm}$ . The resulting curve is shown in red color in Fig. 8, together with several individual

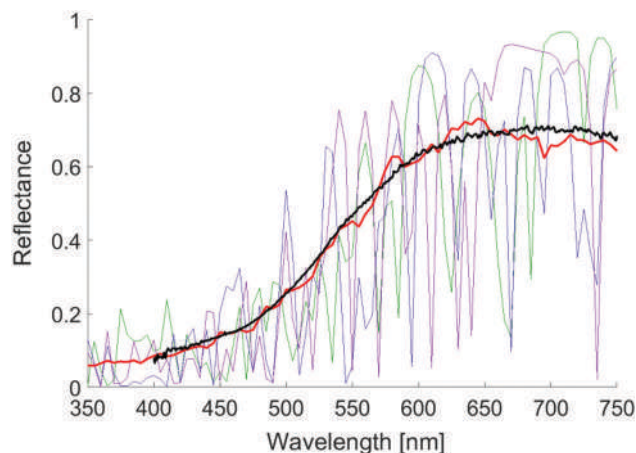


**Fig. 8** Reflectance spectrum of a model in Fig. 7(a) calculated by transfer matrix method with scattering effects included (red curve). 160 individual spectra were calculated to represent natural variability of the grating (three of them can be seen in violet, green and blue color). The final reflectance spectrum (red curve) was calculated by averaging individual spectra. Experimentally recorded spectrum of DCP is shown for reference (black curve).

spectra (violet, blue and green color). The theoretical spectrum appears noisy because the finite number of individual spectral curves (used in the calculation) cannot completely make the resulting curve smooth. By comparing the averaged spectrum with the experimentally recorded one (black curve in Fig. 8), agreement appears quite good.

## Discussion and conclusions

As far as we know, DCP is the only material capable of artificially introducing spherical nano-particles inside the Bragg grating, thus well imitating wing-scales of the *Diachrysis chrysitis* moth. Both pullulan (Fig. 3b) and butterfly's wing (Fig. 2c) possess a number of layers with rough internal surfaces (RMS roughness between 20 and 100 nm). The result is the same: strong suppression of radiation reflected in the UV–blue part of the spectrum. In this spectral range, light is strongly scattered by the rough surfaces and guided through the planar layers. Even a small amount of absorption is being enhanced by the increased path length.

It is interesting to discuss the mechanisms of nanoparticle formation both in *D. chrysitis* and DCP. In the case of *D. chrysitis* moth, we are not able to describe the exact mechanism of wing scale structure growth, because it was beyond this study. However, it is known that the wing scales are dead remnants of cells, whose main constituent is chitin (a natural polysaccharide). Chitin production and excretion are the result of a complicated biochemical process.<sup>34</sup> Additionally, according to Saranathan *et al.*<sup>35</sup> and Dinwiddie *et al.*,<sup>36</sup> wing-scale structures are produced by the complex growth of the cellular plasma membrane and intracellular smooth endoplasmic reticulum. The process is highly unpredictable as supported by the significant body of literature devoted to the, so called, cellular noise.<sup>37</sup> It was found that even genetically identical cells express random variation of

their properties, such as size, structure or protein level. In the case of DCP, we proposed the non-solvent induced phase separation as the main process behind the pullulan nano-sphere particle formation, as fully described in the main body of the paper.

In conclusion, we have created a peculiar kind of volume diffraction grating, where the nano-spherical particles are introduced between the grating layers. It was created through a combination of the holographic method (top-down technique) and non-solvent-induced phase separation (bottom-up method). The bandgap is strongly influenced by the scattering and light intensity enhancement inside the grating layers. Large size gratings can be fabricated simply and quickly (in a few minutes). It was found that the DCP grating has excellent mechanical and environmental stability.

Such multilayer materials might be of interest in solar energy collection to selectively absorb the most energetic photons of UV–blue light, while reflecting unusable long wavelength radiation.<sup>38,39</sup>

## Conflicts of interest

There are no conflicts to declare.

## Acknowledgements

The authors express their gratitude to the Ministry of Education, Science and Technological Development of the Republic of Serbia for supporting this research through projects ON171038, III45016, III43002.

## References

- 1 S. Berthier, *Photonique des Morphos*, Springer Science & Business Media, 2010.
- 2 D. Pantelić, S. Čurčić, S. Savić-Šević, A. Korać, A. Kovačević, B. Čurčić and B. Bokić, *Opt. Express*, 2011, **19**, 5817.
- 3 H. Arwin, T. Berlind, B. Johs and K. Järrendahl, *Opt. Express*, 2013, **21**, 22645.
- 4 D. Azoifeifa, H. Arguedas and W. Vargas, *Opt. Mater.*, 2012, **35**, 175.
- 5 C. Campos-Fernández, D. Azoifeifa, M. Hernández-Jiménez, A. Ruiz-Ruiz and W. Vargas, *Opt. Mater. Express*, 2011, **1**, 85.
- 6 M.-N. Wu, C.-Y. Chen and W. Pan, *AIP Adv.*, 2015, **5**, 127227.
- 7 J. P. Vigneron, M. Ouedraogo, J.-F. Colomer and M. Rassart, *Phys. Rev. E: Stat. Phys., Plasmas, Fluids, Relat. Interdiscip. Top.*, 2009, **79**, 021907.
- 8 D. Pantelić, S. Savić-Šević, D. Stojanović, S. Čurčić, A. Krmpot, M. Rabasović, D. Pavlović, V. Lazović and V. Milošević, *Phys. Rev. E*, 2017, **95**, 032405.
- 9 O. Karthaus, *Biomimetics in photonics*, CRC Press, 2013.
- 10 J. P. Vigneron, M. Rassart, C. Vandembem, V. Lousse, O. Deparis, L. Biró, D. Dedouaire, A. Cornet and P. Defrance, *Phys. Rev. E: Stat. Phys., Plasmas, Fluids, Relat. Interdiscip. Top.*, 2006, **73**, 041905.

- 11 H. Butt, A. Yetisen, D. Mistry, S. A. Khan, M. U. Hassan and S. H. Yun, *Adv. Opt. Mater.*, 2016, **4**, 497.
- 12 K. Watanabe, K. Kanda, Y. Haruyamaet, T. Kaito and S. Matsui, *J. Vac. Sci. Technol., B*, 2005, **23**, 570.
- 13 X. Liu, S. Zhu, D. Zhang and Z. Chen, *Mater. Lett.*, 2010, **64**, 2745.
- 14 K. Krogman, R. Cohen, P. Hammond, M. Rubner and B. Wang, *Bioinspiration Biomimetics*, 2013, **8**, 045005.
- 15 M. Campbell, D. Sharp, M. Harrison, R. Denning and A. Turberfield, *Nature*, 2000, **404**, 53.
- 16 M. Escuti, J. Qi and G. Crawford, *Opt. Lett.*, 2003, **28**, 522.
- 17 Y. Miklyaev, D. Meisel, A. Blanco and G. von Freymann, *Appl. Phys. Lett.*, 2003, **82**, 1284.
- 18 R. Ma, J. Xu and W. Tam, *Appl. Phys. Lett.*, 2006, **89**, 081116.
- 19 M. H. Kok, R. Ma, J. C. W. Lee, W. Y. Tam, C. T. Chan and P. Sheng, *Phys. Rev. E: Stat. Phys., Plasmas, Fluids, Relat. Interdiscip. Top.*, 2005, **72**, 047601.
- 20 R. H. Siddique, R. Hünig, A. Faisal, U. Lemmer and H. Hölscher, *Opt. Mater. Express*, 2015, **5**, 996.
- 21 M. McNamara, D. Briggs, P. Orr, S. Wedmann, H. Noh and H. Cao, *PLoS Biol.*, 2011, **9**, e1001200.
- 22 J. Springer, A. Porube and M. Vanacek, *J. Appl. Phys.*, 2004, **96**, 5329.
- 23 D. Domine, F.-J. Haug, C. Battaglia and C. Ballif, *J. Appl. Phys.*, 2010, **107**, 044504.
- 24 E. Yablonovich and G. Cody, *IEEE Trans. Electron Devices*, 1982, **ED-29**, 300.
- 25 S. Savić Šević and D. Pantelić, *Appl. Opt.*, 2007, **46**, 287.
- 26 N. Kasoju, N. Hawkins, O. Pop-Georgievski, D. Kubies and F. Vollrath, *Biomater. Sci.*, 2016, **4**, 460.
- 27 E. Piacentini, D. Shanthana Lakshmi, A. Figoli, E. Drioli and L. Giorno, *J. Membr. Sci.*, 2013, **448**, 190.
- 28 S. Aruna, P. Binsy, E. Richard and B. Basu, *Appl. Surf. Sci.*, 2012, **258**, 3202.
- 29 A. Kaya, X. Du, Z. Liu, J. Lu, J. Morris, W. Glasser, T. Heinze and A. Esker, *Biomacromolecules*, 2009, **10**, 2451.
- 30 Z. Fang, B. Patterson and M. Turner, *Mater. Character.*, 1993, **31**, 177.
- 31 H. Davies, *Proc. IEEE*, 1954, **101**, 209.
- 32 B. Wolf, *Principles of Optics*, Pergamon, 1980.
- 33 J. Junesch, T. Sannomiya and A. B. Dahlin, *ACS Nano*, 2012, **6**, 10405.
- 34 H. Merzendorfer and L. Zimoch, *J. Exp. Biol.*, 2003, **206**, 4393.
- 35 V. Saranathan, C. O. Osuji, S. G. J. Mochrie, H. Noh, S. Narayanan, A. Sandy, E. R. Dufresne and R. O. Prum, *PNAS*, 2010, **107**, 11676.
- 36 A. Dinwiddie, R. Null, M. Pizzano, L. Chuong, A. Leigh Krup, H. E. Tan and N. H. Patel, *Dev. Biol.*, 2014, **392**, 404.
- 37 I. Johnston, B. Gaal, R. Pires das Neves, T. Enver, F. Iborra and N. Jones, *PLoS Comput. Biol.*, 2012, **8**, e1002416.
- 38 J. Nagel and M. Scarpulla, *Opt. Express*, 2010, **18**, 139.
- 39 N. Dahan and J. Greffet, *Opt. Express*, 2012, **20**, 530.





# Inducing LIPSS on multilayer thin metal films by femtosecond laser beam of different orientations

Aleksander G. Kovačević<sup>1</sup> · Suzana M. Petrović<sup>2</sup> · Branislav Salatić<sup>1</sup> · Marina Lekić<sup>1</sup> · Borislav Vasić<sup>1</sup> · Radoš Gajić<sup>1</sup> · Dejan Pantelić<sup>1</sup> · Branislav M. Jelenković<sup>1</sup>

Received: 3 November 2019 / Accepted: 12 May 2020 / Published online: 28 May 2020  
© Springer Science+Business Media, LLC, part of Springer Nature 2020

## Abstract

The occurrence of laser-induced periodic surface structures (LIPSS) has been known for a while. Multilayer thin films, like Al/Ti, are suitable for LIPSS formation and attractive for applications—due to their wearing behavior and corrosion resistance; LIPSS generation may improve their properties as well. LIPSS properties depend not only on the material but also on the beam characteristics, like wavelength, polarization and scanning directions, etc. After exposing with NIR femtosecond pulses from Coherent Mira 900 laser system in several beam exposures, we have analyzed the samples of thin metal film systems with Tescan Mira3 SEM and NTegra AFM. The formation of LIPSS is most probably due to the generation of surface plasmon polariton, through the periodic distribution of energy in the interaction zone which lead to thermal processes in layers and interfaces. Two types of LIPSS were generated, which differ in shape, orientation and in ablation pronounced or not. For consecutive interactions in the same direction, LIPSS maintained its orientation, while for orthogonal passes LIPSS with mutually orthogonal orientation were generated. LIPSS period fluctuated between 320 and 380 nm and structures with pronounced ablation have significantly smaller width. Probable mechanism is that for greater accumulated energy pronounced ablation takes place giving LIPSS in the form of trenches or grooves, while for less accumulated energy the buildup of the material—probably due to pronounced oxidation—lead to LIPSS in the form of hills or ridges.

**Keywords** Laser nanostructuring · Thin metal films · LIPSS · Structures orientation

---

This article is part of the Topical Collection on Advanced Photonics Meets Machine Learning.

---

Guest Edited by Goran Gligoric, Jelena Radovanovic and Aleksandra Maluckov.

---

✉ Aleksander G. Kovačević  
Aleksander.Kovacevic@ipb.ac.rs

<sup>1</sup> Institute of Physics, University of Belgrade, Belgrade, Serbia

<sup>2</sup> Institute of Nuclear Sciences “Vinča”, University of Belgrade, Belgrade, Serbia

## 1 Introduction

Interaction of pulsed laser beam with surfaces yields the appearance of LIPSS (laser-induced periodic surface structures). The occurrence of LIPSS has long been known and studied (Birnbaum 1965; Van Driel et al. 1982; Sipe et al. 1983; Young et al. 1984; Ursu et al. 1985). It has been studied on variety of materials: metals (Ursu et al. 1985; Wang and Guo 2005; Vorobyev and Makin 2007; Vorobyev and Guo 2008, 2013), semi-conductors (Von der Linde et al. 1997; Bonse and Krüger 2010; Bonse et al. 2011; Varlamova et al. 2014), dielectrics (Reif et al. 2008), graphite (Goloso et al. 2011), compounds (Kautek et al. 2005; Gakovic et al. 2011), diamond (Shinoda et al. 2009), graphene (Beltaos et al. 2014). LIPSS properties depend not only on the material but also on the beam characteristics, like wavelength, polarization and scanning directions, etc. (Kovačević et al. 2017).

Surface morphology is a key factor in controlling the optical, mechanical, wetting, chemical, biological, and other properties of a solid surface. LIPSS may improve material properties by functionalization and may widen applications: structural coloring, absorptance enhancement, antireflective films, biomedical applications, optofluidics applications, holography, anti-counterfeiting, decorating, sensing, catalysis, optical data storage (Vorobyev and Guo 2013).

The occurrence of LIPSS can be viewed as an inherent phenomena of the interaction of the ultrafast beam with solid surface, with main characteristics that the spatial period of LIPSS is less than the beam wavelength. The orientation depends on the incident beam polarization direction. Generation is explained by self-organization or by surface plasmon polaritons (SPP) (Vorobyev and Makin 2007; Reif et al. 2008). Incident wave induces oscillations of charges (surface plasmon) and SPP forms as the coupling between incident and induced waves; in this way periodic distribution of energy is formed on the surface.

Two types of LIPSS are reported: low spatial frequency LIPSS (LSFL) and high spatial frequency LIPSS (HSFL) (Bonse et al. 2005). LSFL period  $\lesssim$  wavelength and HSFL period  $<$  wavelength/2. Named after their size (magnitude of spatial frequency), their orientation in respect to the polarization direction is not yet fully understood. It seems that LSFL orientation is perpendicular to polarization for metals and semiconductors (Bonse et al. 2012). Due to SPP, periodical distribution of thermal energy on the surface can instigate thermal processes. The occurrence of metal-oxide, or thermochemical type of LIPSS has been reported on Ti, Ni, Cr and NiCr surfaces, as well as ablative LIPSS and models have been proposed (Öktem et al. 2013; Dostovalov et al. 2017, 2019a).

When creating LIPSS on multilayer thin metal films, the underneath layer has an important role. In the example of Al/Ti multilayer film (Kovačević et al. 2015), Ti and Al have different electron heat conductivity and electron–phonon coupling. Top layer (Al) electrons accept energy and quickly transfer to the next layer (Ti). Strong coupling keeps the energy in Ti and away from topmost Al. In this way, the damage threshold for Al increases which preserves LIPSS for longer expositions. In this work, we have examined the LIPSS generated upon consecutive scanning over the same area of same and of different scanning orientations. By changing the parameters of the beam (fluence, scanning speed, scanning number and directions over the same area) the formation of LIPSS was affected. Two types of LIPSS, which differ in shape, orientation to the incoming beam polarization and in ablation pronounced or not, are generated and examined during repeated consecutive scanning of same and orthogonal directions. For lower accumulation on energy, LIPSS in the form of ridges formed while for higher fluences and accumulated energies, the generation of LIPSS gave prevalence to the ablation. After repeated consecutive scanning along the

same trajectory LIPSS preserved to some extent. Also, during scanning along close parallel lines, LIPSS from one line affected generation of LIPSS from neighboring line. Overlapping scanning lines should generate LIPSS mutually perpendicular. We have examined the three cases of LIPSS: repeated consecutive scanning along same trajectory, scanning with close parallel lines, and scanning with perpendicular lines. The results can be of use in functionalization of materials by LIPSS forming with possible impact in wetting and biomedical applications.

## 2 Experiment and methods

The samples were prepared by D.C. ion sputtering in a single vacuum run, using Ar ions and switching from one target to the other. Targets were 99.9% pure Al and Ti deposited on a Si(100) wafer as a substrate. In this way, 5×(Al/Ti) multilayer structures have been generated, where each layer was 13 nm thick and total thickness of the multilayer structure was 130 nm.

Coherent Mira 900 laser system was a source of NIR femtosecond pulses (wavelength 730–840 nm, repetition rate 76 MHz, fluence 145–260 mJ/cm<sup>2</sup>) pumped by Verdi V10 Nd:YVO<sub>4</sub> CW laser (wavelength 532 nm, power 10 W) for exposition of the samples. Steering and focusing was a part of a modified optical microscope with 2D mirror scanner (objective 40×, NA 0.65). Ocean optics HR2000CG UV-NIR fiber spectrometer was used for spectral detection. The samples have been analyzed with Tescan Mira3 SEM and NTe-gra Prima AFM under ambient conditions. The numerical simulations have been performed by COMSOL Multiphysics package, with one-dimensional two-temperature (1D TTM) model. Basic relations underlying the TTM model were proposed by Anisimov (Anisimov et al. 1974). The model observes the electron and lattice subsystems. TTM model has been used for many years to calculate the temperature of the electrons and lattice during interaction of ultrashort laser pulses with different materials. All necessary physical quantities and constants that we used in the simulation can be found in the literature (Majchrzak et al. 2010a, b). The fs beam from laser was introduced into the modified microscope onto the steering two-axis scanning mirror system and transferred through the objective of the microscope to the sample.

Patterns used for interaction are presented in Fig. 1. For consecutive repeated scanning over same trajectory, the pattern in the form of letter “N” is used (Fig. 1a). The laser beam traverses over the sample surface following the pattern of the letter. At first location, it “writes” one letter. At second (neighboring) location, it traverses the same trajectory twice, writing two letters one over another. At third location, it writes three letters, and so on. The pattern used for perpendicular overlapped scanning is composed of set of parallel lines and the sample is rotated by 90° (Fig. 1b).

## 3 Results and discussion

The samples were exposed to laser beam of 730, 800 and 840 nm of wavelength with different fluences. Irradiated areas were examined by SEM and AFM. For specified parameters, simulations of 1D temperature distribution were performed.

In Fig. 2, the results after beam of 800 nm wavelength and 153 mJ/cm<sup>2</sup> of fluence repeatedly scanned from 1 to 10 times over the surface are presented. The area where beam



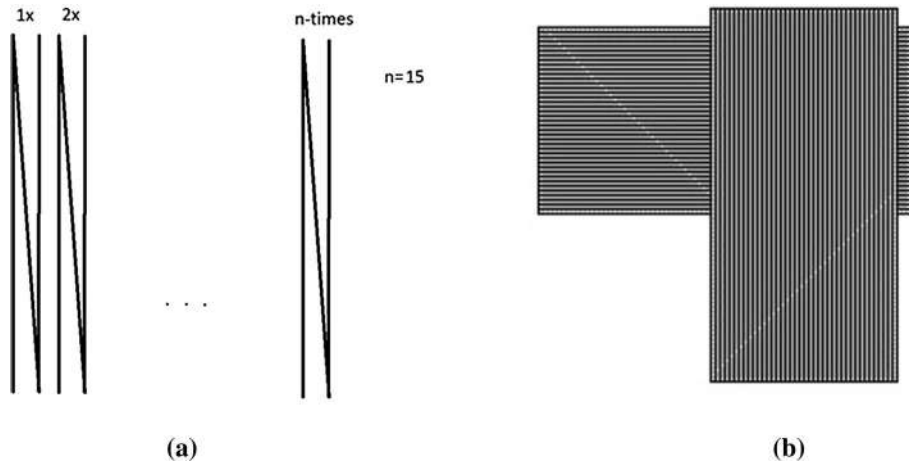


**Fig. 1** Implemented patterns of scanning: **a** for consecutive repeated scanning; **b** for perpendicular overlapped scanning

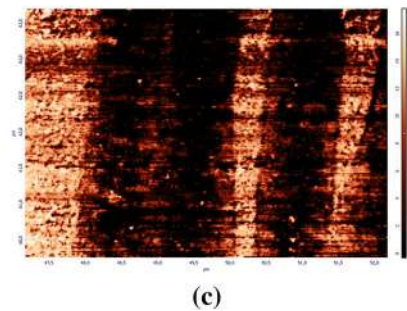
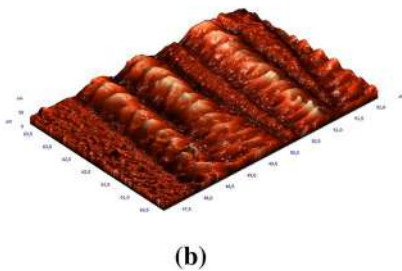
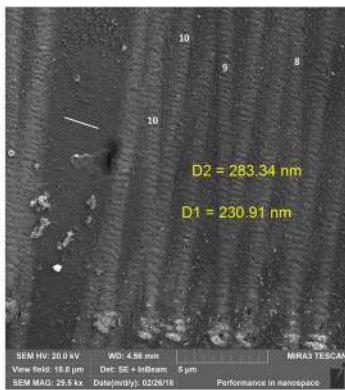


**Fig. 2** LIPSS generated after beam of  $153 \text{ mJ/cm}^2$  repeatedly scanned over the same trajectory: **a** SEM of the area of 8–10 passes; **b** AFM, detailed portion of the area in **a**—rendered area is  $(3 \times 5) \mu\text{m}$  and maximal height is  $50 \text{ nm}$ ; **c** graphical presentation of the AFM current (a.u.) of the area in **b**

scanned 8, 9 and 10 times along the same trajectory, following the shape of the letter “N”, is shown in Fig. 2a. White line on the left side of the image presents polarization direction. The beam repetition rate was 76 MHz, diameter  $\sim 1.2 \mu\text{m}$ , scanning speed  $242 \mu\text{m/s}$ . Effective number of pulses (number of pulses which affect the area of a beam spot) for one pass is 317,000. LIPSS in the form of ridges parallel to the polarization direction with spatial period of  $\sim 283 \text{ nm}$  are generated and preserved up to 10 passes. In Fig. 2b, detailed AFM view of a part of the area from Fig. 2a which shows 10 passes is presented. AFM current of the area from Fig. 2b is shown in Fig. 2c.

The simulation of the lattice temperature from the surface to the bulk is shown in Fig. 3. Odd layers (Al) are presented with light grey bars, even layers (Ti) are presented with grey bars, while substrate (Si) is presented with dark grey bar. After 1.25 ps (Fig. 3a), the temperature reaches maximum in the second (Ti) layer. After 20 ps (Fig. 3b), the temperature reaches maximum in the first (Al) layer.

In Fig. 4, the results after beam of: (a) 730 nm wavelength and  $145 \text{ mJ/cm}^2$  fluence (repetition rate 76 MHz, diameter  $\sim 1 \mu\text{m}$ ) scanned 15 times (scanning speed  $1.14 \text{ mm/s}$ , effective number of pulses for one pass 67,000) and (b) 800 nm wavelength and  $215 \text{ mJ/cm}^2$  fluence (repetition rate 76 MHz, diameter  $\sim 1.1 \mu\text{m}$ ) scanned 10 times (scanning speed  $24 \mu\text{m/s}$ , effective number of pulses for one pass 667,000) along the same trajectories are presented. In Fig. 4a, LIPSS are in the form of ridges (spatial period of  $\sim 278 \text{ nm}$ ) parallel to the polarization direction. In Fig. 4b, LIPSS are in the form of grooves (spatial period of  $\sim 370 \text{ nm}$  and groove width of  $\sim 80 \text{ nm}$ ) perpendicular to the polarization. In both cases LIPSS are preserved up to 15 and 10 passes, consecutively. Higher fluence provoked the appearance of groove-type of LIPSS. Spatial temperature distribution is similar in shape to the distributions shown in Fig. 3.

In order to create structures of mutual perpendicular direction at the same area, we performed perpendicular consecutive scanning of two (same) patterns by sample rotation (Fig. 1b). The beam was of 840 nm wavelength and the fluence was set to  $\sim 182 \text{ mJ/cm}^2$  in order to generate groove-type of LIPSS. The beam repetition rate was 76 MHz, scanning speed  $1.5 \text{ mm/s}$ , diameter  $\sim 1.1 \mu\text{m}$ , Effective number of pulses for one pass is 51,000.

In Fig. 5a, the interaction area of the sample with two consecutive beam scanning of the same pattern (Fig. 1b) is presented. The right-hand and lower parts of the image present areas where patterns don't overlap, while central, upper and left parts present overlapped patterns. Magnified portion of the right-hand part, Fig. 5b, shows that grooves of two

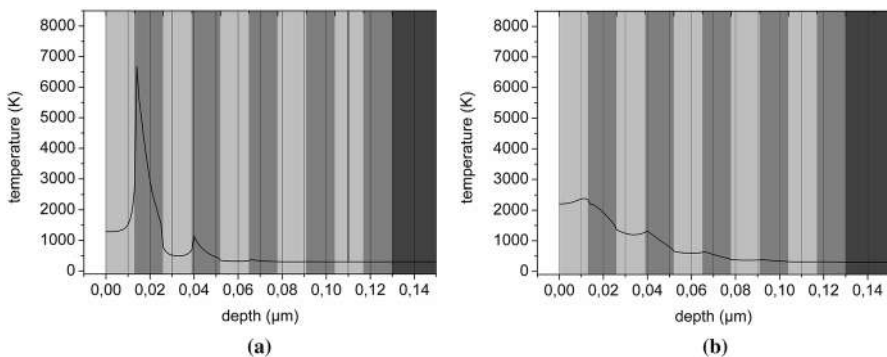


**Fig. 3** Spatial temperature distribution from the surface to the bulk after exposition to the beam of 800 nm wavelength and  $153 \text{ mJ/cm}^2$  of fluence: **a** after 1.25 ps; **b** after 20 ps

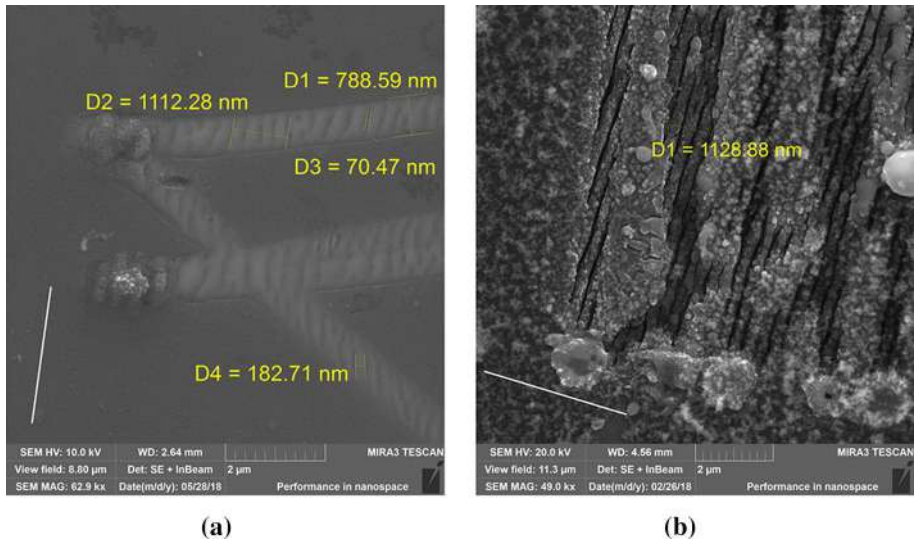
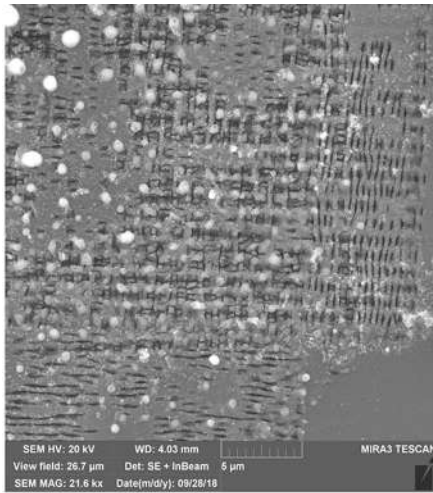


**Fig. 4** SEM micrographs of LIPSS generated after beam of: **a** 145 mJ/cm<sup>2</sup> scanned 15 passes and **b** 215 mJ/cm<sup>2</sup> scanned 10 passes. White line on the left side shows polarization orientation

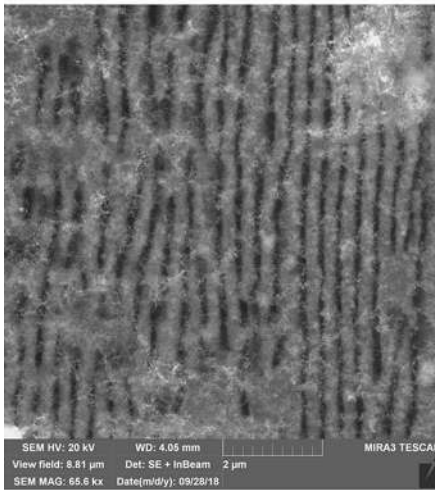
neighboring lines connect when patterns do not overlap. Where patterns overlap, Fig. 5c, grooves don't form in connected perpendicular directions; their width ranges from 98 to 126 nm.

The decrease in the AFM current (Fig. 2c) in the areas of laser exposition could be explained by increased resistivity of the exposed areas. Interaction with the beam fostered the penetration of nitrogen and/or oxygen into the first (Al) layer increasing the resistivity, which goes well with the three-step model (Öktem et al. 2013). The lattice temperature distribution from the surface to the bulk (Fig. 3) shows the influence of the multi-layer structure. After 1.25 ps (Fig. 3a), the temperature reaches maximum in the second layer (Ti). Moreover, the temperatures are higher in Ti layers than in neighboring Al layers. This is explained by the difference between two materials characteristics (Kovačević et al. 2015). Electrons from Al can quickly transfer energy to Ti layer away from the interaction zone due to the difference in electron–phonon coupling. This increases the damage threshold in Al leading to more regular ripples. The repetition rate also influences the regularity of the LIPSS, as noted in (Dostovalov et al. 2019b): higher the repetition rate, more ordered structures are formed.

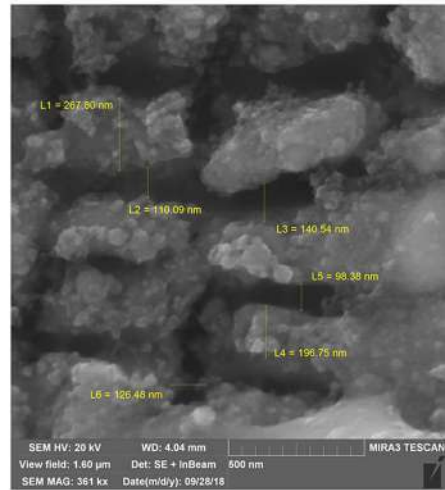
The LIPSS in the form of ridges (Figs. 2a, 4a) are most probably generated by the penetration of the nitrogen and/or oxygen from the ambient (air) into the material—thermochemical LIPSS (Öktem et al. 2013; Dostovalov et al. 2017). For higher fluences, LIPSS formed in the form of grooves by ablation mechanisms, which can be deduced by scattered ejected material seen in Fig. 4b. Slower scanning speed and low melting point of Al induced energy accumulation sufficient for Al melting and ablation, which gave the prevalence of the generation of grooves (ablative LIPSS) over ridges (thermochemical LIPSS). The comparison of the spatial periods—283 nm (Fig. 2a) and 278 nm (Fig. 4a) for ridges versus 370 nm (Fig. 4b) for grooves—suggests grooves could be classified into LSFL and ridges into HSFL; this could be also supported by their orientation in respect to the beam polarization direction (Bonse et al. 2013).



(a)



(b)



(c)

**Fig. 5** SEM micrograph of LIPSS generated by consecutive pattern scanning and sample rotation: **a** wide area; **b** right-hand part of the area in **a**; **c** magnified part of the central area in **a**

The attempt to generate intersecting perpendicular grooves was not successful. The reason is twofold. First generated LIPSS pattern distracts the formation of the second LIPSS pattern. Also, the formation of the second LIPSS pattern smears the first LIPSS pattern due to the accumulation of energy.



## 4 Conclusion

We have exposed  $5\times(\text{Al}/\text{Ti})$  multilayer thin film metal structures to fs laser beam of various wavelengths and fluences. Due to differences in materials characteristics, the temperatures are higher in Ti layers than in neighboring Al layers, which was illustrated by simulations. The appearance of LIPSS indicates lateral periodical distribution of temperature in second layer (Ti). Two types of LIPSS emerged depending on the beam fluence. For fluence lower than  $\sim 170 \text{ mJ}/\text{cm}^2$ , LIPSS in the form of ridges are generated most probably by the penetration of nitrogen and/or oxygen into the sample material (thermochemical LIPSS), which can be deduced by the decrease in the AFM current indicating the increase in resistivity. For higher fluences (above  $170 \text{ mJ}/\text{cm}^2$ ), LIPSS in the form of grooves are generated by ablation mechanisms (ablative LIPSS). Both types are preserved after 10–15 consecutive beam scanning along the same trajectory. Intersecting perpendicular LIPSS can't be successfully formed because of competing influences of perpendicular patterns causing smearing of LIPSS.


**Acknowledgements** The work was supported by the Ministry of Science of the Republic of Serbia under No. III45016, OI171038 and OI171005. The authors appreciate the valuable help from: Dr. Davor Peruško (Institute of Nuclear Sciences “Vinča”, University of Belgrade), Dr. Aleksandar Krmpot, Dr. Mihajlo Rabasović, Dr. Svetlana Savić-Šević and Vladimir Lazović (Institute of Physics, University of Belgrade), Dr. Đorđe Veljović and Dr. Željko Radovanović (Faculty of Technology and Metallurgy, University of Belgrade).

## References

- Anisimov, S.I., Kapeliovich, B.L., Perel'man, T.L.: Electron emission from metal surface exposed to ultrashort laser pulses. *Sov. Phys. JETP* **39**, 375–377 (1974)
- Beltaos, A., Kovačević, A.G., Matković, A., Ralević, U., Savić-Šević, S., Jovanović, Dj., Jelenković, B.M., Gajić, R.: Femtosecond laser induced periodic surface structures on multi-layer graphene. *J. Appl. Phys.* **116**, 204306 (2014)
- Birnbaum, M.: Semiconductor surface damage produced by ruby lasers. *J. Appl. Phys.* **36**, 3688–3689 (1965)
- Bonse, J., Krüger, J.: Pulse number dependence of laser-induced periodic surface structures for femtosecond laser irradiation of silicon. *J. Appl. Phys.* **108**, 034903 (2010)
- Bonse, J., Munz, M., Sturm, H.: Structure formation on the surface of indium phosphide irradiated by femtosecond laser pulses. *J. Appl. Phys.* **97**, 013538 (2005)
- Bonse, J., Rosenfeld, A., Krueger, J.: Implications of transient changes of optical and surface properties of solids during femtosecond laser pulse irradiation to the formation of laser-induced periodic surface structures. *Appl. Surf. Sci.* **257**, 5420–5423 (2011)
- Bonse, J., Krüger, J., Höhm, S., Rosenfeld, A.: Femtosecond laser-induced periodic surface structures. *J. Laser Appl.* **24**, 042006 (2012)
- Bonse, J., Höhm, S., Rosenfeld, A., Krüger, J.: Sub-100-nm laser-induced periodic surface structures upon irradiation of titanium by Ti:sapphire femtosecond laser pulses in air. *Appl. Phys. A* **110**, 547–551 (2013)
- Dostovalov, A.V., Korolkov, V.P., Terentyev, V.S., Okotrüb, K.A., Dultsev, F.N., Babin, S.A.: Study of the formation of thermochemical laser-induced periodic surface structures on Cr, Ti, Ni and NiCr films under femtosecond irradiation. *Quantum Electron.* **47**, 631–637 (2017)
- Dostovalov, A.V., Derrien, T.J.-Y., Lizunov, S.A., Přeučil, F., Okotrüb, K.A., Mocek, T., Korolkov, V.P., Babin, S.A., Bulgakova, N.M.: LIPSS on thin metallic films: new insights from multiplicity of laser-excited electromagnetic modes and efficiency of metal oxidation. *Appl. Surf. Sci.* **491**, 650–658 (2019a)

- Dostovalov, A.V., Okotrub, K.A., Bronnikov, K.A., Terentyev, V.S., Korolov, V.P., Babin, S.A.: Influence of femtosecond laser pulse repetition rate on thermochemical laser-induced periodic surface structures formation by focused astigmatic Gaussian beam. *Laser Phys. Lett.* **16**, 026003 (2019b)
- Gakovic, B., Radu, C., Zamfirescu, M., Radak, B., Trtica, M., Petrovic, S., Panjan, P., Zupanic, F., Ristoscu, C., Mihailescu, I.N.: Femtosecond laser modification of multilayered TiAlN/TiN coating. *Surf. Coat. Technol.* **206**, 411–416 (2011)
- Golosov, E.V., Ionin, A.A., Kolobov, Yu.R., Kudryashov, S.I., Ligachev, A.E., Makarov, S.V., Novoselov, Yu.N., Seleznev, L.V., Sinitsyn, D.V., Sharipov, A.R.: Near-threshold femtosecond laser fabrication of one-dimensional subwavelength nanogratings on a graphite surface. *Phys. Rev. B* **83**, 115426 (2011)
- Kautek, W., Rudolph, P., Daminelli, G., Kruger, J.: Physico-chemical aspects of femtosecond-pulse-laser-induced surface nanostructures. *Appl. Phys. A* **81**, 65–70 (2005)
- Kovačević, A.G., Petrović, S.M., Bokić, B.M., Gaković, B.M., Bokorov, M.T., Vasić, B.Z., Gajić, R.B., Trtica, M.S., Jelenković, B.M.: Surface nanopatterning of Al/Ti multilayer thin films and Al single layer by a low-fluence UV femtosecond laser beam. *Appl. Surf. Sci.* **326**, 91–98 (2015)
- Kovačević, A.G., Petrović, S., Lazović, V., Peruško, D., Pantelić, D., Jelenković, B.M.: Inducing subwavelength periodic nanostructures on multilayer NiPd thin film by low-fluence femtosecond laser beam. *Appl. Surf. Sci.* **417**, 155–159 (2017)
- Majchrzak, E., Poteralska, J.: Two-temperature microscale heat transfer model. Part I: determination of electron parameters. *Sci. Res. Inst. Math. Comput. Sci. Czestochowa Univ. Technol.* **9**, 99–108 (2010a)
- Majchrzak, E., Poteralska, J.: Two-temperature microscale heat transfer model Part II: Determination of lattice parameters. *Sci. Res. Inst. Math. Comput. Sci. Czestochowa Univ. Technol.* **9**, 109–119 (2010b)
- Öktem, B., Pavlov, I., Ilday, S., Kalaycıoğlu, H., Rybak, A., Yavaş, S., Erdoğan, M., Ilday, F.Ö.: Nonlinear laser lithography for indefinitely large area nanostructuring with femtosecond pulses. *Nat. Photonics* **7**, 897 (2013)
- Reif, J., Varlamova, O., Costache, F.: Femtosecond laser induced nanostructure formation: self-organization control parameters. *Appl. Phys. A* **92**, 1019–1024 (2008)
- Shinoda, M., Gattass, R.R., Mazur, E.: Femtosecond laser-induced formation of nanometer-width grooves on synthetic single-crystal diamond surfaces. *J. Appl. Phys.* **105**, 053102 (2009)
- Sipe, J.E., Young, J.F., Preston, J.S., van Driel, H.M.: Laser-induced periodic surface structure. I. Theory. *Phys. Rev. B* **27**, 1141–1154 (1983)
- Ursu, I., Mihailescu, I.N., Prokhorov, A.M., Konov, V.I., Tokarev, V.N.: On the role of the periodical structures induced by powerful laser irradiation of metallic surfaces in the energy coupling process. *Phys. B+C* **132**, 395–402 (1985)
- Van Driel, H.M., Sipe, J.E., Young, J.F.: Laser-induced periodic surface structure on solids: a universal phenomenon. *Phys. Rev. Lett.* **49**, 1955–1958 (1982)
- Varlamova, O., Martens, C., Ratzke, M., Reif, J.: Genesis of femtosecond-induced nanostructures on solid surfaces. *Appl. Opt.* **53**, I10–I15 (2014)
- Von der Linde, D., Sokolowski-Tinten, K., Bialkowski, J.: Laser–solid interaction in the femtosecond time regime. *Appl. Surf. Sci.* **109–110**, 1 (1997)
- Vorobyev, A.Y., Guo, C.: Femtosecond laser-induced periodic surface structure formation on tungsten. *J. Appl. Phys.* **104**, 063523 (2008)
- Vorobyev, A.V., Guo, C.: Direct femtosecond laser surface nano/microstructuring and its applications. *Laser Photonics Rev.* **7**, 385–407 (2013)
- Vorobyev, A.Y., Makin, V.S.: Periodic ordering of random surface nanostructures induced by femtosecond laser pulses on metals. *J. Appl. Phys.* **101**, 034903 (2007)
- Wang, J., Guo, C.: Ultrafast dynamics of femtosecond laser-induced periodic surface pattern formation on metals. *Appl. Phys. Lett.* **87**, 251914 (2005)
- Young, J.F., Sipe, J.E., van Driel, H.M.: Laser-induced periodic surface structure. III. Fluence regimes, the role of feedback, and details of the induced topography in germanium. *Phys. Rev. B* **30**, 2001–2015 (1984)

# Laser induced mixing in multilayered Ti/Ta thin film structures

Marko Obradović<sup>1</sup>  · Janez Kovač<sup>2</sup> · Suzana Petrović<sup>1</sup> · Vladimir Lazović<sup>3</sup> · Branislav Salatić<sup>3</sup> · Jovan Ciganović<sup>1</sup> · Dejan Pjević<sup>1</sup> · Momir Milosavljević<sup>1</sup> · Davor Peruško<sup>1</sup>

Received: 12 October 2017 / Accepted: 1 June 2018 / Published online: 9 June 2018  
© Springer Science+Business Media, LLC, part of Springer Nature 2018

**Abstract** The possibility of interlayer mixing in a Ti/Ta multilayer system, induced by laser irradiation, was the main purpose of these experiments. Ti/Ta multilayer system, consisting of ten alternating Ti and Ta thin films and covered by slightly thicker Ti layer, was deposited on Si (100) wafers to a total thickness of 205 nm. Laser irradiation was performed in air by picoseconds Nd:YAG laser pulses in defocused regime with fluences of 0.057 and 0.11 J cm<sup>-2</sup>. Laser beam was scanned over the 5 × 5 mm surface area with different steps along y-axes. Structural and compositional characterisation was done by auger electron spectroscopy, X-ray photoelectron spectroscopy, atomic force microscopy, and scanning electron microscopy. Laser processing at lower fluence caused only oxidation of the top Ti layer, despite of the number of applied laser pulses. Interlayer mixing was not observed. Application of laser pulses at fluence of 0.11 J cm<sup>-2</sup> caused partial and/or complete ablation of deposited layers. In partially ablated regions considerable mixing between Ti and Ta films was registered.

**Keywords** Thin films · Multilayers · Laser irradiation · Mixing

---

This article is part of the Topical Collection on Focus on Optics and Bio-photonics, Photonica 2017

---

Guest Edited by Jelena Radovanovic, Aleksandar Krmpot, Marina Lekic, Trevor Benson, Mauro Pereira, Marian Marciniak

---

✉ Marko Obradović  
mbradovic@vin.bg.ac.rs

<sup>1</sup> VINČA Institute of Nuclear Sciences, University of Belgrade, P.O. Box 522, Belgrade 11001, Serbia

<sup>2</sup> Jožef Stefan Institute, Jamova 39, 1000 Ljubljana, Slovenia

<sup>3</sup> Institute of Physics Belgrade, University of Belgrade, Pregrevica 118, Zemun 11080, Serbia

## 1 Introduction

During the last few decades great attention is being devoted to the development of new materials for biomedical applications. Currently metallic biomaterials (stainless steels, Co–Cr alloys, Ti and its alloys) are the most widely used materials in this field, especially for orthopedic implants. An ideal metallic biomaterial should satisfy the criteria such as biocompatibility, high corrosion resistance, high strength and low elastic modulus close to that of human bones. Physical and particularly chemical characteristics of the material are to a large extent defined by their surface, so because of that, examination of thin films and coatings of biomaterials requires more attention.

Some previous investigations show that the Ti–Ta alloys are promising materials for biomedical applications due to excellent corrosion resistance and better mechanical characteristics than pure Ti (Zhou et al. 2004a, b, 2005; Zhou and Niinomi 2009; Kesteven et al. 2015; Liu et al. 2015). Multilayered metallic thin film structures are very useful for wide applications due to their properties, such as enhanced hardness or unusual phase composition, compared to single component systems (Sproul 1996). Ti/Ta multilayers belong to the so-called immiscible materials, in which chemical driving forces can prevent radiation induced atomic mixing at their interface. The absence of interlayer mixing was shown during the Ar<sup>+</sup> ion irradiation of this system up to relatively high fluence of  $2 \times 10^{16}$  ions cm<sup>-2</sup> (Milosavljević et al. 2011).

It is generally accepted that creating an appropriate porous structure on the Ti-based implant surface is very important when biocompatibility is of great concern. Chemical and thermal treatments have usually been used for creating such porous structures (Yang and Huang 2010; Nishiguchi et al. 2003; Fujibayashi et al. 2004). However, these roughening procedures induce contamination of implants. On the other hand laser irradiation provides contamination free roughening process because it enables surface treatments without direct contact and easy control of the surface roughness (Jeong et al. 2011).

Surface modification of biomaterials by ultrafast laser processing is considered an innovative technique, which contributes to improved cell integration and inhibits bacterial growth. Different types of the novel surface motives (ripples, groves, spikes) with sub-micron sized features are produced by ultrafast laser processing, while the chemical and physical properties of semiconductor, dielectric and metallic surfaces are significantly modified. Laser-assisted changes of chemistry, charge, topography and wettability of the surface can improve the degree of biocompatibility in terms of promoting cell adhesion, spreading and proliferation (Stratakis et al. 2009; Simitzi et al. 2015, 2017).

This article presents the results of structural and compositional investigations of the laser beam induced effects in Ti/Ta multilayer system. A defocused Nd:YAG laser beam was used, with two different energies. Beam was scanned over the sample surfaces. The aim of these experiments was to investigate the possibility of interlayer mixing in this system caused by irradiation with picoseconds laser pulses.

## 2 Experiment

Ti/Ta multilayer structure consisted of 10 alternate Ti and Ta thin films, with individual thickness of ~18 nm each, covered with slightly thicker Ti film (~27 nm). Total thickness of deposited structure, measured with a talystep profilometer, was ~205 nm.



Samples were deposited in a Balzers Sputtron II system, using 1.2 keV argon ions and 99.9% pure Ti and Ta targets. The base pressure in the chamber was  $\sim 2 \times 10^{-6}$  mbar, and the partial pressure of Ar during deposition was  $1 \times 10^{-3}$  mbar. Complete multilayer structure was deposited in a single vacuum run, at an average deposition rate of  $\sim 0.13$  nm  $s^{-1}$  for both materials onto (100) Si wafers at ambient temperature. The first layer deposited on the silicon substrate was titanium. Si wafers were cleaned by standard HF etch and a dip in deionised water before being mounted in the chamber.

The samples were irradiated by a defocused Nd:YAG laser beam with energies of 4 and 8 mJ. Nd:YAG laser (model EKSPLA SL212P) was operated in the fundamental transverse mode (TEM00 mode). Distribution of energy over the spots was near Gaussian with energy maximum in the centre of the laser spot. All irradiations were performed in air, and laser beam was perpendicular to the sample surface. The laser beam output characteristics were: wavelength 1064 nm, pulse duration  $\sim 150$  ps and linearly polarised. The pulse-to-pulse energy variation was  $\sim 10\%$  with typical pulse repetition rate of 10 Hz. Diameter of the laser spot on the sample surface was 3 mm, so that laser pulse fluences were 0.057 and 0.11 J  $cm^{-2}$  for energies of laser beam of 4 and 8 mJ, respectively. Laser beam was scanned over the sample surfaces with different steps along y-axis covering an area of  $5 \times 5$  mm<sup>2</sup>. Description of the analysed samples is shown in Table 1.

Compositional and structure analyses were done by auger electron spectroscopy (AES), X-ray photoelectron spectroscopy (XPS), atomic force microscopy (AFM) and scanning electron microscopy (SEM).

The depth distribution of elements in as deposited and laser treated samples was analysed by auger electron spectroscopy in the PHI SAM 545 spectrometer. For electron excitation a primary electron beam of 3 keV and 0.5  $\mu A$ , with a diameter of 40  $\mu m$ , was used. During AES depth profiling, the samples were sputtered by two symmetrically inclined Ar ion beams of 1 keV. The sputtering area was  $6 \times 6$  mm<sup>2</sup>. The quantitative composition was determined using the relative sensitivity factors provided by the instrument manufacturer.

XPS analyses were carried out on the PHITFA XPS spectrometer manufactured by physical electronics Inc. XPS spectra were excited by X-ray radiation from an Al monochromatic source. The changes of surface morphology, induced by laser treatment, were examined by atomic force microscopy (Solver PRO47) in oscillating mode. SEM analyses of samples surface and fracture cross section of sample 4 (irradiated with laser beam energy of 8 mJ) was performed by MIRA3 TESCAN microscopy.

**Table 1** Samples description

Sample	Laser beam energy (mJ)	Laser pulse fluence (J $cm^{-2}$ )	Scan speed along x-axis ( $\mu m$ $s^{-1}$ )	Step distance along y-axis ( $\mu m$ )	Total number of applied laser pulses
1	–	–	–	–	–
2	4	0.057	300	300	2670
3	4	0.057	300	200	4170
4	8	0.11	300	300	2670

### 3 Results and discussion

AES depth concentration profiles of elements in the as deposited and laser treated Ti/Ta samples are presented in Fig. 1. The surface of as deposited sample (1) is contaminated with oxygen and carbon. Concentrations of O and C are 41.7 and 42.5 at.% respectively, and they decrease very fast to a few atomic percent inside the top titanium layer. Ti and Ta layers are well separated in the whole multilayered structure. Due to small thickness (~18 nm) of individual layers and limited depth resolution of AES method, some overlapping between Ti and Ta curves is visible. This phenomenon can be assigned to limitations of the AES analytical method rather than mixing of the layers. Enhanced concentration of oxygen (about 7 at.%) was registered in the first Ti layer deposited on silicon substrate. This is a consequence of degassing of the vacuum system at the beginning of thin film deposition process and high reactivity of titanium.

In the case of lower energy of applied laser pulses (samples 2 and 3) laser irradiation induces oxidation of the top Ti layer. Oxygen signal spreads within this layer up to interface with Ta. All other layers beneath remain unaffected, and Ta and Ti signals are still well separated. Enhanced concentration of oxygen in the near surface region originates from the fact that laser irradiation was performed in air. Reason for observed increased incorporation of oxygen is the high temperature on the sample surface during the laser interaction and great reactivity of titanium. It also can be seen that time necessary for completely removing of deposited layers is higher for laser treated samples compared

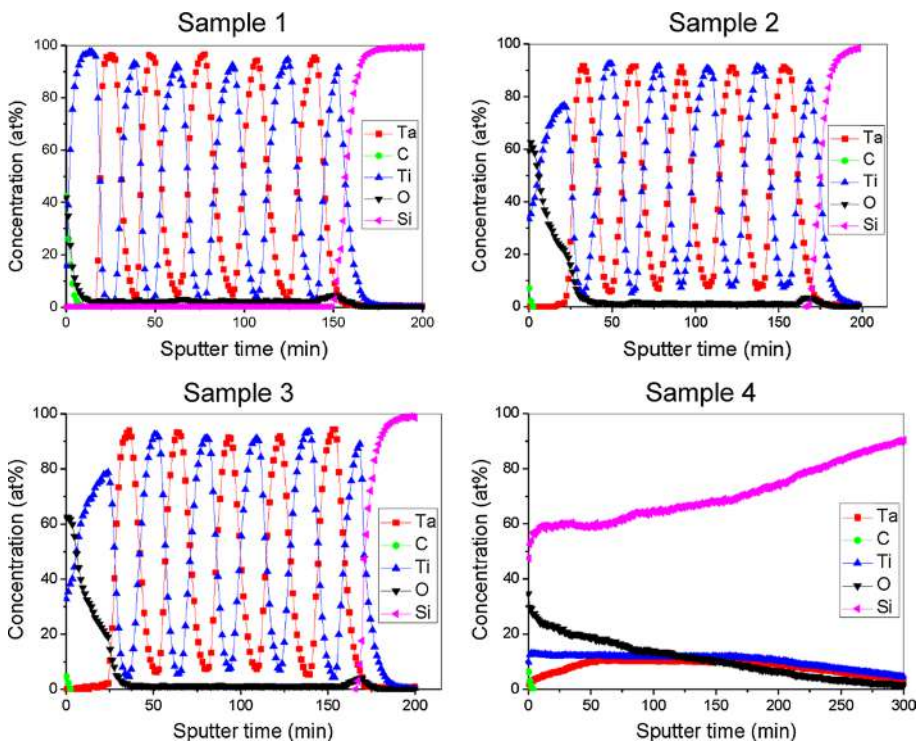


**Fig. 1** AES depth profiles of as deposited (1) and laser treated (2–4) samples

to as deposited. This phenomenon can be explained by formation of Ti–O oxides which have lower sputtering coefficients than those of pure titanium and tantalum.

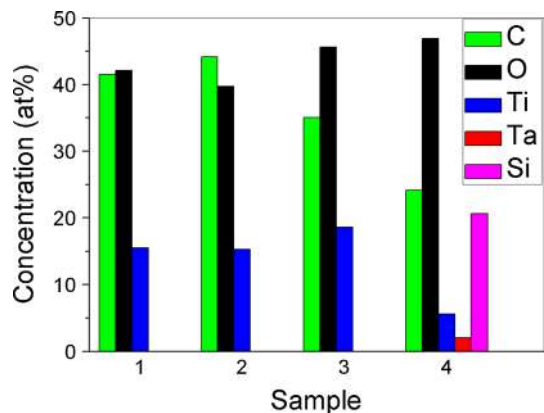
Multilayered structure was completely destroyed by applying the laser beam with higher energy (sample 4). Signals of Ti and Ta are practically equalised and spread deep into the sample, but their concentrations are considerably lower (about 10 at.%). High concentration of Si (~60 at.% at the sample surface) and lack of concentrations of Ti and Ta may be the result of inhomogeneous ablation of deposited layers. Laser spot overlapping was the greatest in the central part of irradiated sample and induced their complete removal, while at the peripheral areas, layers have not completely ablated, some still remained. It may be presumed that AES depth concentration profiles represent some average values of elements concentration that include both ablated and not fully ablated parts of the sample.

The results of surface composition of as deposited and laser treated samples, performed by XPS, are shown in Fig. 2. The aim of this analysis was to deduce whether Ta occurs at the sample surface as a result of laser irradiation. Its appearing would indicate intermixing of layers. Presence of titanium and contaminants, carbon and oxygen, was registered on the surface of as deposited sample (1). These contaminants appear on the surface of all samples due to their adsorption from atmosphere. Tantalum does not appear on the surface in the cases of laser treated samples at lower energy of laser beam despite on the number of applied laser pulses (samples 2 and 3). It occurs only for sample treated with laser beam at higher energy (sample 4). In that case a large amount of silicon was also registered on the sample surface.

XPS analysis show that titanium appeared at the sample surface in the oxide but not metal state in all analysed samples (1–4). Tantalum and silicon are in oxide state at the surface of sample 4 as well. It is well known that clean surfaces of many materials (Ti, Al, Si, etc.) spontaneously react with air, even at room temperature, to form a thin native oxide layer. These layers are usually very dense and can prevent further oxidation. Laser irradiation caused additional oxidation and oxide layer became wider, as can be seen in AES analysis for samples 2 and 3.

AES and XPS analysis show that, except the phenomenon of oxidation of the top Ti layer, multilayered Ti/Ta structure is very stable upon the laser irradiation for laser pulse fluence of  $0.057 \text{ J cm}^{-2}$  (laser beam energy 4 mJ). Appliance of higher laser pulse fluence ( $0.11 \text{ J cm}^{-2}$ ) leads to the complete destruction of this thin film structure.

**Fig. 2** XPS surface composition of as deposited (1) and laser irradiated (2–4) samples



The results of AFM analysis of as deposited and laser treated samples are shown in Fig. 3. Average surface roughness, measured over an area of  $5 \times 5 \mu\text{m}$  for all samples, is presented on the same figure.

It is obvious that laser irradiation induces enhancing of surface roughness. This increase is particularly pronounced for sample irradiated with laser pulses with higher energy (sample 4). Application of laser beam with lower energy (samples 2 and 3) causes the formation of a mesh of micro-cracks, which contributes increasing of surface roughness. This effect is more pronounced for sample irradiated with larger number of laser pulses (sample 3 compared to sample 2).

The results of SEM analysis of as deposited and laser treated samples are presented in Fig. 4. As deposited Ti/Ta sample has a flat, mirror-like surface. As was shown in AFM analysis, irradiation with lower laser pulse fluence of  $0.057 \text{ J cm}^{-2}$  causes the formation of micro-cracks on the top Ti layer.

SEM micrographs of sample 4, treated with higher laser pulse fluence, confirm the assumption about full and/or partial removing of deposited layers. Completely ablated areas are visible on the left micrograph of the sample 4. Magnified area with residual layers is shown on the right micrograph of the sample 4. Dark and bright sections within residual layered structure indicate possible mixing between Ti and Ta. Bright parts correspond to tantalum and dark to titanium.

Formation of micro-cracks may be explained by the fact that short processing cycles permit material transformations within thin films and surfaces without a significant influence on the substrate or underlying bulk material (Bäuerle 2000; Mondal et al. 2008; Petrović et al. 2012). As was mentioned earlier, on the surface of the cover Ti layer a very thin amorphous oxide film (thickness of a few nm) was formed. This formation is a consequence of high reactivity of titanium (Peruško et al. 2015). According to XPS analysis, this surface oxide layer is mainly  $\text{TiO}_2$  and it cannot follow the fast heating and quenching processes caused by laser pulses. This leads to cracking of this oxide film and enables

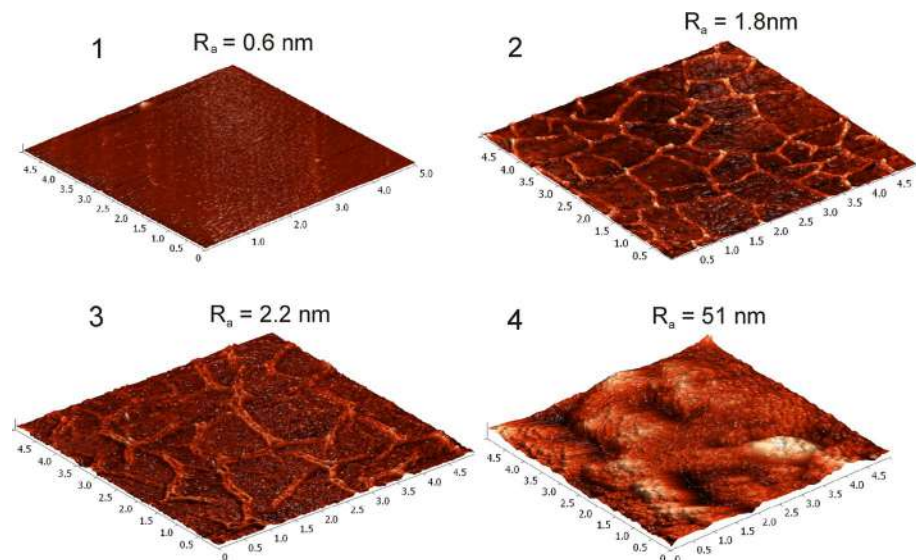


**Fig. 3** AFM images and average surface roughness of as deposited (1) and laser irradiated (2–4) samples



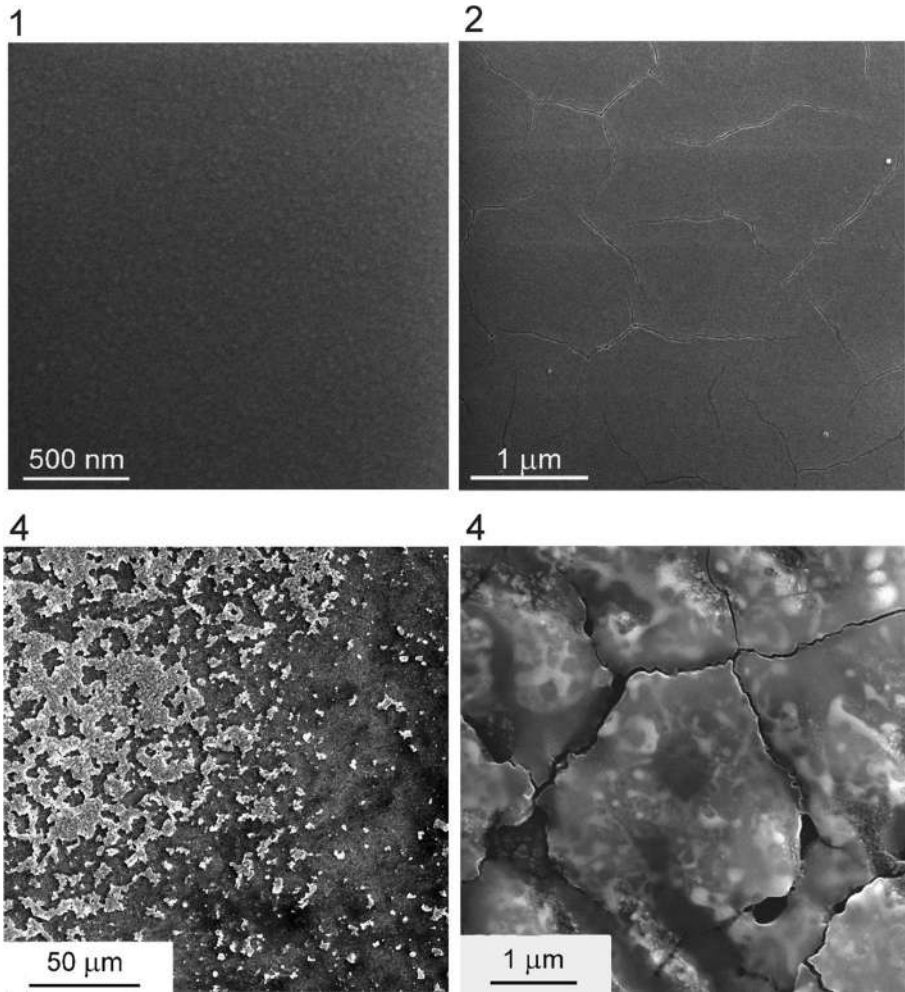


**Fig. 4** SEM analysis of surfaces of as deposited (1) and laser treated (2–4) samples

further oxidation of underlying Ti layer. AES analyses show that this process is limited to the cover layer only, for lower value of laser pulse energy. Approximate calculation of surface temperature, for laser pulse fluence of  $0.057 \text{ J cm}^{-2}$ , gives the value of 1550 K. Since the melting temperature of Ti is 1941 K, it is probably the reason for absence of melting and ablation of cover layer. For fluence of  $0.11 \text{ J cm}^{-2}$  the surface temperature reaches the value of 2280 K and in this case melting and ablation of titanium layer can be expected to appear. The melting temperature for tantalum is 2744 K and its coefficient of thermal expansion is about 30% lower compared to that of titanium. Ta thin film cannot follow the expansion of melted titanium and cracks into small fragments that are trapped and fused into Ti. Ablation of titanium includes the ablation of trapped tantalum fragments. Confirmation of this assumed mechanism for ablation could be seen in the SEM micrograph of surface of sample 4 (Fig. 4). In solidified titanium there can be seen some isolated Ta fragments.

SEM analysis of fracture cross section of sample 4 (Fig. 5) explicitly show that laser treatment with higher energy of laser pulses induces partial mixing between Ti and Ta layers. Fracture cross section of part of sample that is not affected by laser beam is present in Fig. 5a. Well separated Ti and Ta layers are clearly visible.

Micrographs shown in Fig. 5b, c are taken from the parts of sample close to boundary with unaffected zone. The layers close to Si substrate (five or six of them) stay well separated, while the upper part of multilayered structure is completely mixed.

Due to Gaussian distribution of energy over the laser spot, energy (and laser pulse fluence) is lower in this zone. Also, overlapping of laser spots near the border is smaller compared to central part of irradiated zone. Mixing between Ti and Ta layers is less pronounced immediately next to the boundary (Fig. 5b).

Moving away from the border interlayer mixing becomes more expressed (Fig. 5c). Surface roughness increases, deposited layers accumulate in the form of hills in some places and their height overcomes the total thickness of deposited layers. In other places deposited material is almost completely removed. Probably, these effects are responsible for laser induced ablation visible in Fig. 4.

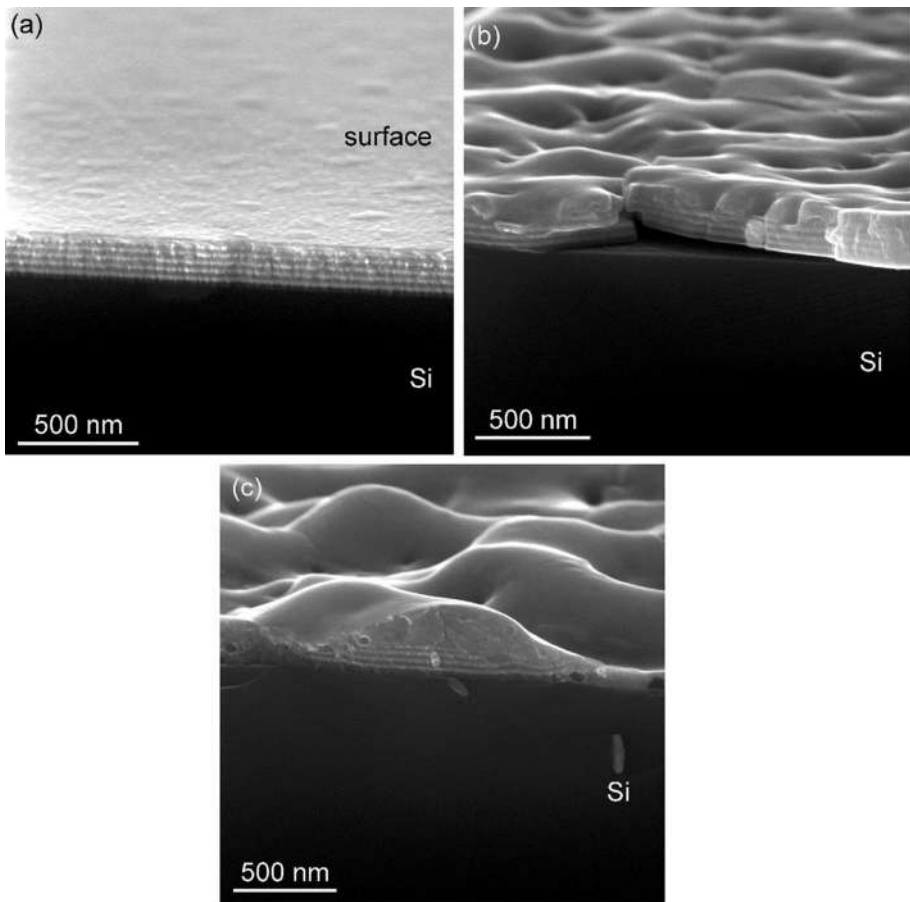


**Fig. 5** Fracture cross section of sample (4) irradiated with laser pulse fluence of  $0.11 \text{ J cm}^{-2}$

Laser induced modification of materials is based on the high temperature created at the surface during very short laser pulses. If the pulse duration is longer than a few tenths of picoseconds, laser–material interaction can be considered as thermally activated (Bäuerle 2000). It has been shown that irradiation of multilayered thin film systems by pico-seconds laser pulses induces mixing of constituent films incorporated within heat-affected zone (HAZ; Peruško et al. 2012, 2013). Approximate calculation of the HAZ (Bäuerle 2000) for this Ti/Ta multilayered system and applied laser beam parameter (duration of laser pulse of 150 ps) gives the value of 68 nm. This result coincides fairly well with observed intermixed layers shown in Fig. 5b. However, formula for HAZ contains only laser pulse duration and thermal diffusivity of materials. In that case the amount of mixed material, incorporated within HAZ, should be the same regardless of the laser pulse fluence. But, for fluence of  $0.057 \text{ J cm}^{-2}$  mixing between Ti and Ta layers was not observed. Probably, the process of interlayer mixing in this case is related to the energy of laser pulses, which must be sufficient to overcome the activity of chemical driving forces.

## 4 Conclusions

Irradiation of Ti/Ta multilayer structure, performed in air by defocused Nd:YAG picoseconds laser pulses at fluence of  $0.057 \text{ J cm}^{-2}$ , did not induce interlayer mixing regardless on the number of applied laser pulses. Only oxidation of the top Ti layer was observed under these conditions.

Appliance of the laser pulses with fluence of  $0.11 \text{ J cm}^{-2}$  leads to partial or complete ablation of multilayered structure, mixing between Ti and Ta films and large increase in surface roughness. Incomplete mixing of layers appeared in the vicinity of boundary with untreated part of sample.

Obtained results indicate that the use of picoseconds laser pulses with fluences in interval ( $0.057\text{--}0.11$ )  $\text{J cm}^{-2}$  can be very useful for mixing of titanium and tantalum layers and fabrication of a new material for medical implants. Suitable choice of films thicknesses, laser pulse fluence and scan speed over the sample surface would lead to the desired composition of this alloy.

**Acknowledgements** This research was supported by the Ministry of Education, Science and Technological Development of the Republic of Serbia, Contract No. OI 171023, and Slovenian Research Agency, Research Program P2-0082.

## References

- Bäuerle, D.: Laser Processing and Chemistry, 3rd edn. Springer, Berlin (2000)
- Fujibayashi, S., Neo, M., Kim, H.M., Kokubo, T., Nakamura, T.: Osteoinduction of porous bioactive titanium metal. *Biomaterials* **25**, 50–443 (2004)
- Jeong, Y.H., Son, I.B., Choe, H.C.: Formation of surface roughness on the Ti–35Nb–xZr alloy using femto-second laser for biocompatibility. *Proc. Eng.* **10**, 2393–2398 (2011)
- Kesteven, J., Kannan, M.B., Walter, R., Khakbaz, H., Choe, H.C.: Low elastic modulus Ti–Ta alloys for load-bearing permanent implants: enhancing the biodegradation resistance by electrochemical surface engineering. *Mater. Sci. Eng. C* **46**, 226–231 (2015)
- Liu, Y., Li, K., Wu, H., Song, M., Wang, W., Li, N., Tang, H.: Synthesis of Ti–Ta alloys with dual structure by incomplete diffusion between elemental powders. *J. Mech. Behav. Biomed.* **51**, 302–312 (2015)

- Milosavljević, M., Milinović, V., Peruško, D., Grce, A., Stojanović, M., Pjević, D., Mitrić, M., Kovač, J., Homewood, K.P.: Stability of nano-scaled Ta/Ti multilayers upon argon ion irradiation. *Nucl. Instrum. Method B* **269**, 2090–2097 (2011)
- Mondal, A.K., Kumar, S., Blawert, C., Dahotre, N.B.: Effect of laser surface treatment on corrosion and wear resistance of ACM720 Mg alloy. *Surf. Coat. Technol.* **202**, 3187–3198 (2008)
- Nishiguchi, S., Fujibayashi, S., Kim, H.M., Kokubo, T., Nakamura, T.: Biology of alkali and heat-treated titanium implants. *J. Biomed. Mater. Res. A* **67**, 26–35 (2003)
- Peruško, D., Petrović, S., Kovač, J., Stojanović, Z., Panjan, M., Obradović, M., Milosavljević, M.: Laser-induced formation of intermetallics in multilayered Al/Ti nano-structures. *J. Mater. Sci.* **47**(10), 4488–4495 (2012)
- Peruško, D., Čizmović, M., Petrović, S., Siketić, Z., Mitrić, M., Pelicon, P., Dražić, G., Kovač, J., Milinović, V., Milosavljević, M.: Laser irradiation of nano-metric Al/Ti multilayers. *Laser Phys.* **23**, 036005 (2013)
- Peruško, D., Kovač, J., Petrović, S., Dražić, G., Mitrić, M., Milosavljević, M., Ciganović, J.: Intermixing and phase transformations in Al/Ti multilayer system induced by picosecond laser beam. *Thin Solid Films* **591**, 357–362 (2015)
- Petrović, S., Peruško, D., Kovač, J., Panjan, M., Gaković, B., Radak, B., Janković-Mandić, L., Trtica, M.: Laser treatment of nanocomposite Ni/Ti multilayer thin films in air. *Surf. Coat. Technol.* **211**, 93–97 (2012)
- Simitzi, C., Efstathopoulos, P., Kourgiantaki, A., Ranella, A., Charalampopoulos, I., Fotakis, C., Athanasakis, I., Stratakis, E., Gravanis, A.: Laser fabricated discontinuous anisotropic microconical substrates as a new model scaffold to control the directionality of neuronal network outgrowth. *Biomaterials* **67**, 115–128 (2015)
- Simitzi, C., Ranella, A., Stratakis, E.: Controlling the morphology and outgrowth of nerve and neuroglial cells: the effect of surface topography. *Acta Biomater.* **51**, 21–52 (2017)
- Sproul, W.D.: New routes in the preparation of mechanically hard films. *Science* **273**, 889–892 (1996)
- Stratakis, E., Ranella, A., Farsari, M., Fotakis, C.: Laser-based micro/nanoengineering for biological applications. *Prog. Quantum Electron.* **33**, 127–163 (2009)
- Yang, W.E., Huang, H.H.: Improving the biocompatibility of titanium surface through formation of a TiO<sub>2</sub> nano-mash layer. *Thin Solid Films* **518**, 50–7545 (2010)
- Zhou, Y.L., Niinomi, M.: Ti–25Ta alloy with the best mechanical compatibility in Ti–Ta alloys for biomedical applications. *Mater. Sci. Eng. C* **29**, 1061–1065 (2009)
- Zhou, Y.L., Niinomi, M., Akahori, T.: Effects of Ta content on Young's modulus and tensile properties of binary Ti–Ta alloys for biomedical applications. *Mater. Sci. Eng. A* **371**, 283–290 (2004a)
- Zhou, Y.L., Niinomi, M., Akahori, T.: Decomposition of martensite  $\alpha$  during aging treatments and resulting mechanical properties of Ti–Ta alloys. *Mater. Sci. Eng. A* **384**, 92–101 (2004b)
- Zhou, Y.L., Niinomi, M., Akahori, T., Fukui, H., Toda, H.: Corrosion resistance and biocompatibility of Ti–Ta alloys for biomedical applications. *Mater. Sci. Eng. A* **398**, 28–36 (2005)



## **Modification of aluminium-titanium and nickel-titanium thin layers by plasma flow action**

N. Trklja<sup>1</sup>, B. Salatic<sup>2</sup>, I. Krstic<sup>1</sup>, B. Obradovic<sup>1</sup>, M. Kuraica<sup>1</sup>

<sup>1</sup> *Faculty of Physics, University of Belgrade, Belgrade, Serbia*

<sup>2</sup> *Institute of Physics, Belgrade, Serbia*

### **Abstract**

Morphological changes occurring on aluminum-titanium and nickel-titanium thin films, deposited on the silicon substrate, when treated with a compressed plasma flow have been investigated. The results of this type of interaction are compared with the results obtained in experiments where the interaction between the laser beam and the target was investigated. The energy density delivered to the surface is about 10 J/cm<sup>2</sup> in both types of interactions. Main similarities of compressed plasma flow treatment used here and laser beam treatment are surface uniform melting, perturbation action on melted surface layer and quenching of the produced surface wave structures.

### **1. Introduction**

Titanium alloys are used in a wide variety of fields – in microelectronics, aerospace and biomedical industries. Systems and parts and their selection may be based on corrosion resistance or in strength features, with additional requirement, the biocompatibility, for biomedical implant applications. Aluminum-titanium (Al-Ti) and nickel-titanium (Ni-Ti) alloys have very good physicochemical characteristics that make them useful for high-temperature wear and corrosion protection in mechanical applications. For example, adding a Ti to Al-alloy can lead to the formation of a fine scale, equiaxed grain structure, which improves the mechanical properties, reduces hot tearing and eliminates porosity.

The main focus of this study is to analyze morphological changes occurring on Al-Ti and Ni-Ti thin films when treated with a compressed plasma flow (CPF) which was formed in the magnetoplasma accelerator and comparison of these changes with those obtained during the treatment with Er:glass and Nd:YAG laser pulses.

### **2. Experimental setup and procedure**

Al-Ti and Ni-Ti multilayer systems have been created by alternate deposition of nanometer-thick layers (of Al or Ni on Ti) on a single silicon substrate, by sputter deposition method

represented in [1]. The thickness of each individual layer is roughly 20 nm. Wafers of Si(100) was used as substrate. The deposited structures consisted of 10 alternate Al (or Ni) and Ti layers, five of each and 20 alternate Al (or Ni) and Ti layers, ten of each. The surfaces of the samples before plasma treatment are shown in Fig 1. The image was made by atomic force microscope (AFM).

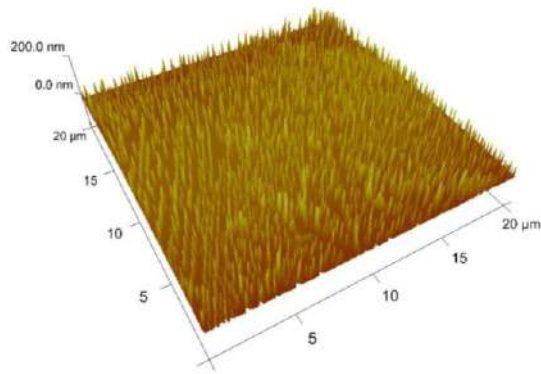


Fig. 1. AFM analysis of the 5x(Ni-Ti)/Si samples before plasma treatment.

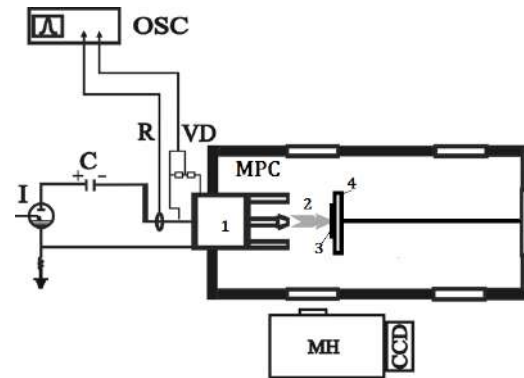


Fig. 2. Scheme of the experimental setup: 1. Magnetoplasma accelerator, 2. CPF, 3. Sample, 4. Sample brass holder.

The plasma source is a quasistationary plasma accelerator which operates in the mode of ion current transfer. The plasma acceleration by the Ampere force in MPC interelectrode gap is accompanied by formation of a compression plasma flow at the outlet of the discharge device. The plasma flow is compressed due to interaction of longitudinal current component with intrinsic azimuthal magnetic field (pinch effect) [2]. The stable CPF is formed 20  $\mu\text{s}$  after the beginning of the discharge. Relatively high values of plasma parameters of the compressed plasma flows (electron density in the order of  $10^{23} \text{ m}^{-3}$ , and plasma temperature of 20000 K) together with large plasma flow velocity (of 100 km/s in hydrogen plasmas) and discharge duration (of up to 100-150  $\mu\text{s}$ ) makes them suitable and efficient for studies of surface modifications under high thermal loads. In addition, we are able to investigate the formation of specific micro- and nanostructures, the occurrence of morphological characteristics arising from the movement of the molten material pieces, and the formation of craters caused by ablation of the target. Scheme of the experimental setup is shown in Fig.2. In present investigation helium with addition of 5% of hydrogen was used as a working gas at 6 mbar pressure. Maximum current in discharge was about 50 kA with time duration of the plasma flow up to 150  $\mu\text{s}$ .

Samples treated by the compressed plasma flows have been analysed by atomic force microscope (AFM) and scanning electron microscope (SEM).

### 3. Experimental results and discussion

The energy density delivered to the surface is about  $10 \text{ J/cm}^2$  [2] and surface is uniformly melted. Due to the fast cooling of the melted surface layer, the surface structures formed during melt phase are freezing (quenched) during a process of the melt resolidification. The central area of the treated surface contains craters with a diameter of 5 or 10  $\mu\text{m}$  and mosaic structures with well-defined boundaries of the characteristic dimension of 1-2  $\mu\text{m}$  (Fig. 3.). Orientation of these structures corresponds to the orientation of the silicon substrate. These microstructures originate from the redeposition of thin film materials on the partially destroyed structure of the Si substrate. The periphery area of the treated surface contains periodical structures which are smooth, homogenous and sinusoidally shaped, as would be expected from the frozen capillary waves (Fig. 4.). Typical wavelength of the periodical structures is 10  $\mu\text{m}$ .

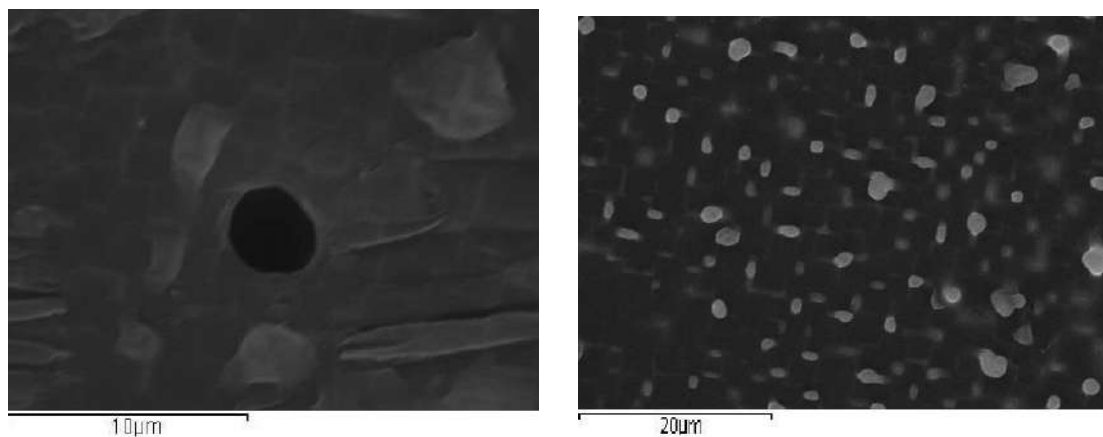


Fig. 3. SEM analysis of the 5x(Ni-Ti)/Si multilayer target after CPF treatment (a) crater (b) mosaic microstructure

These processes are comparable to the (Ni-Ti)/Si and (Al-Ti)/Si surface modifications during laser treatment [3, 4]. Typical wavelengths of the periodical structures in the periphery region are the same (10  $\mu\text{m}$ ). Mosaic structures formed in the central area are smaller in the process of laser treatment (100 nm).

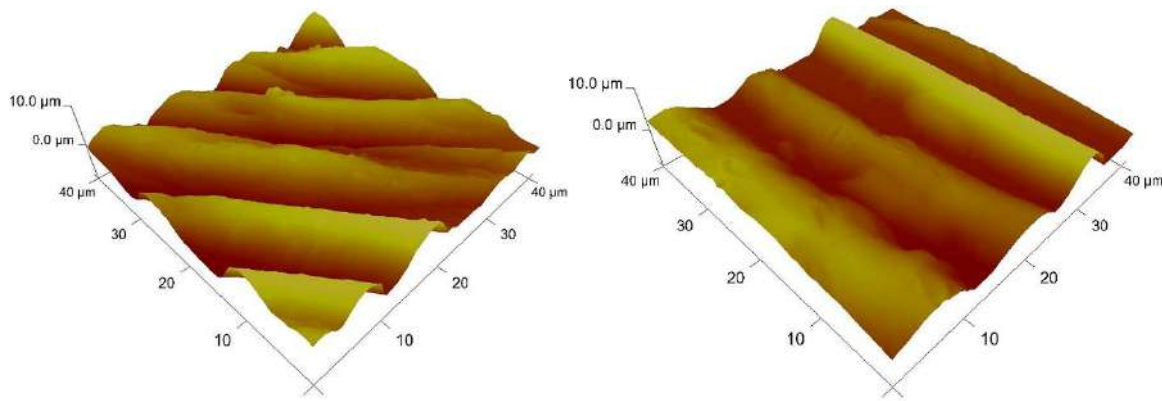


Fig. 4. AFM analysis of the multilayer target after CPF treatment: (a) 10x(Ni-Ti)/Si (b) 10x(Al-Ti)/Si

Results of silicon surface interaction with CPF have shown formation of the periodical structures very similar to those observed in present experiment. Wavelengths of silicone periodical structures are 4-8  $\mu\text{m}$ . Thickness of near-surface molten layer is estimated at 6-10  $\mu\text{m}$ . It can be concluded that, in present experiment, periodical structures come from interaction of thin films with plasma, as well as from silicon – plasma interaction.

#### 4. Conclusions

The basic effects of the CPF action on a solid target are surface melting, formation of different surface patterns and their freezing during fast cooling (quenching effect).

When a target is irradiated with a laser beam, most of the absorbed energy of the laser radiation is transformed into heat. Modifications of treated surfaces – craters, mosaic structures and periodical periphery structures, are similar to those formed by plasma flow-target interaction. Present study is important for investigations related with material of interest for mechanical applications, for fusion experiments, biomedical implant applications, etc.

#### References

- [1] S.Petrovic et al., *Physica Scripta T149*, 014082 (2014)
- [2] I.P.Dožinović et al., *Vauum*, 80, 1381-1385 (2006)
- [3] B.Salatić et al., *Applied Surface Science*, 360, 559-565 (2016)
- [4] S. M. Petrovic et al., *Optics and Laser Technology*, 54, 22-29 (2013)



## Inducing LIPSS on multilayer thin metal films by femtosecond laser beam of different orientations

A. G. Kovačević<sup>1</sup>, S. M. Petrović<sup>2</sup>, B. Salatić<sup>1</sup>, M. Lekić<sup>1</sup>, B. Vasić<sup>1</sup>, R. Gajić<sup>1</sup>,  
D. Pantelić<sup>1</sup> and B. M. Jelenković<sup>1</sup>

<sup>1</sup>*Institute of Physics, University of Belgrade, Belgrade, Serbia*

<sup>2</sup>*Institute of Nuclear Sciences “Vinča”, University of Belgrade, Belgrade, Serbia*

e-mail: Aleksander.Kovacevic@ipb.ac.rs

The occurrence of laser-induced periodic surface structures (LIPSS) has been known for a while [1]. Multilayer thin films, like Al/Ti, are suitable for LIPSS formation and attractive for applications – due to their wearing behavior and corrosion resistance; LIPSS generation may improve their properties as well [2, 3]. LIPSS properties depend not only on the material but also on the beam characteristics, like wavelength, polarization and scanning directions, etc. [4].

After exposing with NIR femtosecond pulses from Coherent Mira 900 laser system in several beam exposures, we have analyzed the samples of thin metal film systems with Tescan Mira3 SEM and NTegra AFM. The formation of LIPSS is most probably due to the generation of surface plasmon polariton, through the periodic distribution of energy in the interaction zone which lead to thermal processes in layers and interfaces. Two types of LIPSS were generated, which differ in shape, orientation and in ablation pronounced or not. For consecutive interactions in the same direction, LIPSS maintained its orientation, while for orthogonal passes LIPSS with mutually orthogonal orientation were generated. LIPSS period fluctuated between 320 and 380 nm and structures with pronounced ablation have significantly smaller width. Probable mechanism is that for greater accumulated energy pronounced ablation takes place giving LIPSS in the form of “trenches”, while for less accumulated energy the buildup of the material – probably due to pronounced oxidation – lead to LIPSS in the form of “hills”.

ACKNOWLEDGEMENT: The work was supported by the Ministry of Science of the Republic of Serbia under No. III45016, OI171038 and OI171005.

### REFERENCES

- [1] H. M. van Driel et al., Phys. Rev. Lett. 49, 1955 (1982).
- [2] S. M. Petrović et al., Opt. Laser Technol. 54, 22 (2013).
- [3] A. Kovačević et al., Appl. Surf. Sci. 326, 91 (2015).
- [4] A. Kovačević et al., Appl. Surf. Sci. 417, 155 (2017).

## Natural waveguides on *Hoplia argentea* elytra

D. Pavlović<sup>1</sup>, B. Salatić<sup>1</sup>, S. Savić-Šević<sup>1</sup>, N. Vesović<sup>2</sup> and D. Pantelić<sup>1</sup>

<sup>1</sup>*Institute of Physics, University of Belgrade, Pregrevica 118, 11080 Belgrade, Serbia*

<sup>2</sup>*University of Belgrade - Faculty of Biology, Studentski Trg 16, 11000 Belgrade, Serbia*  
e-mail: danica.pavlovic@ipb.ac.rs

Light waveguides are structures with a role in receiving and channeling light and filtering certain wavelengths of the electromagnetic spectrum [1]. That's how it comes to light capturing and local reinforcement of its intensity, which can be further utilized for various purposes (e.g. conducting light to pigments in the eye, forming structural coloration, etc.) [2]. Based on their geometric structure waveguides can be planar or linear (banded or fibrous) [3].

Microstructures with a waveguide role have been studied a lot in the living world [4]. Structures with a function of optical waveguides have also been discovered in insects. They can be found on antennae, in complex eyes, on wing scales and other parts of the body [5], and can work as integral part of light or IR receptors, thermoregulatory systems, or can play an important role in the formation of structural coloration [6].

Here we present cuticular structures on beetle elytra (Insecta: Coleoptera) that produce structural coloration thanks to morphology and function of light waveguides. *Hoplia argentea* from family Rutelidae was used as a model organism. We found out that individuals of this species possess linear type of waveguides on its front hardened wings, which are responsible for the production of structurally green coloration.

### REFERENCES

- [1] M. J. Adams, *An introduction to optical waveguides*, 14 (Wiley, New York, 1981).
- [2] A. W. Snyder, R. Menzel, *Photoreceptor optics* (Springer Science & Business Media, 2012).
- [3] G. T. Reed, A. P. Knights, *Silicon photonics: an introduction* (John Wiley & Sons, New Jersey, 2004).
- [4] M. Bass, E. W. Van Stryland, D. R. Williams, *Handbook of optics* (McGrawHill, New York, 1995).
- [5] P. S. Callahan, *Appl. Opt.* **7** (8), 1425-1430 (1968).
- [6] N. N. Shi, C. C. Tsai, F. Camino, G. D. Bernard, N. Yu, R. Wehner, *Science* **349** (6245), 298-301a (2015).

## Formation of LIPSS on Al/Ti thin metal films by scanning of low-fluence femtosecond beam during cross-directional scanning

Aleksander Kovačević<sup>1</sup>, Suzana Petrović<sup>2</sup>, Marina Lekić<sup>1</sup>, Davor Peruško<sup>1</sup>, Vladimir Lazović<sup>1</sup>, Svetlana Savić-Šević<sup>1</sup>, Borislav Vasić<sup>1</sup>, Branislav Salatić<sup>1</sup>, Radoš Gajić<sup>1</sup>, Dejan Pantelić<sup>1</sup>, Branislav Jelenković<sup>1</sup>

(1) Institute of Physics, Pregrevica 118, 11080 Belgrade, Serbia

(2) Institute of Nuclear Sciences „Vinča“, PO Box 522, 11000 Belgrade, Serbia

Contact: M. Lekić (aleksander.kovacevic@ipb.ac.rs)

**Abstract.** Formation of periodic nanostructures on thin metal films by femtosecond laser beam (laser induced periodic nanostructures – LIPSS) influences the tribological properties of the surfaces. Having excellent mechanical properties, multilayer thin films, like 5x(Al/Ti)/Si, are interesting direction of investigation, because their multilayer structure enables forming of high quality LIPSS [1]. Two types of LIPSS are described, high spatial frequency LIPSS (HSFL) and low spatial frequency LIPSS (LSFL), which differ in their spatial frequency. During exposition of thin film metal systems with femtosecond beams, we changed scanning configuration [2]. We have exposed 5x(Al/Ti)/Si multilayer system with femtosecond beam from the laser system Coherent Mira 900 in NIR. Same areas have been exposed with two different scanning directions. The direction of the second scanning over the same area was orthogonal to the first one. The polarization direction during second scanning was orthogonal to the polarization direction during first scanning. In this way, several crossed LIPSS can be seen.

**Acknowledgements.** The work has been supported by the Ministry of Science, Republic of Serbia, under No. III45016, OI171038 and OI171005.

### REFERENCES

- [1] A. G. Kovačević, S. Petrović, et al., *Appl. Surf. Sci.* **326** (2015), 91–98.
- [2] A. G. Kovačević, S. Petrović, et al., *Appl. Surf. Sci.* **417** (2017), 155–159.

## Formation of LIPSS on Al/Ti thin metal films by scanning of low-fluence femtosecond beam during multi-pass scanning

Marina Lekić<sup>1</sup>, Aleksander Kovačević<sup>1</sup>, Suzana Petrović<sup>2</sup>, Davor Peruško<sup>1</sup>, Vladimir Lazović<sup>1</sup>, Svetlana Savić-Šević<sup>1</sup>, Borislav Vasić<sup>1</sup>, Branislav Salatić<sup>1</sup>, Radoš Gajić<sup>1</sup>, Dejan Pantelić<sup>1</sup>, Branislav Jelenković<sup>1</sup>

(1) *Institute of Physics, Pregrevica 118, 11080 Belgrade, Serbia*

(2) *Institute of Nuclear Sciences „Vinča“, PO Box 522, 11000 Belgrade, Serbia*

**Contact:** M. Lekić ( [lekic@ipb.ac.rs](mailto:lekic@ipb.ac.rs) )

**Abstract.** During interaction of femtosecond laser beam with metal surfaces, periodic nanostructures can be formed – laser induced periodic nanostructures, LIPSS. Two types of LIPSS have been recorded, of low and high spatial frequency (LSFL and HSFL, respectively). Thin metal films in multilayer systems, like  $5x(\text{Al/Ti})@\text{Si}$  are convenient for forming high quality LIPSS due to their multilayer structure [1] and are interesting because of their excellent mechanical properties. We have exposed the multilayer thin film metal systems  $5x(\text{Al/Ti})@\text{Si}$  with femtosecond beams with various scanning configurations [2]. The laser system was Coherent Mira 900 in NIR. The same areas have been exposed to several scans of the beam (multi-pass scanning). In this way, it is possible to see that the LIPSS maintain their structure during consecutive scans.

**Acknowledgements.** The work has been supported by the Ministry of Science, Republic of Serbia, under No. III45016, OI171038 and OI171005.

### REFERENCES

- [1] A. G. Kovačević, S. Petrović, et al., *Appl.Surf. Sci.* **326** (2015), 91–98.  
[2] A. G. Kovačević, S. Petrović, et al., *Appl.Surf. Sci.* **417** (2017), 155–159.



## Formation of LIPSS on Al/Ti thin metal films by scanning of low-fluence femtosecond beam during cross-directional scanning

Aleksander Kovačević<sup>1</sup>, Suzana Petrović<sup>2</sup>, Marina Lekić<sup>1</sup>, Borislav Vasić<sup>1</sup>, Branislav Salatić<sup>1</sup>, Dejan Pantelić<sup>1</sup>, Branislav Jelenković<sup>1</sup>

(1) Institute of Physics, Pregrevica 118, 11080 Belgrade, Serbia

(2) Institute of Nuclear Sciences „Vinča“, PO Box 522, 11000 Belgrade, Serbia

Contact: A. Kovačević (aleksander.kovacevic@ipb.ac.rs)

**Abstract.** Interaction of femtosecond laser beam with surfaces may induce the formation of LIPSS, laser induced periodic surface structures, with periods below the wavelength of the laser beam. The interaction with metals may improve the surface tribological properties. Due to multilayer structure, multilayer thin films are convenient for formation of periodic nanostructures of high quality with low fluence beam. We have exposed 5x(Al/Ti)/Si multilayer system with femtosecond beam from the laser system Coherent Mira 900 in multipass and cross-directional regimes. The irradiated samples have been analyzed by Tescan Mira3 SEM. Two forms of LIPSS were generated: „ridges“, parallel to the polarization direction of the beam, and „trenches“, perpendicular to the polarization direction. Both types are probably caused by the occurrence of SPP, surface plasmon polariton, on the topmost surface. The SPP is linked to the heat distribution which influenced the forming of structures. „Ridges“ are probably due to the build up of the material with possible oxidation, while „trenches“ are formed by ablation.

**Acknowledgements.** The work has been supported by the Ministry of Science, Republic of Serbia, under No. III45016, OI171038 and OI171005.

### REFERENCES

- [1] A. G. Kovačević, S. Petrović, et al., *Appl.Surf. Sci.* **326** (2015), 91–98.
- [2] A. G. Kovačević, S. Petrović, et al., *Appl.Surf. Sci.* **417** (2017), 155–159.

## Origin and biomimicry of golden color in moth

Svetlana Savić-Šević<sup>1</sup>, Dejan Pantelić<sup>1</sup>, Branislav Jelenković<sup>1</sup>, Branislav Salatić<sup>1</sup>, Dejan V. Stojanović<sup>2</sup>

(1) Institute of Physics, University of Belgrade, Pregrevica 118, 11080 Zemun, Serbia.

(2) Institute of Lowland Forestry and Environment, University of Novi Sad, Antona Cehova 13, 21000 Novi Sad, Serbia

Contact: S. Savić-Sević ( [savic@ipb.ac.rs](mailto:savic@ipb.ac.rs) )

**Abstract.** We describe a new type of photonic material inspired by a *Diachrysia chrysitis* moth, whose nano-structured wings exhibit a prominent golden color. Wing scales and membranes of the moth represent layered structure with rough surfaces. Theoretical analysis shows that the several optical effects – interference, scattering and absorption - cooperate to produce golden wing color [1]. As a proof of this concept, it is necessary to manufacture the layered structure having rough surfaces. We have created a peculiar kind of volume diffraction grating, where the nano-spherical particles are introduced between the grating layers. It was created through a combination of holographic method (top-down technique) and non-solvent-induced phase separation (bottom-up technique). Alternating air-pullulan layers are produced and held in place by sparsely separated nano-pillars. Air voids are filled with 20 - 100 nm diameter spherical nanoparticles which act as scatterers. Such materials, with a high refractive index contrast and nano-scale scatterers, are important for achieving large reflectance and broad spectrum. Reflection spectrum of artificial structure of moth is quite similar to the one of *D. Chrysitis*. Both spectra are broad with cut-off wavelength at approximately 500 nm, visually corresponding to golden color. The comparison between experimental data obtained from the artificial structure of moth and theoretical results simulated for model structures strongly supported our hypothesis on the origin of the gold color [2].

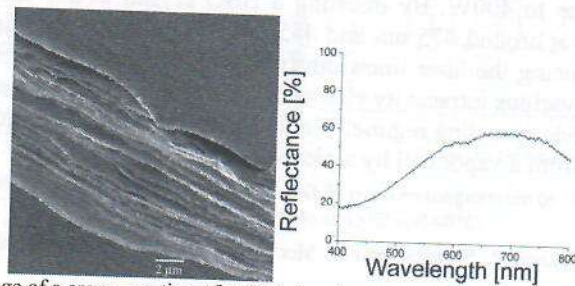


Figure 1. SEM image of a cross - section of artificial moth structure and experimentally recorded reflection spectra.

### REFERENCES

- [1] D. Pantelić, S. Savić-Šević, D. Stojanović, S. Čurčić, A. Krmpot, M. Rabasović, D. Pavlović, V. Lazović and V. Milošević, *Physical Review E*, **95** (2017), 032405-1–032405-10.
- [2] S. Savić-Šević, D. Pantelić, Branislav Jelenković, Branislav Salatić, Dejan V. Stojanović, *Soft Matter* **14** (2018), 5595–5603.



## Inducing LIPSS on multilayer thin metal films by ultrashort laser beam in different ambient conditions

Aleksander G. Kovačević<sup>1</sup>, Suzana Petrović<sup>2</sup>, Branislav Salatić<sup>1</sup>, Marina Lekić<sup>1</sup>, Borislav Vasić<sup>1</sup>, Dejan Pantelić<sup>1</sup>, Branislav Jelenković<sup>1</sup>

(1) *Institute of Physics – University of Belgrade, Pregrevica 118, 11080 Belgrade, Serbia*

(2) *Institute of Nuclear Sciences “Vinča” – University of Belgrade, P.O.Box 522, 11000 Belgrade, Serbia*

**Contact:** A. Kovačević ( [aleksander.kovacevic@ipb.ac.rs](mailto:aleksander.kovacevic@ipb.ac.rs) )

**Abstract.** Laser induced periodic surface structures (LIPSS) may be induced during the interaction of ultrashort laser pulses with surfaces [1]. Having periods below the wavelength of the laser beam, the area of their application is wide, particularly on metal surfaces [2]. Due to lamellar structure, multilayer thin metal films are suitable for high quality LIPSS formation which can improve their characteristics [3, 4]. The beam, the material, and the ambient/environment meet during the interaction and their properties and states/conditions (polarization and scanning directions, temperature, electrical current, composition, ...) influence the characteristics of the LIPSS [5]. We have exposed multilayer thin films of various metals (Al, Ti, Ni, Zr, ...) to Coherent Mira 900 laser system in different conditions of beam, ambient and material; the irradiated samples have been analyzed by Tescan Mira3 SEM and NTegra AFM. Two forms of LIPSS were generated, differing in shape, pronounced ablation, orientation and period. During multi-pass scanning, LIPSS maintained the configuration. During orthogonal scanning, orthogonal LIPSS occurred at some areas. The occurrence of surface plasmon polariton (SPP) is the most probable cause which led to periodic distribution of energy on the surface and thermal processes.

**Acknowledgements.** The work was supported by the Ministry of Science of the Republic of Serbia under No. III45016, OI171038 and OI171005. The authors also thank dr Davor Peruško from the Institute of Nuclear Sciences “Vinča” of the University of Belgrade and to dr R. Gajić, dr A. Krmpot, dr M. Rabasović and V. Lazović, all from the Institute of Physics of the University of Belgrade, for their valuable support.

### REFERENCES

- [1] H. M. van Driel, J. E. Sipe and J. F. Young, *Phys. Rev. Lett.* **49**, 1955 (1982).
- [2] A. Y. Vorobyev and C. Guo, *Laser Photonics Rev.* **7**, 385 (2013)..
- [3] S. M. Petrović, D. Peruško, et al., *Opt. Laser Technol.* **54**, 22 (2013).
- [4] A. G. Kovačević, S. Petrović, et al., *Appl. Surf. Sci.* **326**, 91 (2015).
- [5] A. G. Kovačević, S. Petrović, et al., *Appl. Surf. Sci.* **417**, 155 (2017).

## Laser-induced parallel structures on multilayer thin films of Ni, Pd, Ti, Ta and W

Aleksander G. Kovačević<sup>1</sup>, Suzana Petrović<sup>2</sup>, Jelena Potočnik<sup>2</sup>, Marina Lekić<sup>1</sup>, Branislav Salatić<sup>1</sup>, Vladimir Lazović<sup>1</sup>, Dejan Pantelić<sup>1</sup>, Branislav Jelenković<sup>1</sup>

(1) *Institute of Physics, University of Belgrade, Pregrevica 118, 11080 Belgrade, Serbia*

(2) *Institute of Nuclear Sciences “Vinča”, University of Belgrade, POBox 522, 11001 Belgrade, Serbia*

**Contact:** A. Kovačević ( [aleksander.kovacevic@ipb.ac.rs](mailto:aleksander.kovacevic@ipb.ac.rs) )

**Abstract.** The interaction of ultrashort laser beam with metal surfaces may induce the generation of periodic structures (LIPSS) with period less than the incoming wavelength, opening wide area of application [1, 2]. The presence of the underneath layer influences the quality of the LIPSS [3]. We have exposed multilayer thin films Ni/Ti, Ni/Pd, W/Ti, Ti/Ta to femtosecond beams of various wavelengths and powers. The interactions have been performed by Mira900 fs laser of Coherent. Detailed surface morphology after irradiation was examined firstly by optical microscopy, and then by scanning electron microscopy (JEOL JSM-7500F, Tokyo, Japan). Two types of structures have been noticed. Their appearance differ in the direction against the polarization direction, in pronounced ablation and in the spatial period, enabling their grouping into LIPSS of higher and lower spatial frequencies. Surface plasmon polariton is seen as the most probable cause of periodic distribution of energy at the surface and consequently to LIPSS.

**Acknowledgements.** The work was supported by the Ministry of Science of the Republic of Serbia under No. III45016 and OI171038. The authors also thank dr Davor Peruško from the Institute of Nuclear Sciences “Vinča” (University of Belgrade), dr V. Pavlović from the Faculty of Agriculture (University of Belgrade), dr Đ. Veljović and dr Ž. Radovanović from the Faculty of Technology and Metallurgy (University of Belgrade) and dr A. Krmpot and dr M. Rabasović from the Institute of Physics (University of Belgrade), for their valuable support.

### REFERENCES

- [1] H. M. van Driel, J. E. Sipe and J. F. Young, *Phys. Rev. Lett.* **49**, 1955 (1982).
- [2] A. Y. Vorobyev and C. Guo, *Laser Photonics Rev.* **7**, 385 (2013).
- [3] A. G. Kovačević, S. Petrović, et al., *Appl. Surf. Sci.* **326**, 91 (2015).



## Synergy of interference, scattering and pigmentation for structural coloration of *Jordanita globulariae* moth

Danica Pavlović<sup>1</sup>, Svetlana Savić-Šević<sup>1</sup>, Branislav Salatić<sup>1</sup>, Dejan Pantelić<sup>1</sup>

(1) Institute of Physics Belgrade, Pregrevica 118, 11080 Belgrade, Serbia

Contact: Danica Pavlović ( [danica.pavlovic@ipb.ac.rs](mailto:danica.pavlovic@ipb.ac.rs) )

**Abstract.** Structural coloration has attracted a lot of attention due to its significance in biophotonics and biomimetics. Structural and pigment colorations are omnipresent in insects, producing a range of colors for camouflage, warning, mimicry and other strategies necessary for survival. The coupling of structural and pigment colorations has been largely unnoticed. Herein we show how pigments, scattering and interference work together in two-dimensional waveguiding structures to produce the coloration of *Jordanita globulariae* (Huebner, 1793), a moth whose forewings sparkle with slightly iridescent green scales. We reveal the structure and function of the scales of the *Jordanita globulariae* moth through morphological characterization, spectral measurement and numerical simulation. The synergistic operation of structure and pigments is analyzed. We also discuss the role of this particular coloration in the moth's lifestyle.